Institut für Festkörperphysik

FRIEDRICH-SCHILLER-UNIVERSITÄT JENA

Tieftemperaturphysik Prof. Dr. P. Seidel Prof. Dr. F. Schmidl	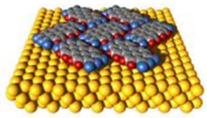 **Angewandte Physik / Festkörperphysik** Prof. Dr. T. Fritz
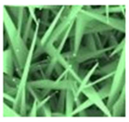 **Experimentelle Festkörperphysik** Prof. Dr. C. Ronning	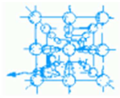 **Ionenstrahlphysik** Prof. Dr. E. Wendler
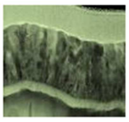 **Photovoltaik** Prof. Dr. C. Ronning Dr. U. Reislöhner	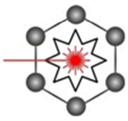 **Laborastrophysik und Clusterphysik** Dr. C. Jäger

Annual Report 2013

Institut für Festkörperphysik

Friedrich-Schiller-Universität Jena

Annual Report 2013

Editor: Prof. Dr. Torsten Fritz

Institut für Festkörperphysik
Friedrich-Schiller-Universität Jena
Helmholtzweg 3/5
D-07743 JENA

home page: http://www.ifk.uni-jena.de/

Prof. Dr. Torsten Fritz	Tel.:	+49 (0) 3641 / 947400, 947411
(director)	Fax:	+49 (0) 3641 / 947412
	e-mail:	torsten.fritz@uni-jena.de
	home page:	http://www.organics.uni-jena.de
Prof. Dr. Carsten Ronning	Tel.:	+49 (0) 3641 / 947300, 947301
	Fax:	+49 (0) 3641 / 947302
	e-mail:	carsten.ronning@uni-jena.de
	home page:	http://www.nano.uni-jena.de http://www.photovoltaik.uni-jena.de
Prof. Dr. Paul Seidel	Tel.:	+49 (0) 3641 / 947410, 947411
	Fax:	+49 (0) 3641 / 947412
	e-mail:	paul.seidel@uni-jena.de
	home page:	http://www.tieftemperaturphysik.uni-jena.de/
Prof. Dr. Frank Schmidl	Tel.:	+49 (0) 3641 / 947429, 947411
	Fax:	+49 (0) 3641 / 947412
	e-mail:	frank.schmidl@uni-jena.de
	home page:	http://www.tieftemperaturphysik.uni-jena.de/
Prof. Dr. Elke Wendler	Tel.:	+49 (0) 3641 / 947333
	Fax:	+49 (0) 3641 / 947302
	e-mail:	elke.wendler@uni-jena.de
	home page:	http://www.physik2.uni-jena.de/inst/exphys/ionen/
Dr. Cornelia Jäger	Tel.:	+49 (0) 3641 / 947354
	Fax:	+49 (0) 3641 / 947308
	e-mail:	cornelia.jaeger@uni-jena.de
	home page:	http://www.astrolab.uni-jena.de/

Preface

We like to take this annual report 2013 as an opportunity to thank a lot of people and organizations for their manifold support for our research at the Institute of Solid-State Physics at the Friedrich-Schiller-University Jena. Furthermore, this report, which is already the 18th in this series, is also addressed to the interested scientific community and to our colleagues within the university and from outside.

Special thanks go to the following organizations for their financial support:

- Deutsche Forschungsgemeinschaft – DFG
- Bundesministerium für Bildung und Forschung – BMBF
- Bundesministerium für Umwelt, Naturschutz und Reaktorsicherheit – BMU
- Bundesministerium für Wirtschaft und Technologie – BMWi
- Thüringer Ministerium für Bildung, Wissenschaft und Kultur – TMBWK
- Deutscher Akademischer Austauschdienst – DAAD
- Gesellschaft für Schwerionenforschung, Darmstadt – GSI
- Deutsches Elektronen Synchrotron, Hamburg – DESY
- Several industrial partners

We also like to thank all our colleagues at other universities and institutes which were or still are collaborating with us, but where the collaborative work has not been presented in the research articles of this report. Furthermore, we are very grateful for the work of our very motivated secretaries, technicians, and the people in the mechanical and electrical workshops. All of them have contributed to our research in an outstanding way and, thus, to this report.

Prof. Dr. Torsten Fritz
(director)

Contents

2. Scientific Reports

5. Publications

6. Cooperations, guests and colloquia at the IFK

7. Teaching activities

1. Scientific Groups of the Institute

Applied Physics / Solid State Physics

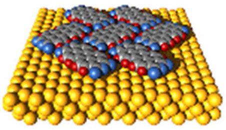

Prof. Dr. Torsten Fritz

- Preparation of highly ordered thin films of organic molecules by UHV-deposition (OMBE)
- Chemical vapor deposition and characterization of carbon nanotubes
- Epitaxial graphene
- Organic-organic heteroepitaxy
- K-doped organic superconductors
- Organic-inorganic hybrid solar cells
- *In situ* optical spectroscopy (DRS and PL) on ultrathin molecular layers
- Analyses of surfaces, layers and nanostructures using AES, XPS, LEED, RHEED, XPD, STM, AFM, and SEM

The group ***Applied Physics / Solid State Physics*** at the Institute of Solid State Physics is engaged in the research on nanostructures, solid surfaces and thin films of both organic and inorganic semiconductor materials.

Our main research interest lays in the discovery of structure-property-relations of structurally well defined ultrathin epitaxial layers, organic quantum wells, K-doped organic super conductors, and carbon nanotubes. The main target of our research is the development of basic principles for the use of nano materials in prospective devices.

For the analyses of the chemical composition and bonding at surfaces and in thin films we use surface analysis methods like photoelectron spectroscopy (XPS, UPS) and Auger electron spectroscopy (AES). The crystalline structure can be determined by electron diffraction (LEED, RHEED, XPD, and electron channeling). Scanning tunneling microscopy (STM), atomic force microscopy (AFM) and scanning electron microscopy (SEM) are used for high-resolution imaging of nanostructures and surfaces.

Our *in situ* optical spectroscopy, namely differential reflectance spectroscopy (DRS) is used to study organic (sub-)monolayers and heterostructures in terms of absorption spectroscopy to analyse the optical interaction between either the molecules itself, organic adsorbates and inorganic substrates, or molecules and dopants.

Experimental Physics / Solid State Physics

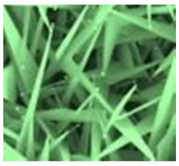

Prof. Dr. Carsten Ronning

- Synthesis, doping and functionization of semiconductor nanowires
- Photovoltaics
- Atmoic structure and band-gap of complex semiconductors
- Growth and functionalization of diamond-like materials
- Synthesis and modification of memoristive materials and devices
- Semiconductor physics: doping using ion beams

Recent work of the research group ***Experimental Physics / Solid State Physics*** in the field of semiconductor nanowires focuses both on the growth of desired nanostructures as well as on the modification of semiconductor nanowires using ion beams for the use as photonic and electronic devices. This includes the realization of light-emitting diodes, field effect transistors, sensors for bio and chemical applications, and the observation of laser oscillations within single nanowires. Another scientific area of the group is the investigation of hard/soft interfaces in terms of biocompatibility. Here, the accelerator systems Mr. JIM Stringer and LEILA are used for the growth of diamond-like materials as well as for nanostructuring of surfaces (ripples). Furthermore, the group works on the investigation and manipulation of memoristive materials and devices using ion beams.

The research on photovoltaics is directed to two different fields: (a) Preparation and development of $Cu(In,Ga)(Se,S)_2$ - based thin film solar cells (CIGS). The research aims at a better understanding of the materials science of the CIGS chalcopyrite semiconductor and the improvement of existing and the development of novel cell concepts. To this end, a complete baseline on a form factor of 10x10 cm^2 is available as well as various characterization tools including AM 1.5 solar simulation and spectral response. (b) Preparation and development of CdTe-based thin film solar cells. The research aims at a better understanding of the materials science of the II-VI semiconductor CdTe and the improvement of existing and the development of novel cell concepts. To this end, a complete baseline on a form factor of 10x10 cm^2 is available as well as various characterization tools including AM 1.5 solar simulation and spectral response.

Low Temperature Physics

Prof. Dr. Paul Seidel

- Superconductivity within thin layers and layer systems
- Josephson effects, proximity effect, and tunnel effects in superconducting devices
- DC-SQUID's and their application in measurements, e.g. CCC, MRX
- cryogenic measurements of mechanical quality factor and optical properties
- Dynamics of superconducting Josephson arrays
- cryogenic engineering (cryocoolers, cryogenic storage)

The ***Low Temperature Physics*** group works on the following fields:

- preparation, characterization, modelling and application of Josephson junctions and SQUIDs (precision and magneto-relaxation measurements with LTS SQUIDs, development of HTS SQUIDs, intrinsic Josephson junctions and Josephson junctions with iron based superconductors)
- low temperature physics and cryogenic engineering (development of new kinds of pulse tube cryocoolers with magnetic regenerators, cryogenic storage, cryogenic current comparator CCC for particle beam analysis)
- experimental work within the SFB/TR7 on cryogenic measurements of the Q-factor and of optical properties of components for future gravitational wave detectors like the Einstein Telescope
- thin film technologies for insulators and other materials
- alternative preparation and properties of crystalline gold nanoclusters

The research is carried out in cooperations with other research groups in Thuringia (TU Ilmenau, IPHT Jena, SUPRACON Jena, Innovent e.V. Jena, Helmholtz Insitute Jena). Within common activities the group works together with the Gesellschaft für Schwerionenforschung Darmstadt, DESY Hamburg, MPI Heidelberg, IFW Dresden and the Zentrum für Raumfahrttechnologie und Mikrogravitation and DLR Bremen.

Several research activities exist with industrial partners e.g. with Chemicell Berlin, HTS Systeme Wallenfels, and the TransMIT center for adaptive cryotechniques Gießen. A long tradition of cooperation with the the Universities of Moscow (Russia), Bratislava (Slovak Republic), Kharkov (Ukraine), Glasgow (U.K.), Poznan (Poland), Padua, Torino and Florence (Italy), Twente (Netherlands) and the Universities of Osaka, Tokyo and Nagoya (Japan) is also remarkable.

Ion Beam Physics

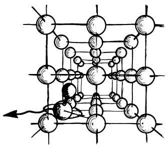

Prof. Dr. Elke Wendler

- Modification of solids by ion implantation and
- succeeding processes
- Ion beam analysis (RBS, PIXE, ERD, NRA)
- Ion beam synthesis of buried nanostructures
- Investigation of the effect of high electronic excitation on structural
- modification of crystalline and amorphous semiconductors

The ***Ion Beam Physics*** group deals with modification of solids and synthesis of buried nanostructures using ion beams and combined secondary processes. The studies cover fundamental processes of ion-beam induced structural modification in semiconductors and insulators being relevant for future electronic, optoelectronic and photonic device technologies.

Silver nanoclusters were successfully formed in LiNbO3 by ion beam synthesis and subsequent annealing and absorption due to plasmon resonance was experimentally proven. To optimise patterning of LiNbO3 by ion beam enhanced etching of this material, damage formation by nuclear and electronic energy deposition of the implanted ions continued to be investigated in collaboration with the Institute of Applied Physics. Here especially the built-up of strain was studied and related to the detected amount of structural damage. Primary effects of damage formation were also studied in crystalline semiconductors. For SiC this work was done in collaboration with the University of Pretoria in South Africa and it could be shown that at elevated temperatures the volume introduced by the implanted ions is decisive for the occurring processes. In collaboration with the University Minsk in Belarus we continued our work on ion beam synthesis of III-V compound nanoclusters in silicon.

Beside these activities on materials modification utilizing ion beams with conventional energies (several 10 keV to several MeV), the effect of high electronic excitation due to swift heavy ion irradiation (several 100 MeV) on plastic deformation and on the formation of voids and porous structures in amorphous Ge were studied in collaboration with the Australian National University Canberra in Australia.

Laboratory Astrophysics / Cluster Physics

Dr. Cornelia Jäger

- Electronic spectroscopy of neutral and ionized polycyclic aromatic hydrocarbons (PAHs) in supersonic jets and cryogenic matrices
- Study of astrochemical reactions in liquid helium nanodroplets
- Low-temperature condensation of cosmic dust particles
- Study of gas-phase condensation processes of cosmic dust nanoparticles
- Study of the chemical and structural processing of dust grains and PAHs in astrophysical environments
- Photoluminescence studies of silicon and germanium nanocrystals produced by CO_2 laser pyrolysis

The ***Laboratory Astrophysics / Cluster Physics Group*** at the Institute of Solid State Physics results from a cooperation between the Max Planck Institute for Astronomy, Heidelberg, and the Friedrich Schiller University, Jena. Inaugurated in February 2003, it is now conducted by Prof. Dr. Thomas Henning and Dr. Cornelia Jäger.

The research of the Laboratory Astrophysics and Cluster Physics Group is devoted to fundamental astrophysical questions that can be answered by laboratory experiments, with particular emphasis on spectroscopy. The electromagnetic radiation reaching us from stellar objects is modified in a characteristic manner by interstellar molecules and dust particles. Many of these “fingerprints” are still far from being understood. In order to determine the species causing the modification of the electromagnetic signals detected by telescopes and satellites, comprehensive laboratory studies are urgently needed.

In our laboratory, we study the condensation, processing, and spectral properties of carbonaceous and siliceous dust grains and astrophysically relevant molecules that may play a role as progenitors of grain formation. Laboratory astrophysics is an interdisciplinary field whose research profits from sophisticated experimental facilities. We are able to simulate astrophysically relevant processes such as gas phase condensation of grains and molecules by laser-induced pyrolysis of hydrocarbons or laser ablation of solids in the laboratory. Interesting molecules, clusters, and nanoparticles are prepared in vacuum chambers under conditions coming close to those in interstellar or circumstellar environments (low pressures and definite temperatures ranges). Sophisticated analytical tools comprising optical spectroscopy, mass spectrometry, chromatography, and electron microscopy help us to characterise the composition and structure of the produced laboratory particulate and molecular analogues.

2. Scientific Reports

The complex polymorphism and thermodynamic behavior of a seemingly simple system: naphthalene on Cu(111)

Roman Forker, Julia Peuker, Matthias Meissner, Falko Sojka, Takahiro Ueba[1], Takashi Yamada[1], Toshiaki Munakata[1], and Torsten Fritz

[1]Osaka University, 1-1 Machikaneyama, Toyonaka, Osaka 560-0043, Japan

Naphthalene, $C_{10}H_8$ (two fused benzene rings), is the smallest polycyclic aromatic hydrocarbon (PAH). It is known to form three commensurate phases in epitaxial films on Cu(111) [1], one of those exhibiting chiral molecular arrangements, cf. Fig. 1. Attempting to shed light on this polymorphism we performed *in situ* low-energy electron diffraction (LEED) as a function of temperature T and surface coverage Θ, revealing an unexpected and extraordinarily complex structural and thermodynamic behavior.

Thin films of naphthalene were grown in ultra-high vacuum (UHV, $p \approx 10^{-8}$ Pa) on a sputter-cleaned, annealed Cu(111) surface using a pulsed leak valve. The metal single crystal was cooled with liquid nitrogen while being gently heated to various temperatures > 78 K. Naphthalene vapor as introduced into the UHV chamber adsorbed on the Cu(111) surface regardless of the sample being shadowed by the LEED apparatus. Therefore, diffraction images could be recorded while depositing $C_{10}H_8$ onto Cu(111), yielding thickness-dependent *in situ* measurements.

For rather low coverage at $T < 90$ K the molecules form a disordered gas-like phase as evidenced by ring patterns in LEED. The rings grow in diameter with rising coverage meaning that the intermolecular distance shrinks. Consequently, the lateral arrangement of molecules is influenced by a repulsive effect. Increasing Θ even more leads to the development of spots whereas the rings disappear. Hence, at least some structural order arises at a certain critical coverage. These emerging spots, however, change their position and even split upon further growth of molecules. Therefore they originate from a metastable precursor which undergoes a steady (and reversible) orientational shift upon variation of Θ (and T). Further increasing of the coverage up to a closed monolayer (ML) ultimately yields the long-range ordered stable film structure **A** with commensurate epitaxial coincidence, compare Fig. 1. From diluted submonolayers to closed monolayers the growth behavior thus resembles a 2D gas – liquid – solid phase transition [2].

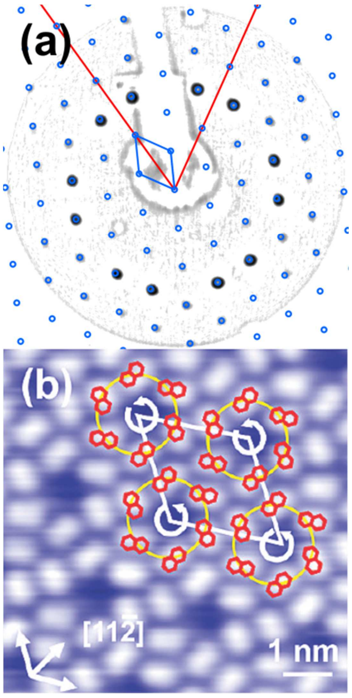

Fig. 1: *Naphthalene on Cu(111), structure* **A**, $(5\sqrt{3} \times 5\sqrt{3})R30°$ *at* $80\,K$. *(a) LEED image,* $E = 23\,eV$ *with reciprocal lattice simulation. (b) STM scan with an apparently chiral motif,* $V = -2.00\,V$, $I = 0.03\,nA$, *adapted from [1].*

Due to the distortion occurring in LEED images a calibration was performed using the well-known Si(111)-(7×7) surface reconstruction [3]. It was confirmed that structure **A** is indeed commensurate.

At elevated temperatures $T \approx 125$ K of the Cu(111) substrate the initial growth behavior of naphthalene is comparable, including the formation of diffraction rings and the subsequent occurrence of the precursor structure. However, the later development differs significantly from low growth temperatures. The Θ-dependent orientational shift does not transform the precursor into the commensurate structure **A**. Instead, a previously unknown structure **B** is preferred at high coverage, while the precursor fully disappears. Remarkably, structure **B** is point-on-line coincident [4] although commensurate structures are commonly thought to be energetically favored because of an exact lattice match. Reassessing ref. [1] one finds that structure **B** has a unit cell similar to the previously reported commensurate structure **C**, yet with a clear moiré contrast in STM images which cannot occur for commensurate superstructures, cf. Fig. 2. These subtle moiré patterns depend very sensitively on the structural relations between substrate and adsorbate lattices and can therefore be employed to analyze the epitaxial relation with high accuracy. Comparing our LEED results and the moiré analysis we find indeed the same unit cell parameters which readily confirm the point-on-line structure. Closer inspection of the STM images in ref. [1] reveals that structures **B** and **C** can coexist even on the same substrate terraces. Indeed, LEED spots of the commensurate structure **C** are found along with structure **B** in the same images, yet with noticeably lower intensity. Moreover, structure **B** is stable upon cooling down to $T < 90$ K and does not transform back into structure **A** as obtained for low temperature adsorption.

In summary, naphthalene thin films on Cu(111) are very susceptible to the growth parameters. The reversible transformation between a precursor and a stable epitaxial $C_{10}H_8$ film has not been reported before. Moreover, a point-on-line structure may be thermodynamically preferred to a “simple” commensurate coincidence.

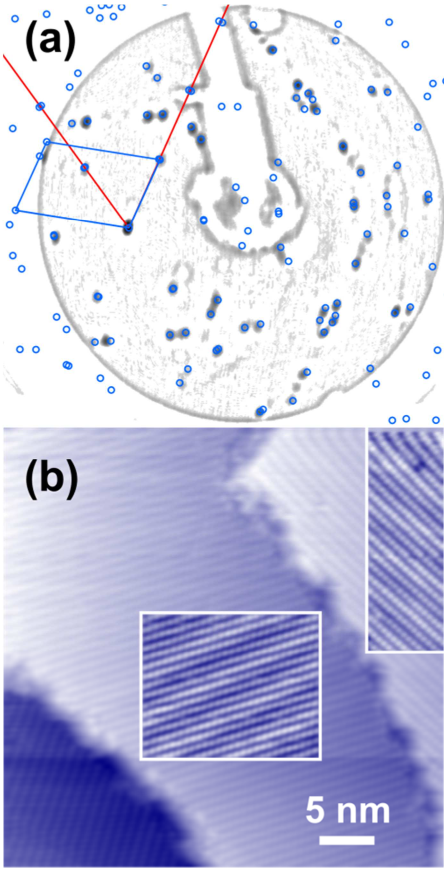

Fig. 2: *Naphthalene on Cu(111), structure* ***B****, point-on-line,* $T \approx 125\,K$. *(a) Tilted LEED image,* $E = 27\,eV$ *with reciprocal lattice simulation. (b) STM scan with enhanced contrast insets showing distinct moiré patterns,* $V = -2.50\,V$, $I = 0.02\,nA$, *adapted from [1].*

References

[1] T. Yamada *et al.*, J. Phys. Chem. C **114**, 13334 (2010).
[2] F. Bischoff *et al.*, ACS Nano **7**, 3139 (2013).
[3] F. Sojka *et al.*, Rev. Sci. Instrum. **84**, 015111 (2013) & Ultramicroscopy **133**, 35 (2013).
[4] D.E. Hooks *et al.*, Adv. Mater. **13**, 227 (2001).

Charge transfer between molecules and vacancies at the PTCDA/ZnO interface

Marco Grünewald, Michael Kozlik, Christian Zwick, Roman Forker, and Torsten Fritz

In recent years organic thin films have been established in applications such as light emitting diodes (OLED), field effect transistors (OFET) and photovoltaic devices [1-3]. The understanding of the interaction mechanisms at interfaces, especially when the interface is not perfect but exhibits a noticeable number of defects, is of fundamental importance to improve the efficiency of organic semiconductor components in the future. Therefore, we investigate layers of the archetypal organic semiconductor 3,4,9,10-perylene-tetra-carboxylic-dianhydride (PTCDA) on ZnO which is established as material for transparent electrodes in solar cells. The 30 nm ZnO film was sputter-deposited on a quartz glass substrate at room temperature and at a deposition rate of 5 nm/min using an argon flow of 6 sccm. The pressure was kept at approx. $3 \cdot 10^{-3}$ mbar. Afterwards the samples were thoroughly degased in UHV and cautiously argon sputtered at 1 kV and ca. 100 nA/cm² for 15 min in order to create vacancies in the ZnO film. Then PTCDA was deposited at a low deposition rate of 0.2 ML/min and monitored by means of *in-situ* differential reflectance spectroscopy (DRS) which is described in detail elsewhere [4-6]. The DRS quantity is defined as follows:

$$DRS(E,d) \equiv \frac{\Delta R}{R} := \frac{R(E,d) - R(E,d=0)}{R(E,d=0)}, \qquad (1)$$

where $R(E,d)$ denotes the reflectivity of the sample surface depending on the photon energy E and the film thickness d. The dielectric functions of the PTCDA films depending on the film thickness were extracted from the measured DRS spectra by using a numerical algorithm introduced in detail in refs. [4,7]. For this purpose the optical functions of the glass substrate and the ZnO have been determined via transmission and reflectance measurement by means of an *ex-situ* spectrophotometer Varian Cary 5000. In order to elucidate the development of the DRS spectra the ΔDRS spectra are shown as well calculated by using two subsequently measured reflectance spectra R_m and R_{m+1}:

$$\Delta DRS_{(m+1)\,-\,m} := \frac{R_{m+1} - R_m}{R_m}. \qquad (2)$$

In **Fig. 1 a)** the imaginary part ϵ'' of the dielectric function of PTCDA on 30 nm ZnO on quartz glass for effective thicknesses ranging from submonolayers up to 7 ML as extracted from the DRS is shown. From the optical spectra in the region above 2.1 eV it can be deduced that very thin films of PTCDA behave almost like monomers as known from PTCDA in solution [8] or from a monolayer on an inert mica substrate shown in the lower graph (studied in detail in ref. [9]). However, the additional feature in the ϵ'' spectra around 1.86 eV is absent in the well-known monomer spectrum [8] as well as in the bulk spectrum of PTCDA [10] but can be assigned to PTCDA anions as elucidated by comparison to potassium doped PTCDA on mica (lower graph of Fig 1, studied in detail in ref. [9]). Beyond 1 ML the formation of PTCDA stacks sets in, and due to the interaction of the transition dipoles of stacked molecules the spectrum con-

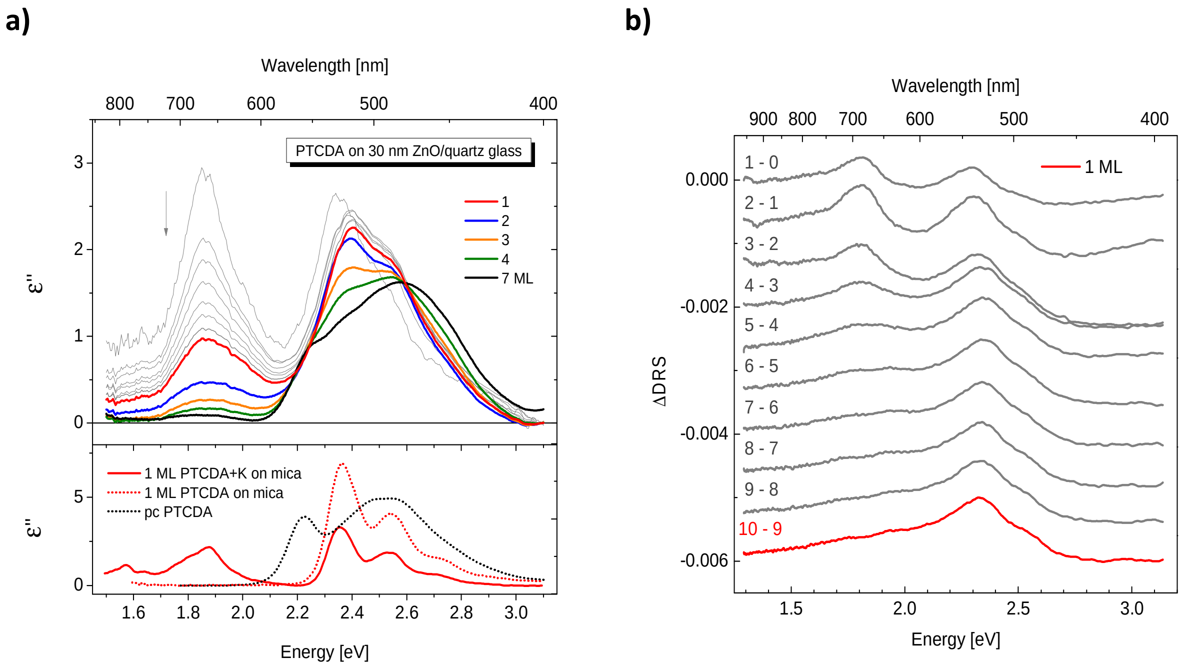

Fig. 1: a) *Imaginary part ϵ'' of the dielectric function of PTCDA on 30 nm ZnO on quartz glass for effective thicknesses ranging from submonolayers up to 7 ML extracted from the DRS shown in Suppl. Fig. 1.* ***b)*** *ΔDRS of PTCDA on quartz glass for effective thicknesses ranging from submonolayers up to 1 ML. The graphs are marked according to the scheme $(m+1)-m$ referring to eq. (2).*

verges towards the bulk spectrum of PTCDA (cmp. black-dotted spectrum in the lower panel). From the ΔDRS spectra in **Fig. 1b** we conclude that the formation of PTCDA anions is restricted to the growth up to 0.5 ML where PTCDA anions and neutral monomers are formed simultaneously.

With this contribution we could show that defects at an organic-inorganic interface can lead to an integer charge transfer resulting in new absorption bands of molecules at the interface. This information might be useful in designing organic devices where the organic thin films are becoming thinner and thinner and thus the interface gains more importance.

Acknowledgments

We thank Carsten Ronning for making his *ex-situ* optical spectroscopy equipment available to us.

References

[1] S. Liu *et al.*, Adv. Mater. **21**, 1217-1232 (2009).

[2] N.R. Armstrong *et al.*, Macromol. Rapid Commun. **30**, 717-731 (2009).

[3] B. Rand *et al.*, Appl. Phys. Lett. **87**, 33508 (2005).

[4] R. Forker *et al.*, Annu. Rep. Prog. Chem., Sect. C: Phys. Chem. **108**, 34-68 (2012).

[5] R. Forker and T. Fritz, Phys. Chem. Chem. Phys. **11**, 2142-2155 (2009).

[6] H. Proehl *et al.*, Phys. Rev. B **71**, 165207 (2005).

[7] R. Nitsche and T. Fritz, Phys. Rev. B **70**, 195432 (2004).

[8] M. Hoffmann, Dissertation, *Technische Universität Dresden*, 2000.

[9] T. Dienel *et al.*, Adv. Mater. **22**, 4064-4070 (2010).

[10] A.B. Djurišić *et al.*, Opt. Commun. **183**, 123-132 (2000).

[11] M. Kasha *et al.*, Pure Appl. Chem. **11**, 371-392 (1965).

Growth of natural "graphene flakes" on various substrates

Falko Sojka, Julia Peuker, Tobias Hümpfner, Matthias Meissner, Roman Forker, and Torsten Fritz

Organic molecules are increasingly gaining importance for the technical progress in our society. Solar cells made of organic molecular layers offer completely new opportunities through their flexibility, and organic LED displays are known for their brilliant colors. Recent studies also claim that highly doped organic molecules show superconducting properties. [1]

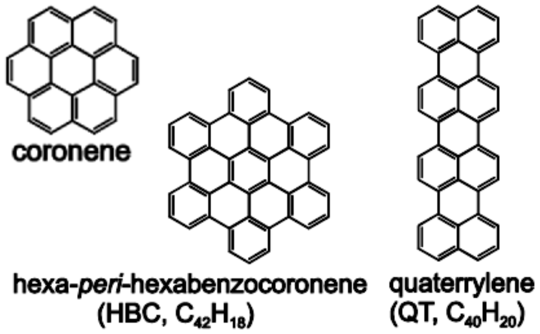

Fig. 1: *Chemical structures of coronene, hexa-peri-hexabenzocoronene (HBC), and quaterrylene (QT).*

Our goal is to search for superconductivity in highly ordered films of organic molecules in order to learn more about the conduction process and to find correlations between the molecules' shapes and superconducting characteristics such as the critical temperature or the critical magnetic field.

The candidate molecules (see Fig. 1) include coronene, hexa-peri-hexabenzocoronene (HBC) as the next larger-size graphene flake with also a hexagonal structure, and quaterrylene (QT). In this work, we are interested in the growth of the pristine molecules on various substrates, studied via low-energy electron diffraction (LEED) and scanning tunneling microscopy (STM).

All of our LEED images are corrected with *LEEDCal*, and the film structure was determined by fitting a simulation to the experimental spot positions using *LEEDLab*. [2, 3]

Figure 2 shows a LEED measurement of one monolayer of HBC grown on epitaxial graphene on top of silicon carbide. The structure we found is rather similar to the structure described by *Zimmermann et al.* [4] but differs significantly from the commensurism described there. The epitaxial matrix we found is:

$$C_{HBC} = \begin{pmatrix} 6.13 \pm 0.01 & 0.97 \pm 0.01 \\ -0.97 \pm 0.01 & 5.16 \pm 0.01 \end{pmatrix}$$

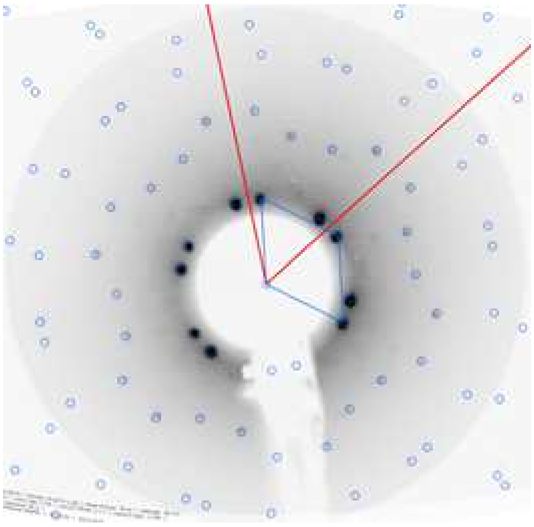

Fig. 2: *LEED image of HBC on graphene overlaid with the fitted structure simulation.*

We have further studied the growth of QT on graphene. Figure 3 shows the resulting diffraction pattern. In contrast to previous measurements [5], we were able to observe additional diffraction orders, because of our more sensitive LEED device. The epitaxial relation we found now can be described by:

$$C_{QT} = \begin{pmatrix} 0 & 3.67 \pm 0.03 \\ 18 & -5.22 \pm 0.05 \end{pmatrix}$$

This confirms the previous assumption of a non-commensurate but point-on-line growth.

As a first step to study coronene the molecule was deposited on a Ag(111) surface. This system was published by *Lackinger et al.* [6] to be commensurate with a 4x4 registry. That is exactly what we observe (see Fig. 4). Although in this case a hexagonal molecule grows on a hexagonal substrate yielding a hexagonal structure, a tilt of the molecular planes against the substrate was postulated by *Lackinger et al.* [6].

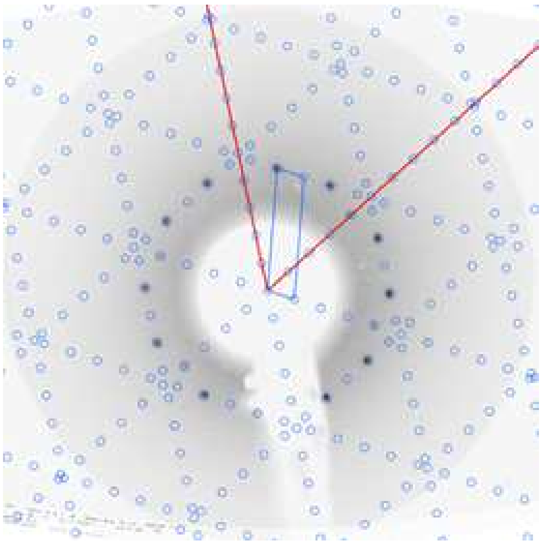

Fig. 3: *LEED image of QT on graphene overlaid with the fitted structure simulation.*

This seems unlikely and could not be verified with STM measurements at low temperatures (1.2 K, see Fig. 5) where only flat-lying molecules were observed. However, further investigations are necessary to be able to exclude tilted molecules definitely.

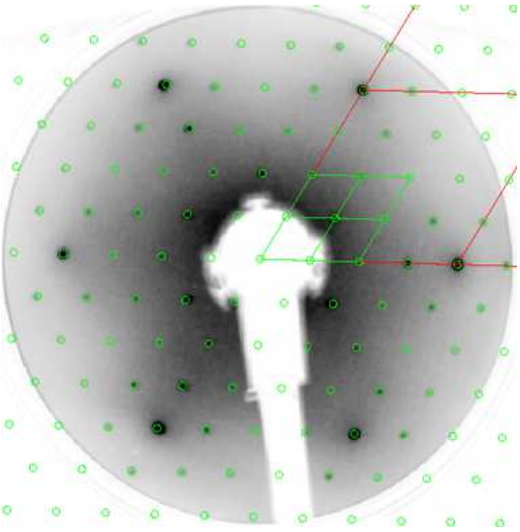

Fig. 4: *LEED image of coronene on Ag(111) overlaid with the fitted structure simulation.*

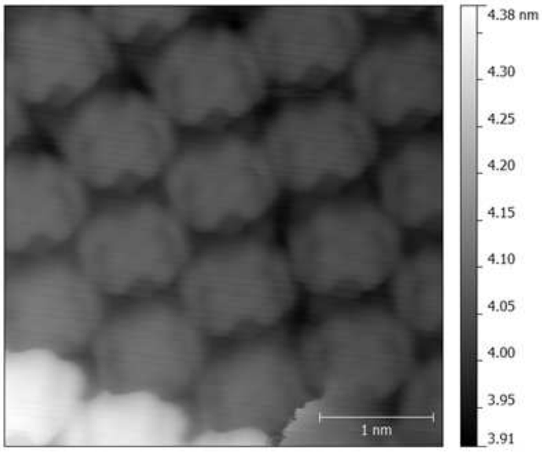

Fig. 5: *LT-STM image of coronene on Ag(111).*

References

[1] Y. Kubozono *et al.*, *Phys. Chem. Chem. Phys.* **13**, 16476-16493 (2011).

[2] F. Sojka *et al.*, *Rev. Sci. Instrum.* **84**, 015111 (2013).

[3] F. Sojka et al., *Ultramicroscopy* 133, 35-40 (2013).

[4] U. Zimmermann *et al.*, *Surf. Sci.* **268**, 296-306 (1992).

[5] R. Forker, *PhD Thesis*, TU Dresden (2010).

[6] M. Lackinger *et al.*, *J. Phys. Chem. B* **106**, 4482-4485 (2002).

Investigations of Rubrene Thin Films on Graphite and Highly Ordered Pyrolytic Graphite

Christian Udhardt, Takashi Yamada, Roman Forker, Toshiaki Munakata, and Torsten Fritz

The aim of this work is to localize electronic states on thin film surfaces of monolayer (ML) and sub-monolayer ranges, and associate them with film structures. The object of study is a highly oriented pyrolytic graphite (HOPG) surface covered with rubrene.

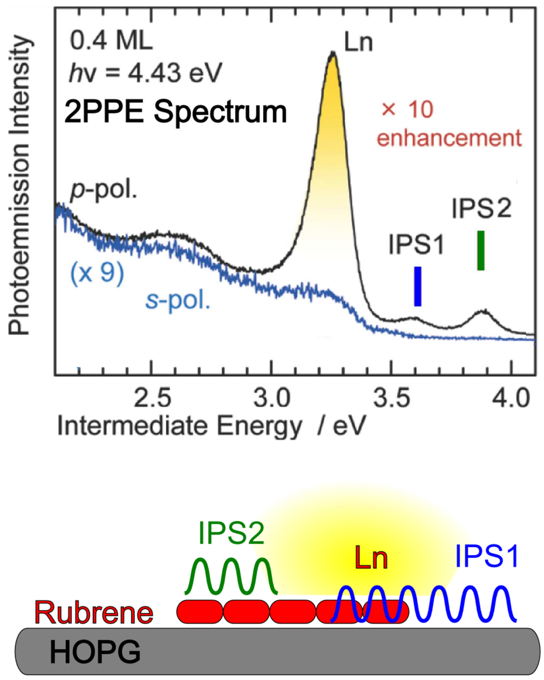

Fig. 1: *Ln-IPS1 mixing in 2PPE spectroscopy (top) caused by a penetration of the IPS1 wavefunction into the molecular islands.*

Spectroscopic studies of the HOPG/rubrene interface using two-photon photoemission (2PPE) show an enhanced, resonant excitation of a specific, unoccupied molecular orbital, which is labeled as Ln.

It is expected that the properties of the Ln excitation (Fig. 1) are influenced by an interaction with the image potential state of HOPG (IPS1) [1]. The interaction is expected at rubrene structures with large boundaries, were an effective mixing can occur. Here, photoemission electron microscopy (PEEM) combined with the 2PPE technique was used to localize the Ln excitation on the sample surface and gather further confirmations of the Ln-IPS mixing. Photon energy as well as film thickness dependence was investigated. Results of the experiments are as follows:

0.3 ML: Bare HOPG and well-formed islands without resonance

Sharp and short border without large interaction.

0.8 ML: Homogeneous coverage with partial resonant glow (Fig. 2)

The well-ordered structure at 0.3 ML was decomposed by the influence of additional molecules, leading to an irregular molecular arrangement with large boundary. The different intensities at the resonance energy indicate different electronic structures, which are caused by different crystal structures in combination with different structural details. On graphite single crystals, the change of the crystal structure was verified with low energy electron diffraction (LEED) and differential reflectance spectroscopy (DRS).

1.2 ML: Unstructured rubrene film without resonance

IPS1 is not present any more (no uncovered HOPG areas).

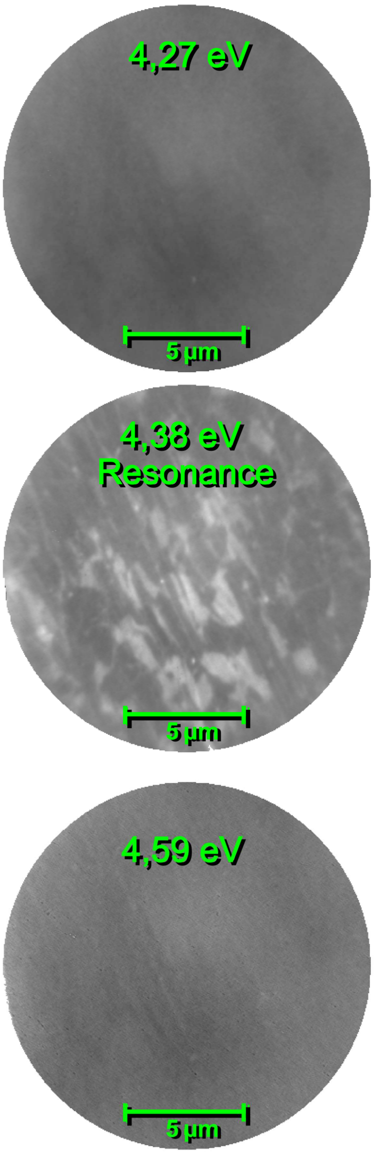

Fig. 1: *2PPE-PEEM images of the HOPG/rubrene interface at 0.8 ML coverage with resonant glow. Same position on the sample surface.*

The measurement results show that the Ln-resonance is linked to special molecular arrangements. However, the mechanism of the Ln-IPS mixing could not be clarified. Additional experiments, especially with scanning tunnel microscopy (STM), are planned.

Acknowledgments

This work results from a cooperation between the Munakata Laboratory (Osaka University) and the group of Prof. Fritz (Friedrich-Schiller-University Jena). I am very grateful to Prof. Toshiaki Munakata and Prof. Torsten Fritz who gave me the opportunity to work on this topic and organized a research stay at Osaka University.

References

[1] J. Park et al., J. Phys. Chem. C 116, 5821-5826 (2012)

Surface Modification of ZnO Nanowire with Plasma Treatments for Hydrogen Sensing

Davide Cammi, Christoph Bückmann, Carsten Ronning

ZnO nanowires are promising candidates as building components for miniaturized gas sensors [1,2]. They can be integrated as a semiconducting channel into electronic devices, and the presence of particular gas molecules can be detected as a change in the current when the device is exposed to the gas atmosphere. The high surface to volume ratio of the nanowires results in a considerably higher value of the gas sensitivity compared to other forms of the same material, such as thin films or bulk structures [3].

The sensing mechanism in ZnO relies on the interaction of the gas molecules with the surface states of the nanowire. This interaction usually results in an electron transfer between the conduction band and the surface states (in particular related to oxygen vacancies), where the electrons are localized. The direction of the electron transfer (from or to the conduction band) determines a corresponding measurable change in the current flow through the nanowire (decrease or increase, respectively). The proper modification of the surface state properties can therefore lead to an enhancement of the gas sensitivity of a ZnO nanowire device.

In this report, we present the effect of oxygen and argon plasma treatments on the hydrogen gas sensing properties of ZnO nanowire devices.

The nanowires were grown by the VLS [4] method and subsequently transferred to a new substrate (850 nm of SiO_2 on Si). After photolithography and metal deposition, the final devices consist of some nanowires bridging two Ti/Au electrodes (10nm/100nm). The samples were then glued on a commercial chip carrier and contacted by electrical bonding. The electrical measurements were carried out with a Source-Measure Unit (SMU) Keithley (Model 237) applying a voltage difference between the drain and the source electrodes. The devices were placed in a sealed chamber, connected to a nitrogen (used as an inert reference atmosphere) and a formier gas (5% hydrogen in 95% nitrogen) supply.

A typical example of the response of the nanowire to the hydrogen atmosphere is shown in Fig. 1. The current increases considerably when a flow of hydrogen (1000 ppm in nitrogen atmosphere) is let into the chamber. It is well known [5] that the surface of the ZnO is usually partially covered by adsorbed oxygen, which tends to trap electrons from the conduction band. The hydrogen molecules react with the oxygen and induce the release of these electrons from the surface states related to the oxygen vacancies back to the conduction band. The conductivity of the nanowire therefore rises and a corresponding increase of the current flowing through the device is observed.

Fig. 2 shows the effect of the oxygen plasma on the hydrogen sensitivity S, expressed as a relative change of the resistivity under the nitrogen atmosphere R_{N_2} and in presence of hydrogen R_{H_2}:

$$S = \frac{R_{N_2} - R_{H_2}}{R_{N_2}}.$$

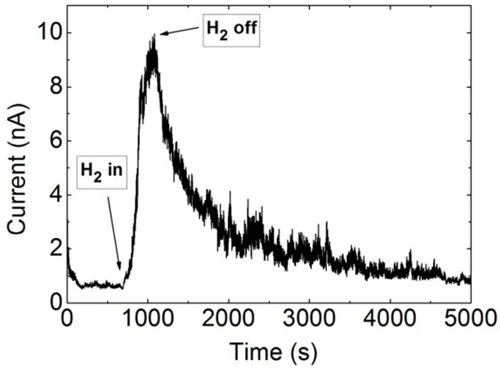

***Fig. 1:** Increase and decrease of the current in a single ZnO nanowire electronic device under exposure of hydrogen gas.*

Immediately after the treatment the sensitivity of the nanowire vanishes completely. After one week, it recovers up to the original value, which was measured before.

An argon plasma treatment, performed under the same conditions, results instead in a slight enhancement of the hydrogen gas sensitivity, as shown in Fig. 3.

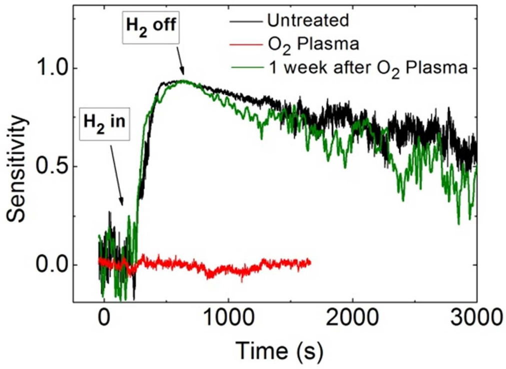

***Fig. 2:** Hydrogen gas sensitivity of a single ZnO nanowire electronic device before and after oxygen plasma. The treatment was performed at 100 sccm, 30 W, 0.7 mbar and for 60 s.*

According to previous studies [5,6], the concentration of ionic oxygen related species (O^- and OH^-) at the surface considerably increase after plasma treatment in oxygen. The effect of the argon plasma is instead the opposite: the surface concentration of these ionic species decreases and at the same time there is an increase of the oxygen vacancy concentration. Surface oxygen vacancies act, as already explained, as surface states where the reaction between the ZnO and the hydrogen molecules takes place. Therefore, it is reasonable that the higher concentration of surface oxygen vacancies induced by the argon plasma treatment results in an enhanced hydrogen gas sensitivity.

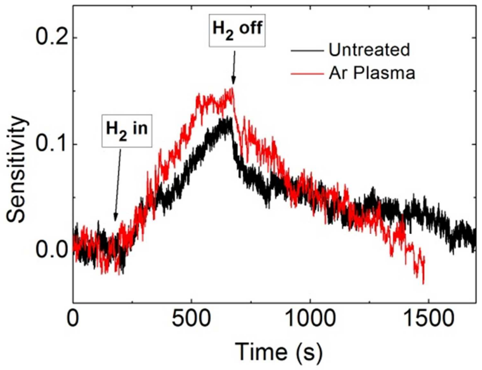

***Fig. 3:** Hydrogen gas sensitivity of a single ZnO nanowire electronic device before and after argon plasma. The treatment was performed at 100 sccm, 30 W, 0.7 mbar and for 60 s.*

References

[1] Q. Wan *et al.*, *Appl. Phys. Lett.* **84**, 3654-3656 (2004).

[2] Zhiyong Fand and Jia G. Lu, *Appl. Phys. Lett.* **86**, 123510- 123513 (2005).

[3] E. Brunet *et al.*, *Sens. Actuators B: Chem.* ***165***, 110-118 (2012).

[4] C. Borschers *et al.*, *J. Phys. Chem. B* **110**, 1656-1660 (2006).

[5] H. –W Ra *et al.*, *Mater. Lett.* **63**, 2516-2519 (2009).

[6] H. –W Ra *et al.*, *Appl. Phys. Lett.* **93**, 033112-033114 (2008).

Enhanced sputtering of gold nanoparticles

Henry Holland-Moritz, Christian Borschel, Sebastian Scheeler[1]*, Claudia Pacholski*[1] *and Carsten Ronning*

[1] *Max-Planck-Institut für Intelligente Systeme, Stuttgart*

Ion beam irradiation is one possible subsequent approach to tune the properties of materials. An important effect concerning the interaction of ions with nanoparticles (NPs) is sputtering, especially when the ion range is in the range of the particle size. [1] Therefore, it is important to understand the quantity of the sputtering effects and how sputtering affects NPs.

To determine the energy and size dependence of the sputter yield, Si samples with hexagonally arranged Au NPs on top, fabricated by the MPI Stuttgart [2], were used. The NPs show a broad diameter distribution, ranging from 35 to 80 nm. These samples were irradiated with Ga ions of energies from 1 to 30 keV in a focused ion beam system (FIB) with a fluence of 3e15 cm^{-2}. High resolution SEM images including about 1.000 NPs were taken before and after irradiation. It was possible to compare single NPs. Using the image analysis software *imagej*, the sizes of the NPs before and after irradiation were compared and the sputter yield calculated, assuming that the spherical shape of the particles is preserved. The results were compared with the simulation results by the Monte-Carlo-code *iradina* [3].

The results are shown in fig. 1. In both plots the solid lines show the simulation results of *iradina*. Fig. 1 (a) shows the energy dependence of the sputter yield. The maximum of the simulated curve indicates the energy, where the ion range is comparable to the NP size. With increasing energy, the amount of energy deposited in the bottom of the NP increases and the sputtering decreases. The data points show the experimental data. These are the average values of all measured sputter yields of certain energies. For all energies the sputter yield is larger compared to the simulation. Also the slope of the data points is steeper than *iradina* predicts.

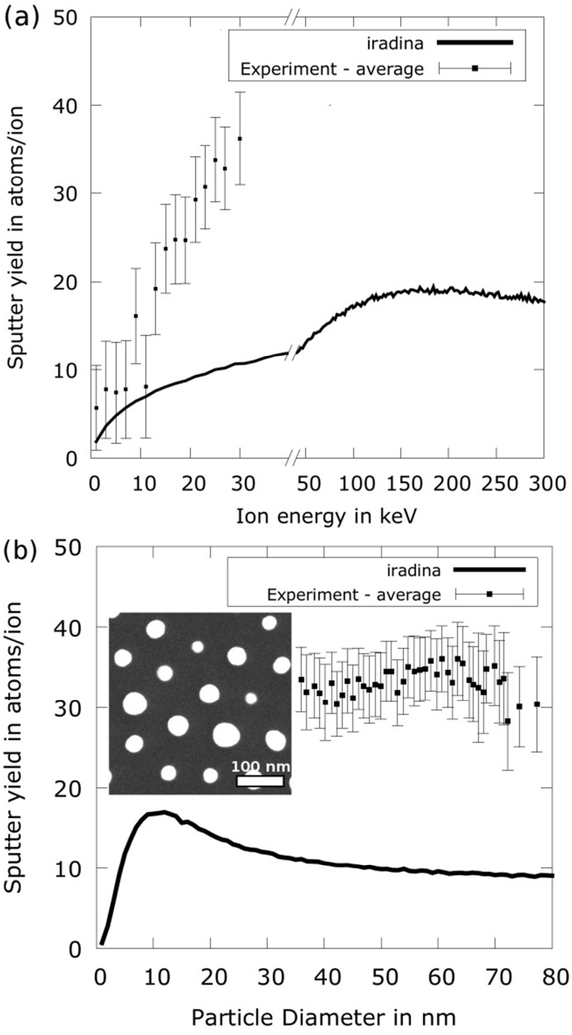

Fig. 1: *(a) Energy dependence of the sputter yield of Ga irradiated Au NPs. (b) Size dependence of the sputter yield. The inset shows a SEM image of the NPs after irradiation.*

In Fig. 1 (b) the data points show the average value of the sputter yield for a 1 nm sized interval of single particle sputter yields. The values of the single particles show a large straggling for NPs of comparable sizes. Molecular Dynamics (MD) simulations indicate ion channeling as a possible reason for this effect. [4] Since the NPs are spinned onto the substrate, their lattice orientation towards the ion beam is randomly distributed. This leads to different degeneration velocities, which we confirmed in an in situ experiment, where particles of the same initial size changed their size with variable speed. In any case, the experimental sputter yields are larger than the simulated results in Fig. 1 (b).

One reason for the disagreement between simulation and experiment is that the surface binding energy assumed in the code as 3 eV. For NPs this should be less compared to bulk, accurate values are not available in the literature. However, even with unrealistic small values of 0.1 eV, for example, it is not possible to explain the discrepancy between simulation and experiment. Therefore, the primary reason is that two major sputtering mechanisms are not taken into account in Monte-Carlo-simulations, like evaporative sputtering and cluster emission. The significance of these effects is shown by MD simulations. [4] MD simulations by Järvi et al. [5] show even larger sputter yields, but they neglect substrate interaction. We made experiments, which point out the importance of the effect of substrate interaction with NPs on sputtering. The inset in fig. 1 (b) shows a SEM image of the Au NP sample, which was irradiated with 25 keV Ga ions, after irradiation. There were no melting or deformation effects, which were found by introductory experiments, justifying the assumption of spherical particles even after the irradiation. According to these introductory experiments, melting effects occur at higher ion beam current densities than which were used in the above mentioned experiments.

In the present work, we showed a new approach of measuring the sputter yield on NPs, comparing single NPs using high resolution SEM images before and after Ga ion irradiation. We confirmed MD simulations results and showed the enhancement of the sputtering effects on NPs experimentally.

References

[1] T.T. Järvi *et al.*, Europhys Lett. **85**, 26002 (2008).

[2] S. Ullrich *et al.*, Part Part Syst Part **30**, 102-108 (2013).

[3] C. Borschel *et al.*, Nucl Instrum Meth B **269**, 2133-2138 (2011).

[4] G. Greaves *et al.*, Phys Rev Lett. **111**, 065504 (2013).

[5] T.T. Järvi *et al.*, Nucl Instrum Meth. **272**, 66-69 (2012).

Nano X-ray fluorescence quantification of dopants in nanowires

Andreas Johannes, Carsten Ronning, Claudia Schnohr, Pillipp Schöppe, Stefanie Eckner

Doping of semiconductors is a key way to manipulate their functionality. The same obviously holds for semiconducting nanowires. As doping during growth is difficult and sometimes impossible, ion beam doping has established itself as a standard technique of the semiconductor industry. Well established and tested software exist for the simulation of concentration and damage profiles in bulk samples [1]. However, the ion implantation into nanostructures with dimensions similar to those of the implanted ions' collision cascade is not so thoroughly investigated. This report focuses on an experiment to evaluate the results of the Monte-Carlo simulation software *iradina* [2].

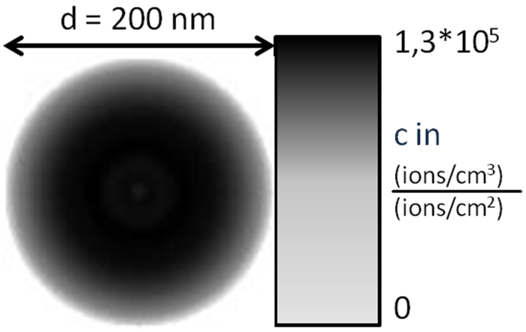

Fig. 1: *Result from iradina simulation. The linear grayscale shows a homogeneous radial concentration profile.*

The simulated concentration profile of a 200 nm ZnO nanowire (NW) irradiated with 175 keV Mn is shown in figure 1. To compare with the simulation, a wire array was irradiated at an angle of 45° and rotated under the ion beam as shown in figure 2. This improves the homogeneity of the implantation while minimizing the implantation energy needed to get homogeneous doping profiles. A lower implantation energy is beneficial as this reduces lattice damage to the sample. The average concentration per fluency [(ions/cm^3)/(ions/cm^2)] is calculated from the simulation. The fluency used in the implantation at the "ROMEO" implanter at the IFK were determined to yield nanowire samples with nominal concentrations of 0,01; 0,1; 1; 2; 4 and 8 at% Mn in ZnO.

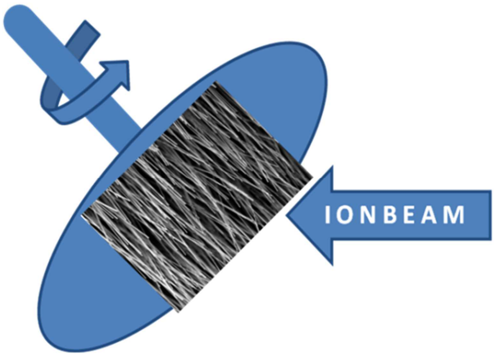

Fig. 2: *Schematic of the rotated implantation under an angle performed at the ROMEO Implanter.*

These wires were transferred to TEM grids and taken to the European Synchrotron Radiation Facility in Grenoble for quantitative X-ray Fluorescence (XRF) at the microfocus beamline ID13. Due to the absence of inelastic scattering background compared to Energy Dispersive X-ray quantification (EDX) the concentration resolution of XRF is at least an order of magnitude better with 0,1 at% compared to typical EDX resolution values of ~ at%. The spacial resolution of the microfocus beamline of ~ 200 nm enables the investigation of single NWs, previously identified in the SEM as shown in figure 3.

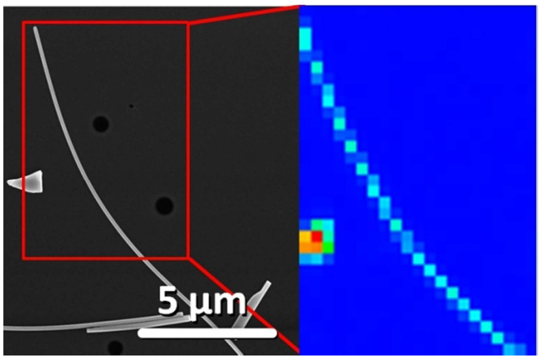

Fig. 3: *SEM Image (left) and nano XRF map (right) of a Mn implanted NW on a C-Foil TEM grid.*

By scanning the length of the NW with a relatively high integration time, it is possible to determine concentration profiles along the NWs implanted with different nominal concentrations. Figure 4 shows exemplary results from 3 nanowires of different nominal concentrations along the length of the wires. Note that the concentration is always higher than expected from the respective *iradina* simulations. This can be attributed to the fact that the simulation is static, thus neglecting the effect sputtering has on the concentration.

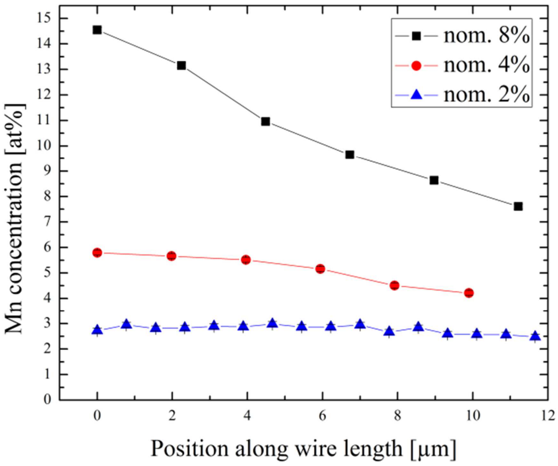

Fig. 4: *Plot of the nano XRF measured concentration for 3 different nominal concentrations over the length of a wire. Errorbar ≈ 0,1 at%.*

It is known and can be shown with *iradina* and other simulations [3], that the sputter yield is greatly enhanced for nanostructures. This arises from the fact that the surface area that contributes to sputtering is high. However, the reported simulation is static in the way that the sputtered ions are not removed and there is no relaxation of the geometry. Software solving this problem on a relevant scale is under development [4]. It is easy to see that removing the outer atoms from the wire in figure 1 will increase the average concentration within the wire.

Additionally, figure 4 shows a concentration gradient along the length of the wires. The slope of the gradient is greater for higher implantation fluencies and not strictly homogeneous among samples implanted with the same fluency (not shown). This is attributed to shadowing of the wires by each other and redeposition of sputtered material from one wire onto another. The variance of the concentration along the wire length is as large as the difference between the simulation and the experiment. Thus experiments with sparser NW arrays will have to be made to differentiate between sputtering, shadowing and redeposition.

We have shown, by accurate XRF quantification of the Mn dopant concentration in ion beam implanted ZnO nanowires, that the dynamic effect of sputtering and unwanted shadowing and redeposition are significant and have to be considered in simulations and future experiment designs.

References

[1] J.F. Ziegler *et al.* http://www.srim.org (2013)

[2] C. Borschel and C. Ronning, *Nucl. Instrum. Meth. B* **269**, 2133 (2011)

[3] T.Järvi *et al.*, *EPL.*, ***82***, 26002 (2008).

[4] B. Liedke *et al.*, *Nucl. Instrum. Meth. B* **316**, 56-61 (2013).

Measurement of gallium depth distribution by GIXRD

M. Oertel, Ph. Schöppe, C. Ronning

For high efficiencies of Cu(In,Ga)Se_2 thin film solar cells the distribution of the gallium content within the absorber layer is one of the most important factors [1]. Mainly sputter techniques are used to determine this Gallium gradient quantitatively [2]. A non-destructive technique is x-ray diffraction under very small incident angles (GIXRD) [3]. Due to the varying main information depth of the reflected x-rays at different incident angles one obtains depth dependent reflection patterns. One can obtain the Gallium depth distribution by the circumstance that the lattice constants a and c of Cu(In,Ga)Se_2 depend strongly on the gallium concentration. Unfortunatly, the intensity of the x-ray beam decreases exponentially within the layer depth. Though it never becomes zero, the diffraction patterns always contain information about the whole layer but with a different weighting. Thus, the shape of the reflection pattern contains the main information rather than the absolute 2θ-position of the maximum. To get quantitatively reliable results it's necessary to simulate diffraction patterns for each incident angle and fit them to the measured reflection patterns with one set of fitting parameters, which determine the Gallium grading. First, I. M. Kötschau applied this method to Cu(In,Ga)Se_2 thin films [4].

Our measurements were done with an URD65 x-ray diffractometer and a CuKα-X-ray source. The need of a very small divergence angle of the incident beam was fulfilled by the use of a 0.09 mm divergence slit in front of the sample. The divergence of the reflected beam was limited by a Soller-Slit with a length of 150 mm and a distance between the metal sheets of 0.2 mm. We investigated the reflection of the (112)-atomic plane of the chalcopyrite structure. This reflection has the advantages of a high intensity and that it does not overlap with other reflections.

To simulate the reflection pattern a mathematical description of the profile shape of the reflection is needed. A very suitable equation is a split PearsonVII-function [4].

$$\frac{I}{\left(\frac{\Gamma_l+\Gamma_r}{2}\right)\left(1+4\left(2^{\frac{1}{m_l}}-1\right)\left(\frac{2\theta-2\theta_M}{\Gamma_l}\right)^2\right)^{m_l}}, 2\theta \leq 2\theta_M \quad (1)$$

$$\frac{I}{\left(\frac{\Gamma_l+\Gamma_r}{2}\right)\left(1+4\left(2^{\frac{1}{m_r}}-1\right)\left(\frac{2\theta-2\theta_M}{\Gamma_r}\right)^2\right)^{m_r}}, 2\theta > 2\theta_M \quad (2)$$

Equation (1) describes the profile shape left of the maximum reflection angle $2\theta_M$ and equation (2) the one on the right side. Due to the splitting of the profile equation one can simulate asymmetric profiles, which are very common due to the instrumental function. $\Gamma_{l,r}$ is the corresponding full width at half maximum (FWHM) and $m_{l,r}$ is the corresponding shaping factor. The values of $m_{l,r}$ depend only on the instrumental function at each incident angle and therefore can be found by measuring a model crystal system with known crystal size distribution. We took the (111)-reflection of a silicon powder standard to determine the shaping factors.

The parameter I in (1) and (2) describes the reflected intensity. To calculate the intensity, an absorber layer model of thin parallel layers, schematically shown in Fig. 1, was used. Each thin layer differs in its gallium content and therefore in its lattice constants and mass attenuation coefficient.

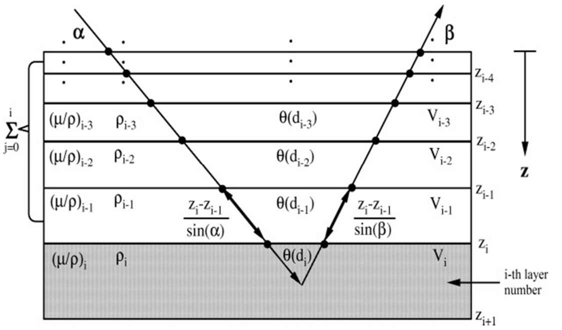

Fig. 1: *The model system of the absorber layer built of thin parallel layers with varying Gallium content [4].*

So, the information about the gallium depth distribution is in the mathematical description of the reflected intensity. To describe the gallium distribution (ggi) within the layer depth *z* the equation

$$ggi(z) = \frac{ggi_{min}-ggi_{max}}{1+\left(\frac{z}{z_w}\right)^{v}} \qquad (3)$$

was taken, where ggi_{min} is the Ga/(Ga+In)-ratio at the surface, ggi_{max} is the maximum ratio, z_w is the depth of the point of inflection and ν is proportional to the slope in z_W. This expression can describe a large variety of observed gallium profiles.

The whole model explained above was implemented in a Mathematica program, where the model parameters are changed till the simulation fits the measured data. Fig. 2 shows the measured patterns of the (112)-reflection of a Cu(In,Ga)Se_2-layer for different incident angles with their corresponding simulations. The hence extracted gallium depth profile is drawn in Fig. 3 where also a nano-XRF-measurement of the gallium profile of the same layer is shown. In comparison both measurements show a slight bowing of the gallium profile. The relatively strong increase of the nano-XRF-measurement in a depth of 1.8 µm is a measurement artifact due to the interface to the back contact. So the GIXRD-measurement reproduces the shape of the gallium profile very well. The slight offset of the GIXRD result is within the errors of both methods. The accordance of both methods shows that GIXRD-measurements in combination with the simulations of diffraction patterns are very suitable to determine gallium gradients in Cu(In,Ga)Se_2-thin films.

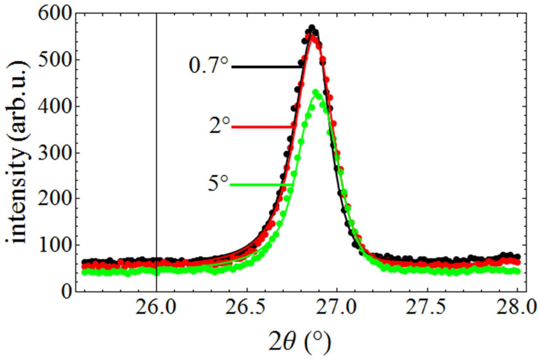

Fig. 2: *Measured GIXRD-pattern of the (112)-reflection of a Cu(In,Ga)Se_2-layer for incident angles of 0.7°, 2°, 5° (dots) with the corresponding simulations (lines).*

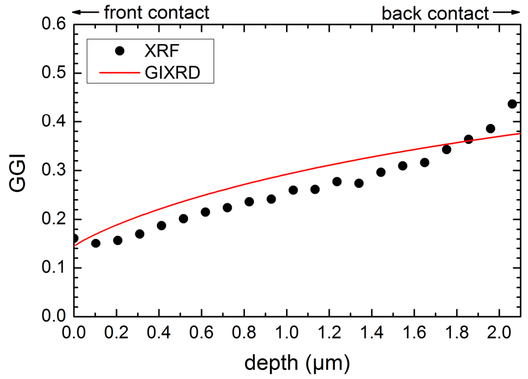

Fig. 3: *Comparison of XRF and GIXRD measurements of the Ga/(Ga+In)-ratio of a Cu(In,Ga)Se_2 absorber layer.*

Acknowledgement

We thank our colleagues of the IOQ for using their diffractometer and their assistance during the buildup of the GIXRD setup.

References

[1] A. Chirilă *et al.*, Nat. Mater. **10**, 857-861 (2011).

[2] D. Abou-Ras *et al.*, Microsc. Microanal.**17**, 728-751 (2011).

[3] I. M. Kötschau *et al.*, TSF **515**, 5992-5996 (2007).

[4] I. M. Kötschau, PhD Thesis, Universität Stuttgart (2003).

CdTe grown under Cd/Te excess at very low temperatures for solar cells

C. Heisler, M. Brückner, F. Lind, C. Kraft, U. Reislöhner, C. Ronning, and W. Wesch

A promising but also challenging approach to further decrease energy consumption and production costs of thin film CdS/CdTe solar cells is the reduction of substrate temperature during growth of the CdTe absorber. This would also allow the use of alternative substrates with lower thermal stability than the normally used glass panes, thereby also enabling lightweight and flexible photovoltaic modules.

We investigated the dependence of the substrate temperature and of material supply during absorber deposition on the composition of CdTe layers and interpreted the results with respect to the CdTe phase diagram.

All samples were prepared on commercial glass substrates with a fluorine doped tin oxide layer as front contact. While the CdS buffer layers were deposited by the close space sublimation process, the 3 to 4 µm thick CdTe absorber layers were deposited by a high vacuum PVD process. Additional evaporation sources in the PVD chamber allow the evaporation of elementary tellurium or cadmium simultaneously to the evaporation of CdTe in the main source. The investigated CdTe layers were grown with 3 different source combinations to modify the composition of the material beam: (A) using only the CdTe effusion cell, (B) using the CdTe effusion cell and the Te evaporation source at a temperature of 400 °C and (C) using the CdTe effusion cell and the Cd evaporation source at a temperature of 300 °C. In all cases the temperature of the CdTe effusion cell was 700 °C while the substrate temperature was varied between 45 and 300 °C. After the deposition of CdTe the $CdCl_2$-activation was performed at 380 °C for 40 min. A double layer of 3 nm Cu and 20 nm Au was used as back contact.

The Te:Cd ratio was investigated by *Energy-Dispersive X-ray Spectroscopy* and the parameters of the solar cells were measured under AM1.5 illumination.

It was found that the CdTe layers, which are deposited at a substrate temperature below 190 °C with the CdTe source (A) as well as with the CdTe source and an additional Te source (B) show a significant excess of Te (see Fig. 1).

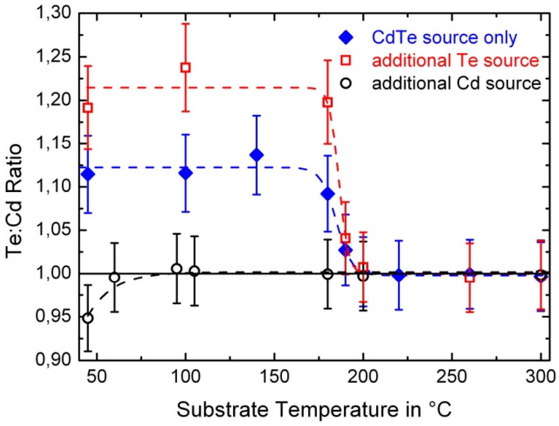

Fig. 1: *Te:Cd ratio of the CdTe layers grown under three different growth conditions as function of the substrate temperatures. The dashed lines serve as guides for the eye.*

Parallel to the occurrence of excessive Te, the performance of the solar cells with absorbers grown at substrate temperatures below this limiting temperature decreases abruptly, as shown in Fig. 2.

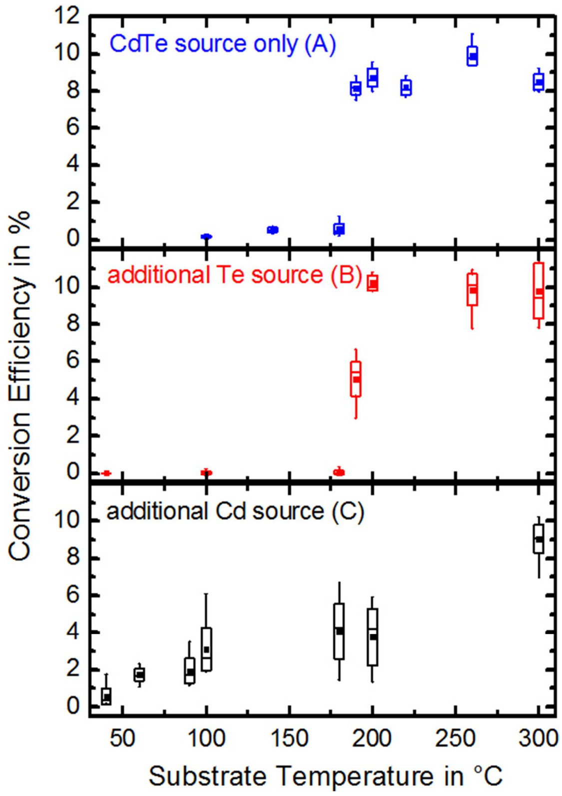

Fig. 2*: Characteristics of solar cells with CdTe absorber layers grown with three different material beams at different substrate temperatures.*

To understand this effect, the phase diagram of CdTe has to be considered. It is shown in Fig. 3 and represents the characteristics at a pressure of 1 bar. For the examination of a growth in high vacuum ambient different aspects have to be considered: (i) at low pressure, liquid phases of CdTe, Cd and Te do not exist and the materials sublimate to the gas phase, (ii) the evaporation temperature of the materials decreases with decreasing pressure. For a pressure of $5x10^{-7}$ mbar the sublimation temperatures of Cd and Te are 100 °C and 190 °C, respectively [1]. Consequently, elementary Cd and Te deposited in a high vacuum process will sublimate from the substrate and only stoichiometric CdTe will be deposited if the substrate temperature is higher than the temperature of the solidus-lines from Te and Cd. For substrate temperatures below the solidus-lines of Te, excessive Te will be deposited as exclusions in the CdTe layer. The evaporation temperature of Cd is lower than the evaporation temperature of Te and excessive Cd is deposited as exclusions only below the solidus temperature of cadmium.

With an additional Cd-source (C) the Te excess can be compensated, which allows the growth of stoichiometric CdTe layers below 190 °C. Finally, an adapted Cd-flux, lower than that used for the processes shown in Fig 2, enabled the production of solar cells with a conversion efficiency η=9% at a substrate temperature as low as 100 ° [2].

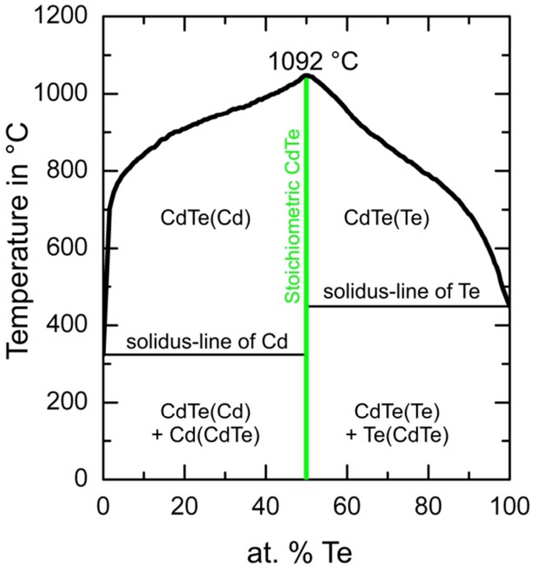

Fig. 3: *Phase diagram of CdTe at a pressure of 1 bar after Ref. [1].*

References

[1] A. Luque and S. Hegedus, Handbook of Photovoltaic Science and Engineering, John Wiley & Sons Ltd, Chichester, p. 623 (2003).

[2] Ch. Heisler et al., J. Appl. Phys. **113**, 224504 (2013).

Transparent CdTe solar cells with a ZnO:Al back contact

C. Heisler, C.S. Schnohr, M. Hädrich, M. Oertel, C. Kraft, U. Reislöhner, H. Metzner, and W. Wesch

CdTe solar cells which are transmitting a significant part of the incident light are a promising option for the use as top cell in a multi-junction solar cell configuration with expected conversion efficiencies of 25% [1]. Furthermore, transparent CdTe solar cells are also a very interesting option for architectural applications. In order to build transparent CdTe solar cells two crucial development steps have to be reached: First, to permit the transmission of the incident light the metallic non-transparent back contact has to be replaced by a transparent back contact. Second, due to the fixed band gap and the high absorption coefficient of CdTe the thickness of the CdTe-absorber must be reduced below 1 µm to increase the amount of light transmitted below 860 nm.

We used commercial Tec-7 glasses as substrates which were already coated with transparent conductive oxide (SnO_2:F). The CdS and the subsequent CdTe layer were deposited by close space sublimation in our baseline. The CdS layer thickness of all samples was 150 nm while the CdTe layers were varied in thickness from 0.2 to 5 µm by adjusting the deposition time. The CdTe layers were deposited at two different temperature sets: (i) with a crucible temperature of 660 °C and a substrate temperature of 480 °C and (ii) in a low temperature process where the crucible temperature was 620 °C while the temperature of the substrate was only 300 °C. The subsequent $CdCl_2$-activation process was performed at 380 °C for 40 min.

To study the influence of the absorber thickness on the device performance, a non-transparent Cu-Au back contact, consisting of a 3 nm thick Cu layer and a 20 nm thick Au layer, was applied.

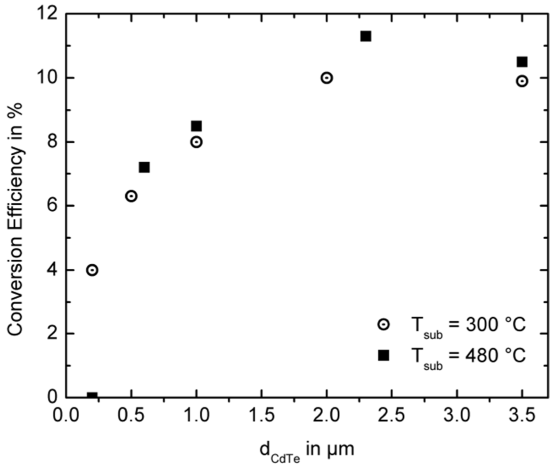

Fig. 1: *Conversion efficiencies of solar cells with high- and low-temperature CdTe absorber layers and different absorber thicknesses.*

The conversion efficiencies of the best solar cells are shown in Fig. 1 as a function of the absorber layer thicknesses. The solar cells with the low-temperature absorber layers exhibit slightly lower performances over most thicknesses. However, for extremely thin absorber layers with thicknesses of about 0.25 µm no operating high-temperature solar cells were found while an efficiency of 4 % was still observed for the solar cells with the low-temperature CdTe layer. Because low deposition temperatures are necessary for the fabrication of monolithic tandem solar cells in order to minimize or prevent the diffusion of the materials of the subjacent layer system, we identify the low-temperature process as most suitable.

For the fabrication of the transparent back contact, a bilayer of 1 nm Cu and 1 nm Au is deposited in a PVD process. Subsequently, the samples were annealed and a 250 nm ZnO:Al layer was deposited by an RF sputter process.

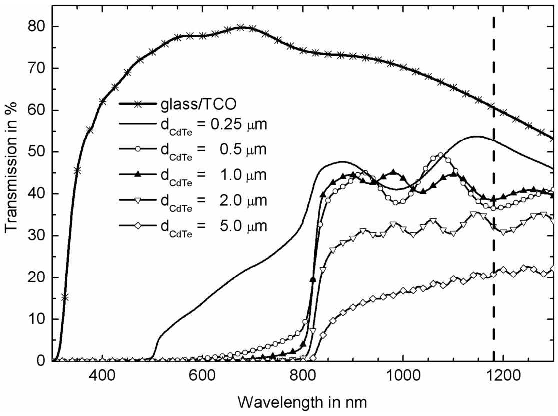

Fig. 2: *Transmission spectra of glass with TCO and of glass/TCO/CdS/CdTe layer stacks with different CdTe layer thicknesses between 0.25 and 5 µm. The dashed vertical line indicates the band gap of the CISe bottom solar cell.*

Fig. 2 shows the transmission spectra of the glass/TCO layer and of the glass/TCO/CdS/CdTe layers without back contact and different thicknesses of the absorber layers. The transmission of the TCO coated glass is high for all wavelengths. For the glass TCO/CdS/CdTe layer stack the incident light with wavelengths less than 500 nm is mostly absorbed by the CdS buffer layer in accordance with the absorption spectrum of CdS. Light with a wavelength between 500 and 800 nm is mainly absorbed in the CdTe absorber layer. Obviously, the transmission of light between 500 and 800 nm can be increased by reducing the thickness of the absorber layer to less than 1 µm. Because the optimal transmission of NIR light is a crucial requirement for the use of a CdTe solar cell as top cell in a multi-junction solar cell, the CdTe-thickness should not exceed 1 µm.

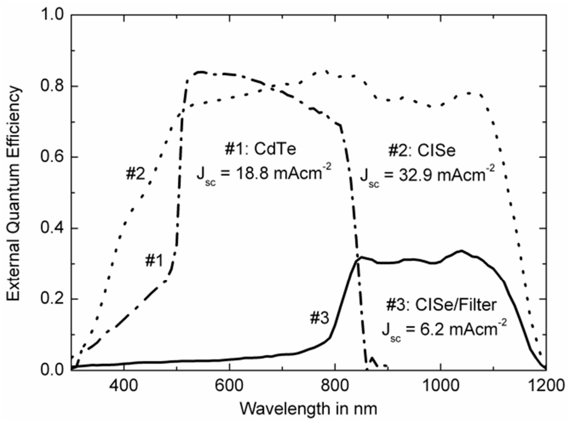

Fig. 3: *External quantum efficiencies of a CdTe solar cell (#1) and a CISe solar cell with (#3) and without (#2) the CdTe solar cell as filter.*

Fig. 3 shows the external quantum efficiency of a CdTe solar cell with such a back contact as top cell in a tandem configuration with a CISe-cell and thus demonstrates the potential application. The short circuit currents given in Fig. 3 were calculated from the EQE spectra. The quantum efficiency spectrum shows that the CdTe solar cell only uses light with wavelengths beneath 800 nm to generate photo current. The CISe solar cell with the CdTe/CdS cell as filter provides a short circuit current of more than 6 mA/cm² which can be used additionally in this tandem cell configuration. To minimize the reflection losses in the NIR spectrum a monolithic design of the proposed tandem cell concept should be applied. Thereby, the ZnO:Al back contact is applicable both as transparent back contact for the top and as an n-type front contact for the bottom cell. More details on this work are found in Ref. [2].

References

[1] R. Noufi et al., Proceedings of the IEEE 3rd World Conference on Photovoltaic Energy Conversion, Osaka, Japan, May 2003, p. 12.

[2] C. Heisler et al., Thin Solid Films 548 (2013) 627–631.

Growth and characterization of vanadium dioxide nanowires

Jura Rensberg, Matthias Ogrisek, Hannes Mähne[1]*and Carsten Ronning*

[1]*NamLab gGmbH Dresden, Germany*

Vanadium dioxide undergoes a metal-to-insulator transition (MIT) accompanied by a reversible first-order structural transition from a high-temperature tetragonal to a low-temperature monoclinic phase, at about 68 °C. As a consequence considerable changes in electrical resistivity and optical properties are observed making VO_2 an excellent candidate for numerous applications in optical, electronic, and optoelectronic devices. The growth of high-quality VO_2 films with bulk-like electronic properties and high crystalline quality is still challenging. Enormous strains exist at the interfaces to the substrate, mainly due to the differences in the crystal lattice parameters and thermal expansion coefficients between the thin film and the substrate [1]. For this reason, nanostructures are of particular relevance, as stress can quickly relax laterally e.g. in nanowires, allowing growth with very high crystal quality [2]. A well-known process for fabricating nanowires is the vapor-liquid-solid (VLS) growth technique [3]. However, it is reported that vanadium dioxide nanowires can be generated directly from the vapor-phase in the absence of a metal catalyst (vapor-solid growth, VS) simply by thermal evaporation of solid source material [4].

Here, we report on the successful growth of vanadium dioxide nanowires. Conditions for the growth of VO_2 nanowires were adapted from literature [4 - 7] as well as adjusted and optimized to a 3-zone tube furnace. Commercial VO_2 powder as source material was placed in an alumina boat and heated up to 1325 K allowing evaporation. Substrates, both with and without a thin Au film acting as metal catalyst, were placed at the cooler end of the tube furnace. The vapor was transported at a pressure of ~100 mbar by Ar gas flow of 20 sccm to the substrates

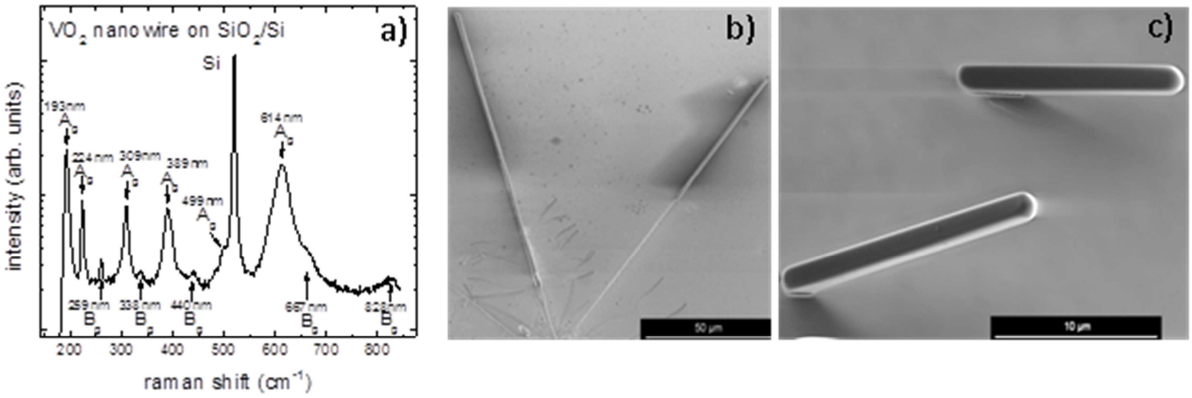

Fig. 1: *Raman investigations at room temperature confirm the VO_2 nature of the grown nanowires (a). The SEM images show, that VO_2 nanowires grow in-plane on a thick SiO_2 layer (b), whereas on r-plane Al_2O_3 the growth direction is out-of-plane (c).*

initiating the growth process of nanowires. Energy-dispersive X-Ray spectrometry (EDX, not shown) revealed only vanadium and oxygen signals. The Raman spectrum of as-deposited nanowires measured at RT is shown in Fig 1(a). The phonon modes can be uniquely assigned [8] confirming the VO_2 nature of the nanowires. The morphology of the nanowires was studied by scanning electron microscopy (SEM). As it can be seen in Fig 1(b), the as deposited VO_2 nanowires on thick SiO_2/Si display in-plane growth and are typically up to 200 µm long and between 1 and 2 µm in diameter. Since no major difference between the growth on gold coated and uncoated substrates was found, we conclude that the growth mechanism is VS.

Out of plane growth of the nanowires was achieved by using r-plane sapphire substrates, compare Fig. 1(c). Although the nanowires on these substrates are only of several 10 µm length, out-of-plane growth enables the mechanical dispersion onto a clean substrate for further experiments.

In future experiments the nanowires will be contacted for electrical characterization on top of insulating substrates using deposition and/or lithography methods. Furthermore, upstanding nanowires allow homogeneous ion implantation giving rise to new and tunable electrical and optical properties.

References

[1] Wong *et al.*, J. Cryst. Growth **364**, 74 (2013).

[2] Mandl *et al.*, Nano Lett. **6**, 1817 (2006).

[3] Wagner *et al.*, Appl. Phys. Lett. **4**, 89 (1964).

[4] Cheng *et al.*, J. Cryst. Growth **311**, 1571 (2009).

[5] Guiton, American Chemical Society **127**, 489 (2005).

[6] Chou *et al.*, J. Appl. Science **105**, 034310 (2009).

[7] Maeng *et al.*, Materials Research Bulletin **43**, 1649 (2007).

[8] Schilbe, Physica B **316-317**, 600 (2002).

Thermal stability and ion beam modification of VO_2 thin films

Jura Rensberg, Sebastian Vatterodt, You Zhou[1], Shriram Ramanathan[1] and Carsten Ronning

[1] *School of Engineering and Applied Sciences, Harvard University, Boston, USA*

The metal-to-insulator transition (MIT) in vanadium dioxide (VO_2) at a critical temperature T_C of about 68 °C induces significant changes in electrical, optical and structural properties and can be triggered not only thermally but also electrically. This makes VO_2 thin films very promising for integrated devices like ultra-fast switches, sensors, and memories [1]. It is desirable to reduce T_C to ambient temperatures for most applications. It is known that the critical temperature can be decreased by as much as ~ -20 K/at.% by the incorporation of tungsten into the VO_2 lattice [2]. However, doping of VO_2 thin films during growth is limited to vertical incorporation of dopant profiles. In contrast, ion beam doping allows also for lateral doping using suitable masking techniques such as optical or electron beam lithography. Furthermore, the dopant concentration and implantation depth can be well controlled via the ion fluence and the ion energy. The major disadvantage of doping by ion implantation is the high concentration of defects created by the implantation process, making in-situ or post implantation annealing necessary.

In this study we examined the possibility of doping VO_2 by ion implantation. For this purpose 100 to 200 nm thick VO_2 films were deposited onto c-Al_2O_3 substrates by rf-sputtering. Further details for the film preparation have been described elsewhere [3]. The structural stability of VO_2 under ion bombardment was investigated using 75 keV Ar^+ ion irradiation and 1.4 MeV He^+-Rutherford backscattering spectrometry in channeling geometry (RBS/C). Since argon is not incorporated in the lattice, only effects related to irradiation damage occur and can be investigated separately. The implantation depth was calculated to be 50 nm using the simulation program SRIM [4]. Furthermore, it was calculated that an ion fluence of

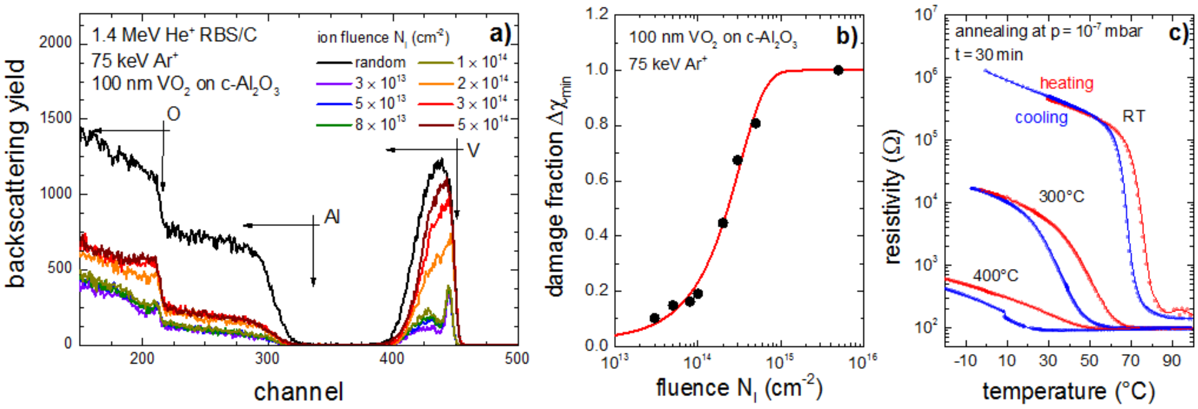

Fig. 1: *(a) 1.4 MeV He^+ RBS/C spectra of VO_2 thin films on c-Al_2O_3. The samples were irradiated with 75 keV Ar^+ and different ion fluences. (b) The damage fraction $\Delta\chi_{min}$ can be calculated as a function of the ion fluence using the vanadium backscattering signal. (c) Annealing VO_2 in high vacuum at a base pressure of 10^{-7} mbar leads to a reduction of both the critical temperature T_C of the MIT and the resistivity change due to oxygen out-diffusion.*

5×10^{15} cm^{-2} is required to achieve a nominal doping concentration of ~ 1 at.% in a depth of 50 nm.

Fig. 1(a) shows RBS/C spectra of 100 nm thin films of VO_2 on c-Al_2O_3 prior to and after irradiation. When the He^+ ion beam is aligned with the [010]-axes of un-irradiated VO_2, in particular the backscattering yield of vanadium is strongly reduced compared to a random orientation of the film. With increasing ion fluence N_I the backscattering yield of vanadium increases and reaches almost random values at an ion fluence of 5×10^{15} cm^{-2}. This can be attributed to the formation of point defects and defect clusters by ion beam damage. The damage fraction $\Delta\chi_{min}$ is therefore given as backscattering yield of vanadium for He ion incidence parallel to [010]-axes of VO_2 divided by the backscattering yield for random incidence. VO_2 is completely amorphized ($\Delta\chi_{min}$ ~ 1) at an ion fluence of 1×10^{15} cm^{-2}, as it can be seen in Fig. 1(b) for such irradiation conditions. Since the ratio of the damage cross section for all ion species can be simulated, this is a universal curve for VO_2 valid for all implantation species. Thus, ion beam doping with appropriate ion concentrations in order to reduce T_C is not possible without further treatment, making in-situ or post implantation annealing necessary.

Thus, the possibility of ion irradiation at higher ion implantation temperatures was investigated. VO_2 thin films were placed on a sample holder in the irradiation chamber, slowly heated to annealing temperatures of 300°C and 400°C, respectively, and kept at these temperatures for 30 minutes. A base pressure of 10^{-7} mbar commonly used for ion irradiation experiments was used. Afterwards the electrical properties of the films have been investigated in the temperature range from below room temperature up to 100°C by measuring their temperature-dependent resistivity in van der Pauw geometry. These measurements are summarized in Fig 1(c). The untreated sample shows a MIT with a change in resistivity by about 3 orders of magnitude at a temperature of about 70°C. With increasing annealing temperature the resistivity change at the MIT vanishes and the samples become metallic in the whole temperature range. We believe that this is caused by oxygen out-diffusion. Furthermore, T_C decreases and the hysteresis width increases with increasing annealing temperature. Additionally, an implantation temperature of 400°C is not sufficient to prevent amorphization of the samples, if they are irradiated with 75 keV Ar^+ ions and an ion fluence of 5×10^{15} cm^{-2}.

Here, we have reported about ion beam irradiation of Vanadium dioxide thin films. Ion fluences of about 1×10^{15} cm^{-2} lead to an amorphization of VO_2 and thus a loss of MIT properties. We have found out, that irradiation at higher temperatures utilizing dynamic annealing is not applicable to VO_2 due to oxygen out-diffusion under high-vacuum conditions. Therefore, future experiments will focus on post implantation annealing to recover the lattice structure after ion implantation.

References

[1] Leroy *et al.*, Appl. Phys. Lett. **100** 213507 (2012).
[2] Wong *et al.*, J. Cryst. Growth **364** 74 (2013).
[3] Tang *et al.*, Phys Rev. B **31** 1000 (1985).
[4] http://www.srim.org/.

Continuous wave nanowire lasing

Robert Röder, Marcel Wille, Sebastian Geburt, Mengyao Zhang[1], Jia Grace Lu[1],
Federico Capasso[2] and Carsten Ronning

[1] University of Southern California, Department of Physics and Astronomy
[2] Harvard University, School of Engineering and Applied Science

The forthcoming limitations of conventional electronic integrated circuits cause reinforced work in the field of nanophotonics to develop new concepts for circumventing the drawbacks of electrical interconnects by on-chip optical data transmission and processing [1]. Semiconductor nanowires are promising building blocks for on-chip optoelectronic components, as they are functional and connecting units in both electronics and photonics. They furthermore mark, due to efficient waveguiding [2], the lower size limit of a photonic laser system [3, 4]. Single nanowire laser oscillations have been demonstrated for a lot of materials ranging from the UV spectral range to the NIR only at pulsed optical pumping [5], as high pumping powers are required to establish the population inversion responsible for light amplification. Thus, further improvement for future integration in optoelectronic devices will be gained by nanoscaled continuous wave (cw) emitting coherent nanowire based light sources.

The drawback of nanowire lasing at cw optical pumping remains therefore in managing the thermal budget, since “off” times are missing, which allow the thermal power to dissipate. In this study, the pumping threshold for cw lasing is therefore lowered to values, at which the heating is nearly negligible, by using CdS based nanowire material providing high optical gain values up to 10^4 cm^{-1} and a perfect resonator structure. High quality CdS nanowires are synthesized by thermal transport using a tin catalyst resulting in Sn doping of 1-4 at.% during growth [6]. Single CdS:Sn nanowires reveal very high quality single-crystalline lattice structure with a plane spacing of $\approx$ 0.67 nm along the c-axis in good agreement with literature, as shown in Fig. 1, and hints for extended defects such as stacking faults or dislocations are missing.

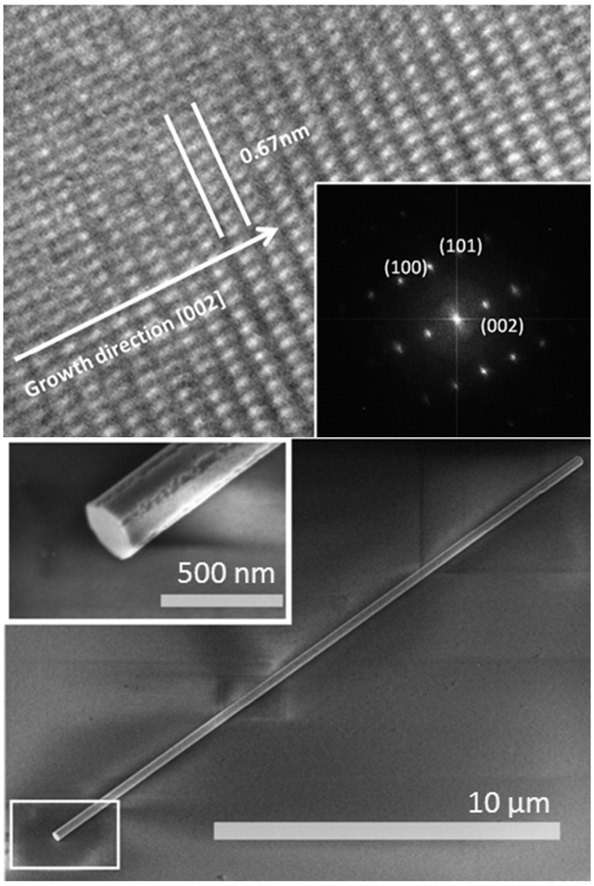

Fig. 1: *Top: HRTEM image of a CdS:Sn nanowire showing single crystalline structure with growth direction along c-axis. Inset shows the respective FFT pattern. Bottom: SEM image of the CdS:Sn nanowire (diameter ~300 nm, length 19.9 µm) with smooth end facets lying on a SiO$_2$/Si Substrate. The nanowire is therefore well suited as laser resonator.*

The high optical quality of single CdS:Sn nanowires exhibiting perfect resonator structure, like in Fig. 1, is proven by the absence of the defect based luminescence in microphotoluminescence (µPL) meausurements. Power dependent µPL spectra of the waveguided emission, which is originating from the smooth facet ends of the nanowire, are shown in Fig. 2a. A broad spontaneous emission band superimposed with intensity modulations indicating Fabry-Pérot oscillations governs the spectra below 2 kW/cm², while above this value sharp, equidistant modes evolve at the low energy side of the spectrum. At high optical pumping above 6 kW/cm², the stimulated modes dominate the spectra with negligible spontaneous emission. The optical power, which is emitted from the single nanowire as function of the optical pumping is presented in Fig. 2b. The characteristic S-shaped course in the double-logarithmic plot as well as the return to a linear slope above 6 kW/cm² proves the cw laser oscillation in single CdS:Sn nanowires at 4K and is consistent with a multimode laser model [7]. The cw laser emission of a single nanowire is extremely bright, thus it can be seen with unaided eye at ambient light conditions.

In conclusion, the high quality nanowire resonator together with the high optical gain material show extreme low lasing thresholds, enabling continuous wave (cw) nanowire lasing up to 120K, which is most likely caused by an electron-hole plasma upon high pumping powers [8].

References

[1] B. Piccione *et al.*, Nat. Nanotechnol. **7**, 640-5 (2012).

[2] T. Voss *et al.*, *Nano Lett.*, *7*, 3675-80 (2007).

[3] M. Zimmler *et al.*, *Semicond.Sci. Tech.* **25**, 024001 (2010).

[4] S. Geburt *et al.*, *Nanotechnology* **23**, 365204 (2012).

[5] Y. Ma *et al.*, Adv. Opt. Photon. **5**, 216 (2013)

[6] M. Zhang *et al.*, Nano Lett. (submitted).

[7] L. W. Casperson *et al.*, Appl. Opt. **14**, 1193-99 (1975).

[8] R. Röder *et al.*, Nano Lett. **13**, 3602-06 (2013)

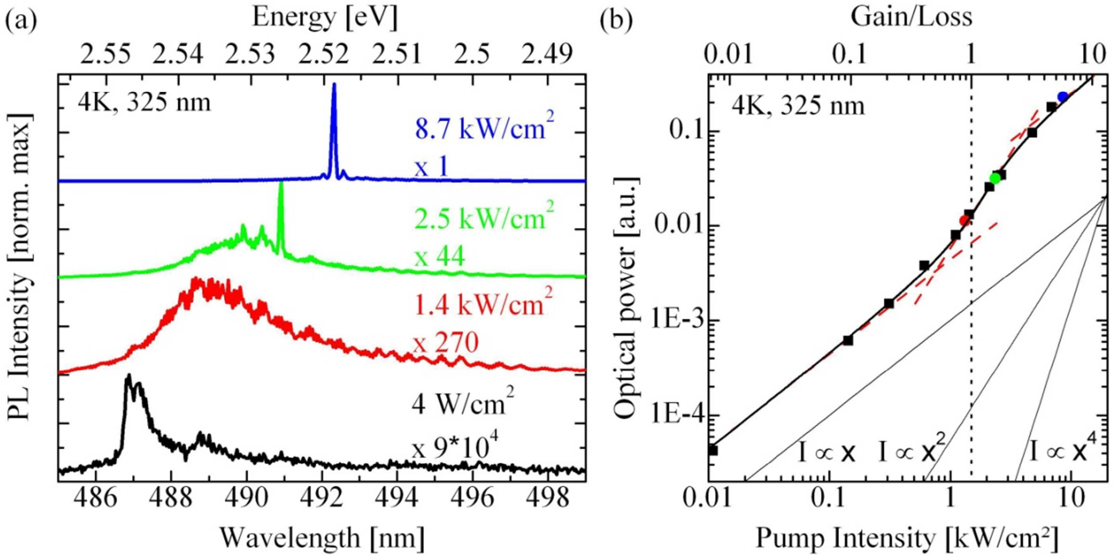

Fig. 2: *(a) The µPL end facet spectrum at 4K (325 nm excitation) shows spontaneous emission at moderate cw excitation of 4 W/cm². At higher excitations above 2 kW/cm², longitudinal laser modes evolve and dominate the spectra above 6 kW/cm². (b) The integrated PL intensity versus pump power clearly proves cw lasing by fitting the data with a laser model.*

Atomic-scale structure of Cu(In,Ga)Se_2 powders and thin films

C. S. Schnohr, H. Kämmer, S. Eckner, T. Steinbach, M. Gnauck,
C. A. Kaufmann, C. Stephan*, S. Schorr*,[§]*

** Helmholtz-Zentrum Berlin für Materialien und Energie, Hahn-Meitner-Platz 1,*
14109 Berlin, Germany
[§] Institut für Geologische Wissenschaften, Freie Universität Berlin, Malteserstr. 74-100,
12249 Berlin, Germany

Cu(In,Ga)Se_2 thin film solar cells have reached record efficiencies of more than 20 % not only on conventional glass substrates [1] but also on flexible polymer foils [2] thus offering a wide range of novel applications in the fields of architecture and product design.

The electrical properties of the absorber layer, such as the bandgap energy or the doping characteristics, are strongly influenced by the material composition. Typical high efficiency solar cells are slightly In rich and Cu poor with an In/III = In/(In+Ga) ratio of 0.60 to 0.70 and a Cu/III = Cu/(In+Ga) ratio of 0.80 to 0.90 [1]. However, the composition is not homogeneous throughout the absorber layer and may vary significantly as a function of depth.

Apart from the electrical properties, the composition also influences the structural parameters of the material. Cu(In,Ga)Se_2 crystallizes in the chalcopyrite type crystal structure shown schematically in Figure 1 with lattice constants *a* and *c* varying linearly with the In/III ratio.

While the long-range crystallographic structure is accessible with X-ray or neutron diffraction, extended X-ray absorption fine structure (EXAFS) spectroscopy provides structural parameters on the nanometre scale. Recent EXAFS studies of Cu(In,Ga)Se_2 powder samples clearly demonstrated that the local atomic arrangements strongly deviate from the average crystallographic structure [3,4]. The anion position, in particular, depends sensitively on the kind of group-III first nearest neighbours (In or Ga) and therefore on the composition. This in turn influences the material bandgap [5] and thus the device performance. We have now extended these studies to polycrystalline absorber layers as used in thin film solar cells.

Cu(In,Ga)Se_2 powder samples were synthesized by solid state reaction from the pure elements while polycrystalline thin films with thicknesses of 2-3 µm were prepared on glass/Mo substrates by a three-stage co-evaporation process. The composition of the material was determined by wavelength dispersive X-ray analysis and X-ray fluorescence analysis, respectively. EXAFS measurements of the Cu, Ga and In K-edge were performed at 17 K at Beamline C of HASYLAB (DESY) in

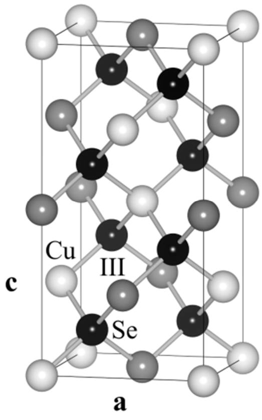

Fig. 1: *Schematic showing the chalcopyrite type crystal structure of Cu(In,Ga)Se_2.*

Hamburg. While the powder samples were measured in transmission mode, the spectra of the as-grown thin films were detected in fluorescence mode. Details of the experiment and subsequent data analysis are given in Ref. [3].

Figure 2 plots the element-specific Cu-Se, Ga-Se and In-Se bond lengths as a function of the In/III ratio for $Cu(In,Ga)Se_2$ powder samples and polycrystalline thin films. In all cases, the values for powders and thin films agree within experimental uncertainty and can thus be considered identical. Consequently, all conclusions previously drawn for $Cu(In,Ga)Se_2$ powders [3,4] are also valid for the polycrystalline absorber layers.

In particular, the element-specific bond lengths are very different from each other and remain close to the values of the ternary compounds despite a significant change of the lattice constants. This behaviour is very similar to that of other tetrahedrally coordinated semiconductors and originates from the fact that bond bending is energetically favoured over bond stretching [6,7]. As a result, the local atomic arrangements deviate significantly from the long-range crystallographic structure and the anion is displaced from the ideal tetrahedral lattice site depending on the neighbouring cation configuration. The material is thus characterized by structural inhomogeneity on the nanometre scale even if compositional fluctuations or secondary phases are absent.

Regarding the structural relaxation of the Se anion, two different mechanisms have to be distinguished, namely a displacement with respect to Cu and group-III atoms and a displacement with respect to In and Ga atoms [3]. These two mechanisms are distinctly different regarding the direction of the relaxation, the magnitude of the displacement and the influence on the bandgap. Overall, structural relaxation of the anion with respect to In and Ga contributes significantly more to the experimentally observed bandgap bowing than relaxation with respect to Cu and group-III atoms [4]. A similar behaviour was also observed for $Cu(In,Ga)S_2$ indicating that these findings represent general features of mixed chalcopyrite semiconductors [4].

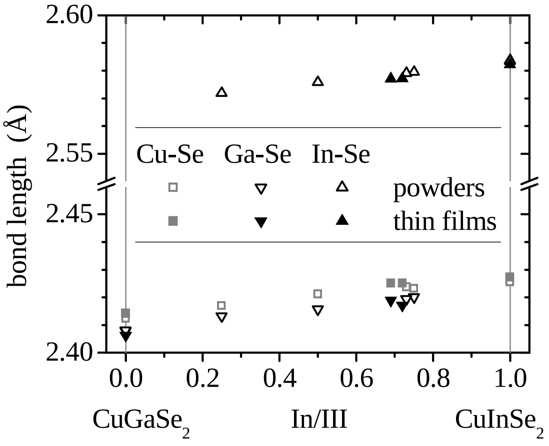

Fig. 2: *Element-specific bond lengths measured at the Cu, Ga and In K-edge as a function of the In/III = In/(In+Ga) ratio for* $Cu(In,Ga)Se_2$ *powders and thin films. The uncertainty of the values is 0.002 Å and thus similar to the size of the symbols. Note the break in scale for the bond length.*

References

[1] P. Jackson *et al.*, Prog. Photovoltaics **19**, 894-897 (2011).

[2] A. Chirila *et al.*, Nature Mater. **12**, 1107-1111 (2013).

[3] C.S. Schnohr *et al.*, Phys. Rev. B **85**, 245204 (2012).

[4] S. Eckner *et al.*, Appl. Phys. Lett. **103**, 081905 (2013).

[5] J. Vidal *et al.*, Phys. Rev. Lett. **104**, 056401 (2010).

[6] C.S. Schnohr *et al.*, Phys. Rev. B **78**, 115201 (2008).

[7] C.S. Schnohr *et al.*, Phys. Rev. B **79**, 195203 (2009).

Electron beam induced current measurements on CuIuSe$_2$ solar cells

S. Schönherr, Ph. Schöppe, M. Oertel, U. Reislöhner and C. Ronning

Electron beam induced current (EBIC) measurements can be used to visualize the depletion region in semi-conductor junction structures and is a common method to investigate carrier collection in semiconductor devices. In thin film solar cells it is more often used to localize recombination centres, for examples in CIGSe [1] or in CdTe solar cells [2]. Local fluctuations in the solar cell material properties are reported to be a limitation for high efficient solar cells [3]. The main advantage of EBIC measurements in a scanning electron microscope is the direct correlation to the morphology. Defects localized in EBIC measurements could be linked to the real structure of the specimen. The most common application of EBIC for the characterisation of Cu(In,Ga)Se$_2$-solar cells is in cross-section geometry. This allows characterizing the pn-junction and the absorber layer down to the back contact. Possible shunts can be detected and conclusion on the preparation of the cells can be made.

A CuInSe$_2$-solar cell was fabricated in a sequential process. First, a multi-layer system containing copper and indium on top of a molybdenum back contact was deposited by DC - magnetron sputtering. Afterwards, the metallic precursor was reactively annealed in two steps in a selenium vapour atmosphere, where it converted to an about 2 µ*m* thick CISe$_2$ absorber layer. Completing the solar cell, a CdS buffer layer was deposited via chemical bath deposition and as front contact a ZnO layer was sputtered on top.

This solar cell was broken in order to measure it in cross-section and no further treatment was conducted. The front and back contact were contacted with two indium dots, which were pressed on the top of the specimen. The electrical contact was checked via current-voltage measurements. As scanning electron microscope a *FEI Helios NanoLab 600i FIB* was used with current densities between 20 pA up to 2 nA and acceleration voltages from 2 kV to 30 kV.

Figure 1 shows a SEM image of a typical cross-section of the CuInSe$_2$-solar cell. The Mo layer is clearly visible on top of the glass substrate, as well as the 2 µm absorber layer with typical grain sizes and on top the transparent front contact. Conspicuously, in some regions the absorber lost the contact to the back contact and this shouldn't lead to a current in the fallowing EBIC measurements.

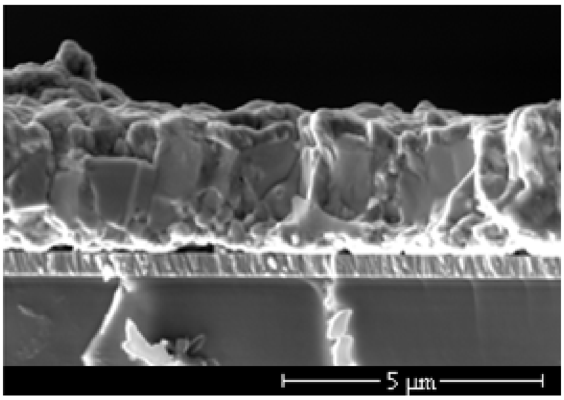

Fig. 1: *Scanning electron microscope image of a cross-section from a CuInSe$_2$-solar cell for the correlation with the EBIC images.*

In figure 2 the corresponding EBIC image is shown, measured with different acceleration voltages from 30 kV to 5 kV. A current up to 50 nA was detected and amplified.

The grain structure is well seen, as well as in the SEM image. Furthermore, current fluctuations were detected in regions, where the front contact got loose from the absorber during the preparation of the cross-section. This is well seen in the darker grain on the left side of the EBIC image. This grain is smaller than the surrounding ones and has no contact to the ZnO layer. To characterize such grains more in detail, the acceleration voltage of the SEM has to be decreased to reduce the excitation volume in the sample.

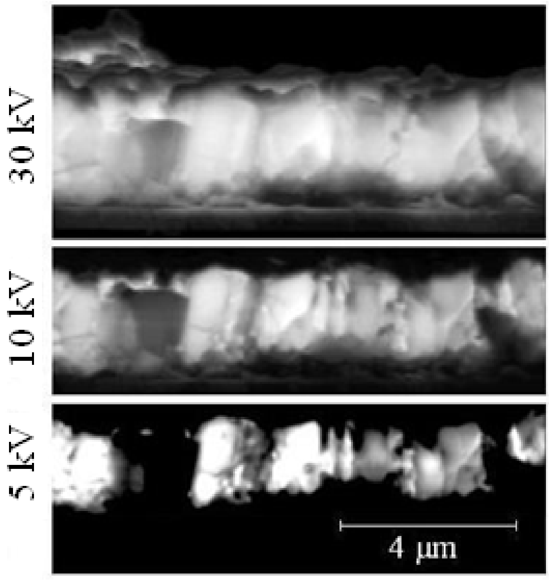

Fig. ***2:*** *EBIC images taken with different acceleration voltages of the same region as shown in figure 1.*

As consequence, the measured current decreases but the lateral resolution increases. For 5 kV the generation volume is small enough to excite only single grains. Grains without direct connections to the contacts give no longer a contribution to the EBIC signal. The grain without a front contact on the left side of the image shows no EBIC signal for low voltages. This means that this grain is separated from the surrounding ones and the carriers cannot move across the grain boundaries to the front contact of another grain.

For a better comparability, the EBIC image was dyed red and was superimposed on to the SEM image (figure 3).

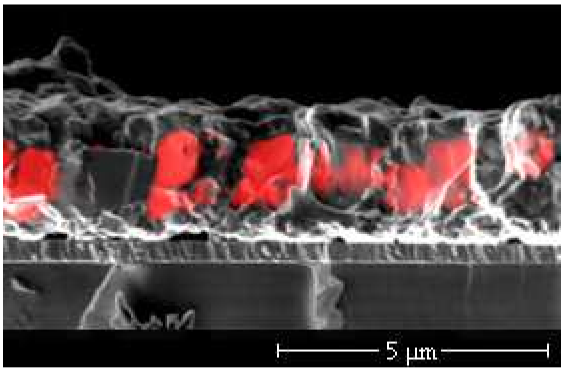

Fig. 3: *Red dyed EBIC image taken at 5 kV added to the SEM image of figure 1.*

Notably, there are regions with no contact to the Mo back contact, which contribute to the EBIC signal. Probably there is a good connection to other grains so that the generated current flows across surrounding ones to the back contact. Further regions, especially on the right side of the EBIC image, show no EBIC signal next to the back contact. This can be explained by the bad quality of the cross-section with detached contacts. Additionally, during the preparation the cell didn’t break with smooth edges and so the lower absorber layer protrudes. To eliminate these effects and to create smooth edges the cross-section will further prepared via sputtering in a focused ion beam system.

References

[1] Wätjen *et al.*, Solar Energy Materials & Solar Cells **107**, 396-402 (2012).

[2] P.R. Edwards *et al.*, Thin Solid Films, **372**, 284-291 (2000)

[3] Grabitz *et al.*, Thin Solid Films, **487**, 14-18 (2005).

Improved preparation of CIGSe-lamellas with a focused ion beam

Philipp Schöppe, Alexander Kusch, Claudia Sarah Schnohr, Andreas Johannes, Stefanie Eckner, Sven Schönherr, Udo Reislöhner, Manfred Burghammer[1)]*, Carsten Ronning*

1) European Synchrotron Radiation Facility, B.P. 220, F-38043 Grenoble Cedex, France

The efficiency of CIGSe solar cells depends on the structure and the stoichiometry of the absorber layer. There exist a lot of methods like XRF, EDX, TEM, XRD etc. in order to get chemical and structural information. We improved the spatial resolution of XRF and EDX by investigating thin lamellas of the CIGSe solar cell.

The lamellas were prepared using a Focused Ion Beam (FIB). Therefore, a piece of the solar cell is cut out by gallium ion sputtering and mounted on a TEM grid. Afterwards the mounted sample is thinned using gallium ions with stepwise reduced ion beam energies down to 8 keV or less. Thus, the surfaces of the lamella, which were damaged by the high energy gallium ions, are removed and only a thin damaged surface layer is left.

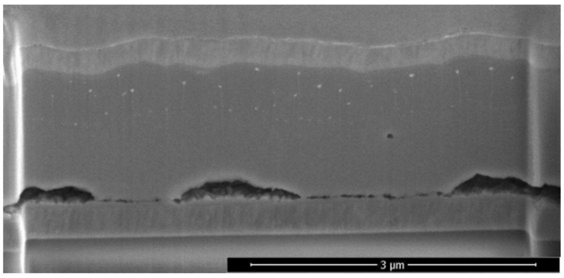

Fig. 1: *SEM picture of a CIGSe lamella with precipitates (white spots) created during preparation by FIB.*

A picture of a CIGSe lamella is shown in figure 1. As it can be seen in the image precipitates occur in the absorber due to the energy, which is brought in by the gallium ions. Thus, a diffusion process starts at which the precipitates are formed. These precipitates differ chemically from the originally absorber [1], and the area around them also has a disturbed stoichiometry. Hence, a chemical characterization of the absorber would be very difficult if the precipitates have to be taken into account.

The variation of beam energy and current showed no improvement of the situation. Abou-Ras et al. [2] suggested the use of XeF_2 as a reactive gas during the ion beam milling process in order to reduce the formation of the agglomerates. The fluorine is highly reactive, and enhances the sputter process by etching. We used the reactive gas during the last step of ion beam milling. A SEM picture of such a prepared lamella is shown in figure 2. No more agglomerates on the absorber surface are now observed, as the agglomerates created before were completely removed and no new ones are formed. The disadvantage when using XeF_2 so far is that the protective platinum layer vanishes very fast.

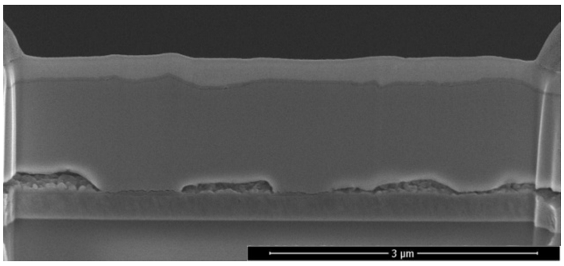

Fig. 2: *SEM picture of CIGSe lamella prepared with FIB, XeF_2 was used during the last step of milling.*

The lamella shown in figure 3 was measured by scanning transmission electron microscopy (STEM). The absorber has a polycrystalline structure, which is displayed in figure 3. The size of the grains is in the order of 1 µm. The interface between the absorber and the molybdenum back contact shows big holes, which probably lead to a reduced efficiency of the solar sell.

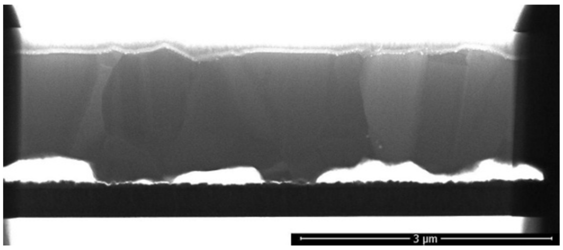

Fig. 3: *STEM picture of CIGSe lamella shown in figure 2.*

X-ray fluorescence (XRF) measurements were done on the CIGSe lamellas in order to analyze spatially resolved the composition of the absorber. An X-ray beam with a diameter of 200 to 300 nm was used to investigate the thin lamellas, which had a thickness between 60 and 1000 nm. As mentioned before the typical grain size is in the order of one µm. Hence, the nano beam XRF on lamellas offers the opportunity to get information even from a single grain.

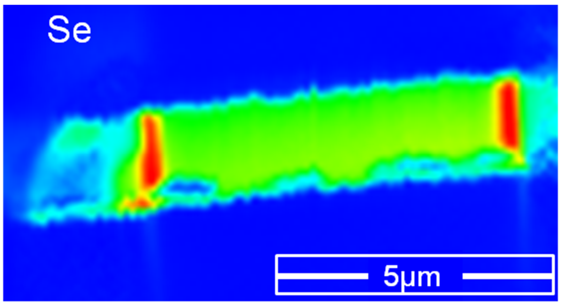

Fig. 4: *Se-concentration map taken by XRF of the CIGSe lamella, which is also shown in figure 2 and 3.*

As an example figure 4 shows a Se-concentration map of the lamella from figure 2 and 3. The concentration was determined by XRF. The Se signal is clear detected in the absorber, but it is not confined to the absorber. There is a Se signal at the interface to the back contact. It is particularly well seen below the holes. This gives an advice that a $MoSe_2$ layer is formed.

References

[1] J. Y. Lee e*t al*., Surf. Interface Anal. **44**, 1542-1546 (2012).

[2] D. Abou-Ras *et al*., Micron **43**, 470-474 (2012).

Cu diffusion in In_2S_3 layers and Meyer-Neldel rule

Albert Juma[1], Henry Wafula[2], Paul Pistor[1], Steffen Fengler[1],
Elke Wendler and Thomas Dittrich[1]

[1]Helmholtz-Zentrum Berlin für Materialien und Energie, Berlin, Germany
[2]Masinde Muliro University of Science and Technology, Kakamega, Kenya

Cu diffusion in thin In_2S_3 films is not well studied but important for the performance of chalcopyrite solar cells with In_2S_3 buffer layers or for the development of solar cells based on ZnO-nanorods/In_2S_3/CuSCN. Cu was found to diffuse from $Cu(In,Ga)(S,Se)_2$ or from CuSCN into In_2S_3 during an annealing step in air at temperatures of about 200 °C, which is mandatory for optimal solar cell performance (for details see [1] and references therein).

Cu diffusion was studied in different In_2S_3 layers which were thermally evaporated (PVD) or deposited onto c-Si wafers by spray-ILGAR [2] from 25 mM solution of $In(acac)_3$ or $InCl_3$ precursor salt dissolved in ethanol. An In_2S_3 layer thickness of 100 nm was used for the presented experiments. A CuSCN source layer was spray-spin coated onto the c-Si/In_2S_3 from a 0.11 M or 0.05 M solution of CuSCN in n-propyl sulphide (for details of preparation see [1, 3]). The c-Si/In_2S_3/CuSCN-substrates (dimension of about 2.5 cm×2.5 cm) were separated to several samples which were used for annealing in air for 5 min at annealing temperatures T_A between 150 °C and 250 °C. Cu diffusion was studied by Rutherford backscattering spectrometry (RBS).

Figure 1 shows a typical set of RBS spectra measured on In_2S_3(PVD) layers after annealing and removal of the CuSCN source layer. It can be seen that the Cu signal is well separated which allows the determination of the corresponding Cu depth distributions.

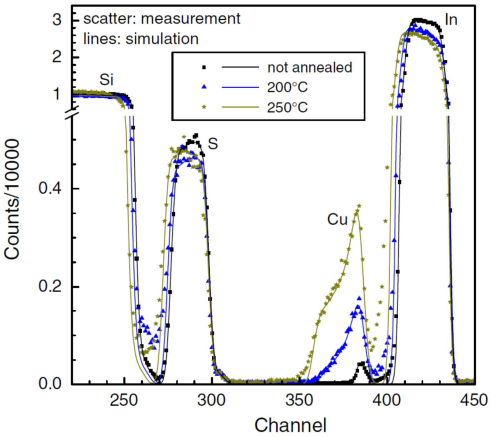

Fig. 1: *Measured RBS spectra for In_2S_3(PVD) layers on c-Si for different annealing temperatures as well as for an untreated reference. Solid lines correspond to simulated spectra with specific concentration profiles of Cu.*

Copper profiles and the increasing concentrations at higher T_A can be simulated by taking the diffusion coefficient as a free parameter. The value of the diffusion coefficient can be obtained by comparing measured and simulated Cu profiles for each temperature. In this procedure the high Cu concentration at the surface was omitted because it is independent of the annealing temperature, caused by deposition and etching of the source layer. For our experiments, the one dimensional diffusion equation with a source term was simulated with a simple recursion formalism (see [1] and references therein). Measured and simulated profiles of the Cu concentration in In_2S_3(PVD) layers are plotted in Fig. 2 for annealing temperatures of 175, 200, 225 and 250 °C. Good agreement between measured and simulated profiles of the Cu concentration was reached with diffusion coefficients of D_{Cu} = $(3.1\pm0.5)\times10^{-14}$, $(4.3\pm0.4)\times10^{-14}$, $(8\pm2)\times10^{-14}$ and $(8.8\pm0.3)\times10^{-14}$ cm^2/s for T_A=175, 200, 225 and 250 °C, respectively.

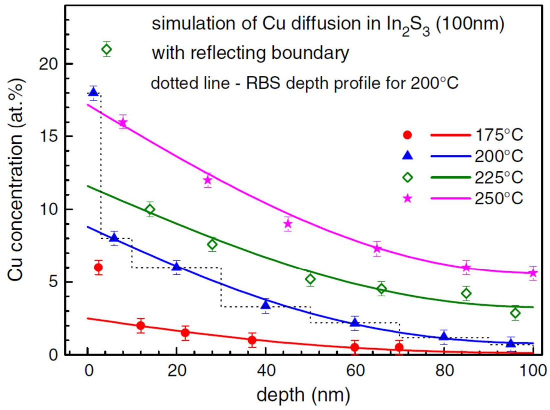

***Fig. 2:** Comparison of measured (scatter) and simulated (lines) concentration profiles of Cu after 5 min of annealing at different temperatures. The diffusion coefficient of Cu in In_2S_3(PVD) was adjusted for best agreement between measured and simulated data [1].*

Atomic diffusion is a thermally activated process that obeys the Arrhenius relation

$$D_{\mathrm{Cu}} = D_0 \exp\left(-\frac{E_{\mathrm{A}}}{k_{\mathrm{B}}T}\right), \qquad (1)$$

where D_{Cu} is the diffusion coefficient, D_0 the diffusion pre-factor, k_B the Boltzmann constant and T the temperature. From the diffusion coefficients given above an activation energy E_A of 0.3 eV for the In_2S_3 (PVD) layer could be determined [1]. In a similar procedure, activation energies of Cu diffusion in the In_2S_3(acac) and In_2S_3(Cl) layers were obtained [3].

Often a relation between the pre-factor D_0 and the activation energy E_A is observed according to

$$D_0 = D_{00} \exp\left(\frac{E_A}{E_{MN}}\right) \qquad (2)$$

which is called Meyer-Neldel rule with D_{00} and E_{MN} – the so-called Meyer-Neddel energy - being temperature-independent constants (for further references see [3]). E_{MN} was obtained from the slope of the graph in Fig. 3 by fitting the data with Eq. (2) and amounted to 40 meV. This value is in good agreement with data from literature for atomic diffusion, which range between 25 and 250 meV [4, 5].

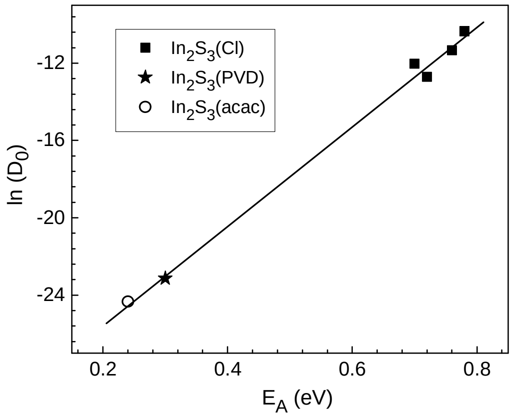

***Fig. 3:** Natural logarithm of the diffusion pre-factor (D_0) as a function of the activation energy (E_A) for Cu diffusion in different In_2S_3 layers.*

References

[1] A. O. Juma *et al.*, Thin Solid Films **520**, 6740-6743 (2012).

[2] R. Sáez-Araoz *et al.*, Prog. Photovolt: Res. Appl. **20**, 855-861 (2012).

[3] A.O. Juma *et al.*, J. Appl. Phys., accepted for publication.

[4] K. Shimakawa and A. Aniya, Monatsh Chem. **144**, 67-71 (2013).

[5] J. Shinar *et al.*, Phys. Rev. B **43**, 1631-1636 (1991).

Low-temperature damage formation in ion-implanted SiC and its correlation with primary energy deposition

Elke Wendler, Markus Schilling and Lutz Wendler

<0001> 4H-SiC samples were implanted with 45 keV He$^+$, 120 keV B$^+$, 180 keV Mg$^+$ and 200 keV Ar$^+$ ions. The implanted layers are about 300 nm thick. The ion fluence N_I varies between 5×10^{11} and 1×10^{16} cm^{-2}. Damage analysis was done by Rutherford backscattering spectrometry (RBS) in channelling configuration using 1.4 MeV He$^+$ ions and a backscattering angle of 170°. Ion implantation and subsequent damage analysis were carried out at (15±2) K in one target chamber without changing the temperature and the environment of the samples [1]. From the RBS channelling spectra the relative concentration of randomly displaced lattice atoms, n_{da}, versus depth z was calculated (for details see [2]). Here only the maximum concentration, n_{da}^{max}, is considered, taken as a mean value over 35 nm.

Figure 1 summarises the damage concentration n_{da}^{max} as a function of the ion fluence N_I for the different ion species implanted. Additionally results for 360 keV Ag$^+$ ion implantation are included [3]. The damage evolutions for the various ion species are rather structureless and a continuous transition towards amorphisation is observed (see Fig. 1). Such a behaviour can be well described assuming that two processes occur: (i) damage formation within a single ion impact with the cross-section σ_d and (ii) stimulated growth of damage which already exists from previous ions with the cross-section σ_g. These two processes can be represented by the relation (see [2] for details)

$$n_{da}(N_I) = 1 - \frac{\sigma_d + \sigma_g}{\sigma_g + \sigma_d \exp\left[\left(\sigma_g + \sigma_d\right) N_I\right]}. \qquad (1)$$

The model curves were fitted to the experimental data by minimising the chi-square by applying the Levenberg-Marquardt algorithm and using the uncertainty Δn_{da}^{max} for each data point as a weighting factor. The uncertainties caused by the statistics of the backscattering spectra and caused by determination and reproducibility of the ion fluence are taken into account (for details see [2]).

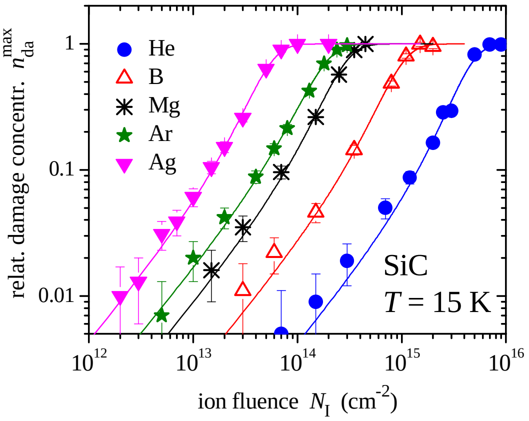

***Fig. 1:** Damage concentration in the maximum of the measured distribution versus ion fluence for various ions species implanted into SiC at 15 K. The lines are fitted to the experimental data using Eq. (1) (for details see text).*

It is expected that for the implantation conditions chosen here in SiC the energy deposited in the displacement of lattice atoms is mainly responsible for damage formation. This energy can be represented by the cross-section σ_{SRIM} (for details see [2]) and therefore, the experimentally obtained damage cross-sections σ_d and σ_g are plotted in Fig. 2 as a function of σ_{SRIM}.

The results observed are very similar to those for III-V compounds [3,4]. Figure 2 shows that for both quantities a clear correlation with σ_{SRIM} is observed. In the case of direct-impact-damage formation, the corresponding cross-section σ_d exhibits a dependence on σ_{SRIM} which is between a linear and a quadratic one. The cross-section σ_g of stimulated growth of damage increases linearly with σ_{SRIM} (see Fig. 2). A weighted linear fit of σ_g versus σ_{SRIM} through the origin yields a pre-factor of 17.9±0.8 which close to that for III-V compounds of 15±5 [4].

In the case of III-V compounds an empirical dependence of σ_d on σ_{SRIM} and S_e, the energy per ion and per unit depth deposited in electronic interactions, was found [4] which is given by

$$\sigma_d = \xi \frac{\sigma_{\mathrm{SRIM}}^{1.8}}{S_e}. \tag{2}$$

To check this equation for SiC, the product $\sigma_d S_e$ is plotted as a function of σ_{SRIM} and the function $\sigma_d S_e = \xi\,(\sigma_{\mathrm{SRIM}})^B$ is fitted to the experimental data thus obtaining the parameters ξ and B. For the automatic fitting procedure, the total errors, as explained in Ref. [2], are taken as weighting factors. The parameters are obtained to be B = 1.85±0.7 and $\xi = (0.6\pm1.4)\ \times10^{23}$ eVcm$^{-13/5}$. Comparing these numbers with those for III-V compounds, it becomes obvious that the exponents B are in very good agreement with each other. Setting B fixed to be 1.8, $\xi = (1.08\pm0.08)\ \times10^{22}$ eVcm$^{-13/5}$ is obtained. This is larger than the corresponding value obtained for III-V compounds [2, 4].

These results suggest universal dependences to occur for all common semiconductors. With the empirical formulas it becomes possible to predict low-temperature damage formation for any ion species implanted in any of these semiconductors. These results serve as starting point for further modelling including substrate temperature and ion flux. However, further data are required for confirmation of the empirical dependences and for determination of the corresponding parameters.

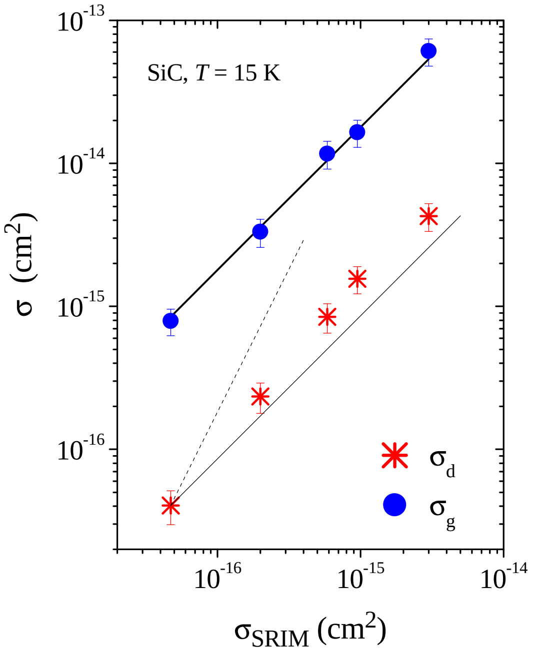

Fig. 2: *Cross-section σ_d of direct-impact-damage formation and σ_g of stimulated growth of damage versus the cross-section σ_{SRIM} of formation of primary displacements for SiC implanted at 15 K. The thick solid line is a linear fit to the experimental data of σ_g through the origin using the errors as weighting factors. The thin solid and dashed lines represent a linear and quadratic dependence on σ_{SRIM}, respectively.*

References

[1] B. Breeger et al., Nucl. Instrum Methods Phys. Res. B **174,** 199-204 (2001).

[2] E. Wendler et al., Vacuum, in press.

[3] E. Wendler et al., Nucl. Instrum. Methods Phys. Res. B **268**, 2996-2999 (2010).

[4] E. Wendler, L. Wendler, Appl. Phys. Lett. **100**, 192108 (2012).

Swift heavy ion irradiation of crystalline CdTe

T. Steinbach, Th. Bierschenk, M.C. Ridgway*, W. Wesch*

**Australian National University, Research School of Physics and Engineering, Canberra, Australia*

Cadmium telluride (CdTe) is a preferred material for use as an effective absorber in thin film solar cells, and for the optimization of the absorber properties ion irradiation can be used. It has been previously shown for low and medium ion energy irradiation (dominating nuclear energy deposition) that CdTe is relatively radiation resistant and shows damaging behaviour different to that of elemental and III-V semiconductors ([1] and references therein).

In order to study the effect of high electronic energy deposition on structural modifications, CdTe single crystals were irradiated with 185 MeV Au^{13+} ions at room temperture and incidence angles of 0° and 45° corresponding to electronic energy depositions of $S_e \approx 20$ keV nm^{-1} and 28 keV nm^{-1}, respectively, and subsequently analysed by means of Rutherford backscattering channelling spectroscopy (RBS/C) and cross-section transmission electron microscopy (cs-TEM).

The depth distributions of the relative defect concentrations n_{da} calculated from RBS/C spectra are depicted in Fig. 1 for irradiation at 0° and 45° ion incidence. Whereas at low ion fluences the defect profiles are constant over the depth and increase with ongoing irradiation, at fluences above $N_I \approx 1x10^{13}$ cm^{-2} with increasing ion fluence a pronounced peak close to the surface (z < 0.3 µm) is formed For the highest ion fluence used the maximum defect concentration amounts to $n_{da} \approx 0.7$ for perpendicular incidence, whereas for the irradiation at 45° $n_{da} = 1$ within a 100 nm thick surface layer which is commonly attributed to the existence of an amorphous layer. In contrast, the defect concentration in the depth is nearly constant and amounts to $n_{da} \approx 0.14$ for the highest fluence used.

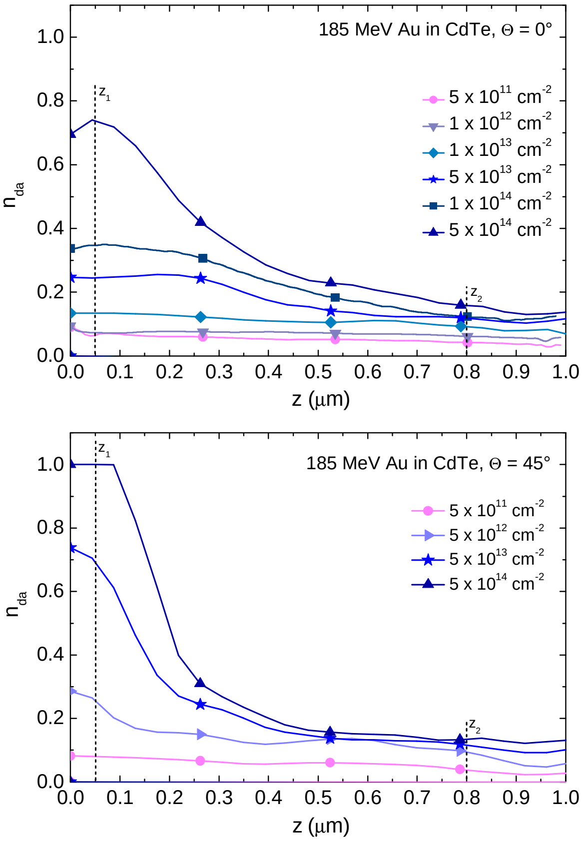

Fig. 1: Relative defect concentration n_{da} versus depth z for CdTe irradiated with 185 MeV Au ions at incidence angles of Θ = 0°(top) and 45° (down) [1]

The results of the TEM analysis of the sample containing the heavily damaged surface layer (Fig. 1, lower part) are shown in Fig. 2. In the cs-TEM image (Fig. 2a) a ≈ 140 nm thick modified surface layer can

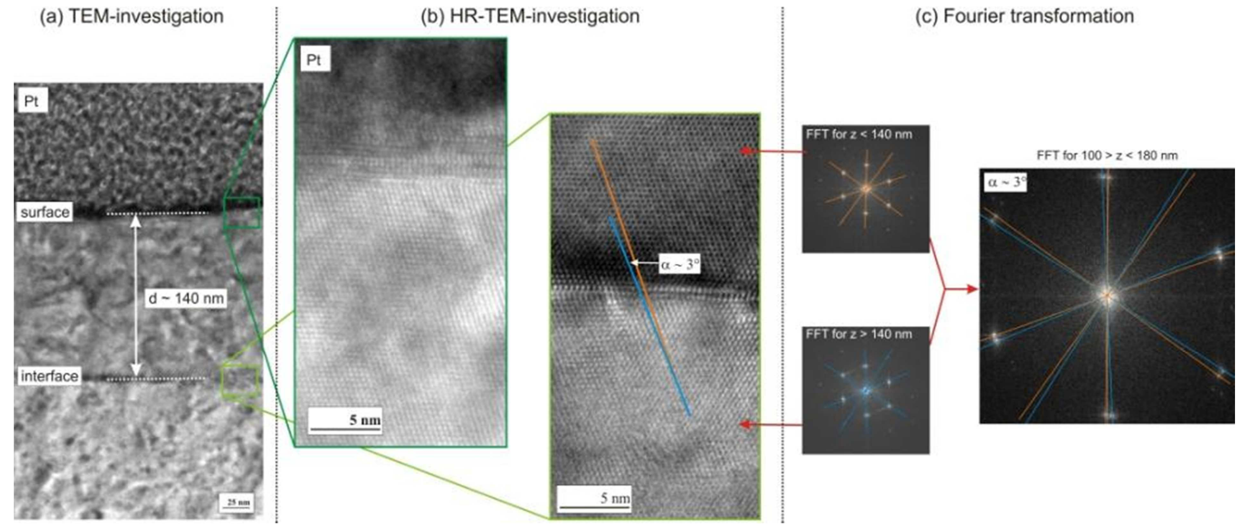

Fig. 2: Cross-section TEM ((a) and (b)) and Fourier transformation (c) of c-CdTe irradiated with 185 Au ions under 45° to an ion fluence of $N_I = 5x10^{14}$ cm^{-2}. The Pt-layer on the sample surface was deposited for the FIB lamellae preparation [1].

be identified which is separated from the underlying CdTe by an interface and corresponds to the strongly damaged layer observed by RBS (Fig. 1, lower part). The high-resolution images (Fig. 2b) indicate that both the surface layer and the underlying CdTe possess a high crystalline quality. This is also confirmed by the corresponding Fourier transformations (FFT) which are depicted separately for each region in the left FFT-images in Fig. 2c. These images show several single peaks for both regions. Contrary, for the Fourier transformation over both regions (i.e. the CdTe-CdTe interface) each peak appears twice (right FFT-image in Fig. 2c). This leads to the conclusion that the orientation of the c-CdTe surface layer is rotated by an angle of α = 3° compared to the underlying substrate. This rotation can also be seen in Fig. 2b, where the planes are rotated by α = 3°.

In case of lower ion fluences as well as for irradiation at 0° TEM analysis does not reveal separate surface layers, i.e. α = 0°. However, the surface layers ($z < 200$ nm) are characterized by a high concentration of extended defects (not shown) [1].

The TEM investigations reveal a strong resistance of CdTe with respect to damage formation and amorphization due to high electronic energy deposition. High fluence irradiation does not lead to the formation of stable point defects or amorphous tracks. The high concentration of extended defects in the near surface may induce mechanical stress which results in the observed rotation. This obviously results in the high defect concentration measured by RBS. The high radiation resistance may be explained by the high ionicity of the material combined with the high defect mobility within the thermal spike which may cause an effective defect annealing process similar as suggested for nuclear energy deposition [1].

References

[1] T. Steinbach, Th. Bierschenk, S. Milz, M.C. Ridgway, W. Wesch, J. Phys. D: Appl. Phys. **47**, 065301 (2014)

Work supported by Bundesministerium für Bildung und Forschung (BMBF, contract no. 05KJ10SJ1) and Deutscher Akademischer Austauschdienst (DAAD, ID 50753245).

Porous structure formation in ion irradiated germanium

Tobias Steinbach and Werner Wesch

Ion irradiation of amorphous germanium (a-Ge) leads to the formation of voids close to the sample surface and the transformation into a sponge like surface layer at high ion fluences ([1] and references therein). This extreme structural modification is accompanied by a strong volume expansion Δz which is illustrated in Fig. 1 for Ge irradiated with I and Au ions [1]. After amorphization of the irradiated crystalline Ge layer is completed in the ion fluence range of $N_I \sim 10^{13}$ cm^{-2}, the volume expansion starts for fluences approximately two orders of magnitude above the amorphization threshold, i.e. for ion fluences $N_I > 1\text{x}10^{15}$ cm^{-2}. For both ion species, Δz increases linearly with increasing ion fluence. The larger slope for Au irradiation is a consequence of the higher nuclear energy deposition caused by the Au ions. Whereas in case of Au irradiation a saturation Δz ~ 560 nm at $N_I = 2\text{x}10^{16}$ cm^{-2} without any further structural modification (not shown) is observed, for I irradiation a temporary saturation Δz ~ 770 nm at $N_I \approx$ 4.25-5.0x10^{16} cm^{-2} is reached. The identical ratio between the saturation value and the projected ion range of $\Delta z/R_p$ = 8.0-8.3 for both ion species suggests that in this fluence region the ion beam induced structural modifications caused by I and Au irradiation are identical. For higher ion fluences I irradiation causes an extreme volume expansion for $N_I > 5.25\text{x}10^{16}$ cm^{-2} with a maximum value of Δz = 1.63 μm at $N_I \sim 7\text{x}10^{16}$ cm^{-2} and a continuous decrease for still higher fluences.

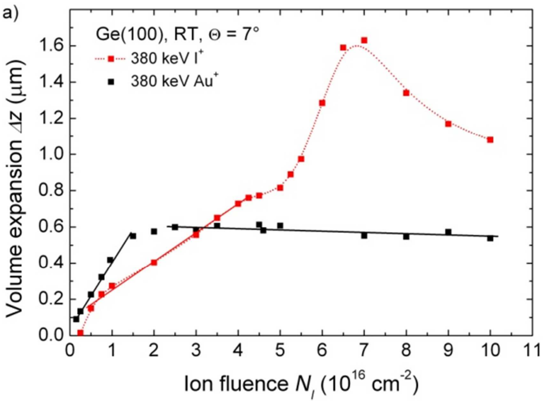

Fig. 1: *Volume expansion Δz as a function of the ion fluence N_I for Ge irradiated at room temperature with 380 keV I and Au ions [1].*

In the ion fluence region ~ 10^{15} cm^{-2} $\leq N_I \leq$ 4x10^{16} cm^{-2} irradiation with both ion species leads solely to the formation of sponge-like porous surface layers the thickness of which increases with the ion fluence (Fig. 2 for I irradiation).

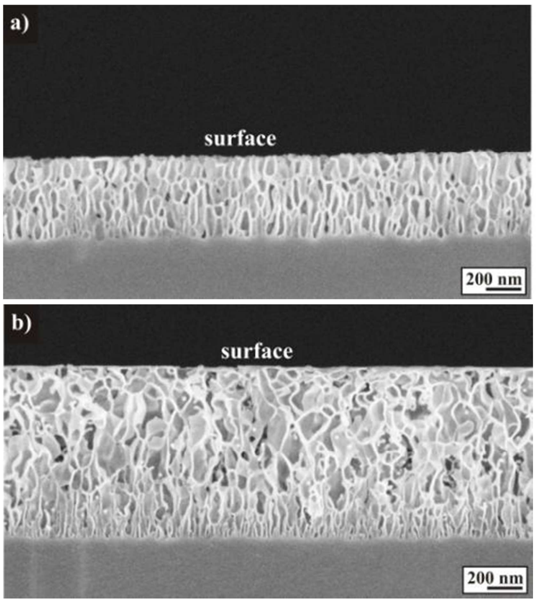

Fig. 2: *Cross-section SEM images of Ge irradiated with 380 keV I ions to fluences $N_I = 1\text{x}10^{16}$ cm^{-2} (a) and 4x10^{16}cm^{-2} (b) [1].*

The extreme volume expansion observed in case of I irradiation at high fluences (Fig. 1) is connected with the formation of a buried netlike porous structure as illustrated in Fig. 3 for an ion fluence of $N_I = 6x10^{16}$ cm^{-2}.

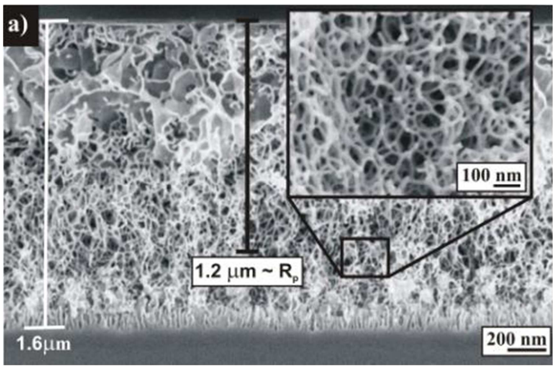

Fig. 3: Cross-section SEM image of Ge irradiated with 380 keV I ions to a fluence of $N_I = 6x10^{16}$ cm^{-2} [1].

It is obvious that this netlike porous structure consisting of 10-15 nm thin interconnected Ge nanowires starts in depth regions of the nuclear energy deposition maximum or the projected ion range R_p. In the fluence range where the volume expansion has its maximum (N_I ~ 7x10^{16} cm^{-2}) the netlike structure covers the whole surface layer. The continuous decrease of Δz at still higher ion fluences is attributed to local instabilities of the structure [1].

In agreement with earlier published results on low energy heavy ion irradiation of a-Ge (see references in [1]) also I and Au ion irradiation causes the formation of voids only in the amorphous Ge phase close to the surface, and with ongoing irradiation sponge-like porous surface layers are formed. The underlying mechanism is commonly attributed to the energetically favourable agglomeration of vacancy-like defects induced by the nuclear energy deposition. The influence of the nuclear energy deposition is clearly reflected in the differences in volume expansion for the different ion species (Fig. 1). However, at high ion fluences a second transformation into a netlike porous structure is only observed in I irradiated samples indicating that, similar as it was observed in case of irradiation with ion energies of several MeV [2], the implanted ion species and their chemical properties obviously play an important role. The I ions implanted into the sponge-like porous layer, i.e. into the Ge walls, act as interstitial defects leading to dangling Ge bonds within the Ge walls. These defects are effective sinks for radiation induced vacancies which agglomerate to small vacancy clusters in order to minimize the dangling bond concentration. The presence of dangling Ge-bonds is therefore assumed to cause instability and an energetically driven transformation to a netlike porous structure [2]. Contrary, in high-fluence Au irradiated Ge such a structural transformation is not observed, and it is proposed in Ref. [2] that the implanted ions diffuse into the Ge matrix where they occupy regular lattice sites and are bonded to the Ge atoms.

References

[1] T. Steinbach, W. Wesch, Nucl. Instr. and Methods B **319**, 112-116 (2014).

[2] T. Steinbach, J. Wernecke, P. Kluth, M.C. Ridgway, W.Wesch, Phys. Rev. B **84**, 104108 (2011).

Work supported by the Bundesministerium für Bildung und Forschung (BMBF, contract no. 05KJ10SJ1).

Ion beam induced thin film stress in lithium niobate

E. Schmidt, T. Steinbach, W. Wesch

Irradiation with energetic ions is well suitable for the selective modification of crystalline solids for many applications. One of several processes occurring during the irradiation is the formation of lattice defects, which accumulate with ongoing irradiation. In many materials this accumulation leads to a phase transformation from the crystalline to the amorphous state at high fluencies. In general amorphisation causes the formation of mechanical stress, which is disadvantageous for various applications of ion beam technologies. An example for the negative influence of such effects is the application of ion beam enhanced etching in $LiNbO_3$ as described previously [1]. $LiNbO_3$ is getting fully amorphous and generates highly anisotropic thin film stress under ion irradiation, which limits the application of this technique.

The aim of this work was to investigate the formation of ion beam induced thin film stress in $LiNbO_3$. For this purpose, irradiations with varying parameters (ion energy and irradiation temperature) over a wide range of ion fluencies for different crystallographic orientations were performed. Ion beam induced defect-formation could be studied in-situ by means of RBS in channeling configuration. The in-situ measurement of ion beam induced thin film stress was realized by a scanning laser reflection technique. A resulting dependence of damage- and stress-formation of $LiNbO_3$ under irradiation with 1 MeV I-ions is shown in Fig. 1.

The stress-formation was measured in-situ in three different crystallographic orientations, as shown in Fig. 1 (top). Due to the highly anisotropic crystal structure of $LiNbO_3$ the stress formations along the various axes differ in their main characteristics, i.e. the stress yield as well as the fluence dependence show a different behavior. Especially in Z-cut $LiNbO_3$ the stress values are one order of magnitude smaller compared to the other measured orientations. Moreover the stress-behavior in this orientation shows a superposition of two well separated stress-maxima during the irradiation.

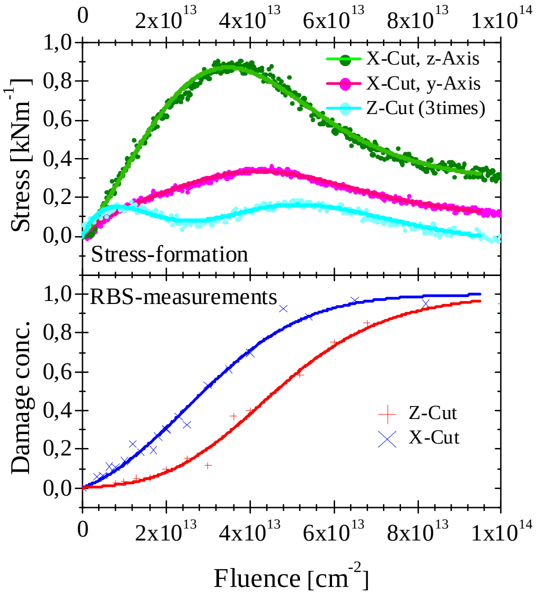

Fig. 1: *Ion beam induced stress and damage formation in $LiNbO_3$ at irradiation with 1MeV iodine*[6].

The measurement of ion beam induced damage by RBS in different crystallographic orientations is shown in Fig. 1 (bottom). The differences in X-cut and Z-cut $LiNbO_3$ are well known and attributed to the different crystallographic visibility of point defects in $LiNbO_3$ [2]. The defect formation shows a slight increase up to a fluence of ~$1x10^{14}$ cm^{-2}, where amorphisation is reached. At this point no significant crystalline structure can be measured with RBS in the irradiated material in any axis.

The comparison of ion beam induced thin film stress and crystallographic damage reveals a similar behaviour as previously observed in germanium [3]. In this case the physical description of ion beam induced thin film stress is based on defect induced local strain and viscoelastic relaxation [4]. However, this approach cannot explain the strong anisotropic stress dependence in $LiNbO_3$ and especially the two well separated maxima observed in the stress formation of Z-cut $LiNbO_3$.

Thus a new approach was developed for $LiNbO_3$ based on the assumption, that different defect types strain the surrounding crystalline $LiNbO_3$ in an anisotropic manner. The formation of anisotropic thin film stress during the irradiation is now attributed to the formation and transformation of different point and extended defects from crystalline material into each other and finally to the amorphous phase. Different defect-formation models were adapted to the experimental data. The most suitable approach in the description of all experiments was made with a modified damage formation model as proposed by Webb and Carter [5] with three different defect types beside the amorphised and crystalline state. Therein the defect formation and transformation were mathematically described by a complex set of coupled ordinary differential equations (for details see [6]).

With ongoing irradiation different defect types (n_1, n_2 and n_3) were generated from crystalline material (n_u). At higher fluencies amorphous material (n_A) is generated and the defect formation saturates. The measured total stress as well as the measured damage-formation is now understood as the superposition of different formations and transformation of defects.

Best fits based on calculation with this model are shown in Fig. 1 (solid lines). The calculated fluence dependence of the formation and transformation of different defect types as well as the crystalline and amorphous phase are shown in Fig. 2.

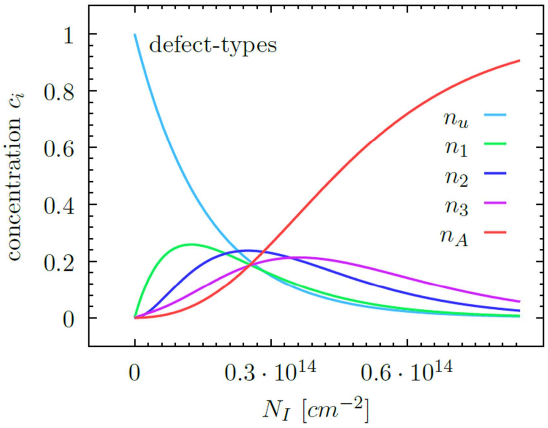

Fig. 2: *Concentrations c_i of different defect types over the ion fluence N_I for room temperature irradiations of $LiNbO_3$ with 1MeV I-ions calculated from the best fit to all stress- and RBS-data*[6].

References

[1] F. Schrempel *et al*., Opt. Lett. **34**, 1426 (2009).

[2] G. Götz *et al*., Nucl. Instr. and Meth. B **209-210**, 1079 (1983).

[3] T. Steinbach *et al*., Nucl. Instr. and Meth. B **307**, 194-198 (2009).

[4] E. Snoeks *et al*., Appl. Phys. Lett. **65**, 2487 (1994).

[5] R. Webb and G. Carter, Radiat. Eff. Defect. **42**, 159 (1979).

[6] E. Schmidt *et al*., submitted to Nucl. Instr. and Meth. B (2013).

Improvement of I_cR_n-product and microwave response of planar $Ba(Fe_{1-x}Co_x)_2As_2$/Pb Junctions with artificial barrier layers

Sebastian Döring, Stefan Schmidt, Manuel Monecke, Martin Feltz, Frank Schmidl, Volker Tympel, Kazumasa Iida[1], Fritz Kurth[1], Bernhard Holzapfel[1], and Paul Seidel

[1] Institute for Metallic Materials, IFW Dresden, Helmholtzstraße 20, D-01069 Dresden

In our investigations on iron-based superconductors we designed and applied layouts for heterojunctions [1-4]. They consist of a $Ba(Fe_{1-x}Co_x)_2As_2$ (Ba-122) base electrode, a Pb counter electrode (covered by In) and an artificial barrier layer. In early experiments we used sputtered gold layers as barrier and observed Josephson effects for junctions with thin layers ($d = 5$ nm) [1-3], while thicker layers ($d = 10$ nm) lead to transport dominated by Andreev reflection and possible other effects corresponding to the special type of order parameter symmetry in pnictide superconductors [3,4]. Based on these results we further developed our preparation processes and tested titanium oxide layers as barrier. Via Ion Beam Etching the existing gold film thickness was reduced to nominally 1 nm and titanium layers with $1.0\,\text{nm} \leq d \leq 7.0\,\text{nm}$ were sputtered *in-situ* and subsequently oxidized on atmosphere at 80°C [5]. Junctions prepared in such manner showed Josephson effects for $d \leq 2.0$ nm [6]. Here we compare planar Josephson junctions with Au and TiO_x barrier layers and show the resulting improvement of properties regarding the I_cR_n-product as well as their microwave response.

Fig. 2a) shows a typical *I-V*-characteristic of a junction with a gold barrier. One can see an asymmetric shape, thus the positive critical current is higher than the negative one. For the positive critical current a value of $I_c = 350\,\mu A$ and a normal resistance of $R_n = 53\,m\Omega$ can be observed resulting in an I_cR_n-product of about 18 µV. This is too low for possible application like SQUIDs, where the transfer function and the noise are proportional to I_cR_n.

Additionally the stability of junctions with gold barrier was not very good, due to current noise the values of critical current and normal resistance were fluctuating even at constant temperature. Because of these disadvantages an improvement of the gold barriers or another barrier material has to be introduced.

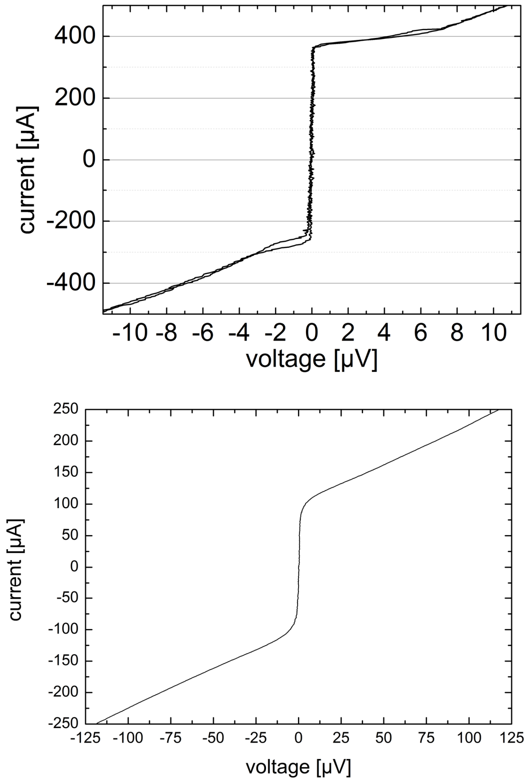

Fig. 2: *I-V-characteristics of a junction at 4.2 K. a) 5 nm Au barrier, area 30×30 µm^2 [1]. b) 2.0 nm TiO_x barrier, area 7×7 µm^2.*

In fig. 2b) an *I-V*-characteristic of a junction with titanium oxide layer is shown. The specific parameters are $I_c = 115\ \mu A$ and $R_n = 0.75\ \Omega$, resulting in $I_cR_n = 90\ \mu V$, which is an increase by factor 5 compared to the former Au barrier junctions. Additionally, only very little current noise was observed and let assume a good stability of junctions with TiO_x barrier.

Further characterization of a Josephson junction is typically performed by irradiation with microwaves of frequency *f*. By doing so, Shapiro-steps are expected at constant voltages $V_n = h/2e \cdot nf$. The dependence of the *n*-th step can be obtained from the generalized Josephson equation:

$$\beta_C\ddot{\varphi} + \dot{\varphi} + \sin\varphi = i_b + i_m \sin\Omega\tau \quad (1)$$

With the McCumber parameter β_C, i_b and i_m, the normalized bias and microwave currents, Ω the relative microwave frequency and τ the normalized time.

The experimentally examined microwave dependence for the gold barrier junction is shown in fig. 3a). A simulation of the critical current was possible but just with the additional assumption of an excess current of unknown origin with exponential dependence and an offset of about 30 µA. Even with this assumption the periodicity of the critical current is rather bad due to the current noise mentioned above. The first Shapiro step could be observed for one period but then vanished for higher microwave amplitudes. Again by comparing the microwave dependence of gold barrier junctions to them with titanium oxide barriers as shown in fig. 3b) one can see clearly improvement in the behavior. The periodicity of the critical current and the first Shapiro step is very good up to amplitudes of about 5. Also the fitting of measured values with the simulation from equation (2) is much better compared to fig. 3a). Only a few losses in the first Shapiro step are observed thus they do not reach the expected maximal values from the simulation.

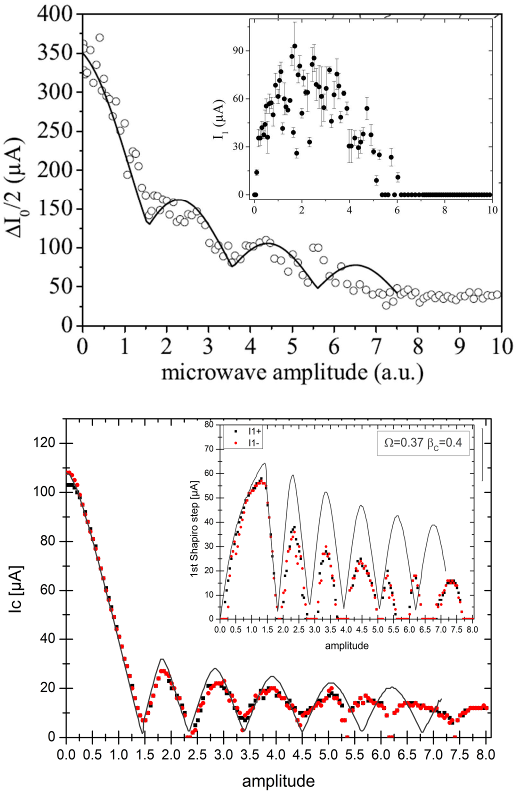

Fig. 3: *Josephson current and first Shapiro-step (Inset) vs. microwave amplitude.*
a) 5 nm Au barrier, area 30×30 µm² [1,2].
b) 2.0 nm TiO_x barrier, area 7×7 µm².

In summary we could successfully expand our possibilities of junction preparation and could improve the properties of our planar Josephson junction significantly by using titanium oxide as barrier material.

We thank the EC (project IRON-SEA), the Landesgraduiertenförderung Thüringen and the DFG (SPP 1458) for financial support.

References

[1] S. Schmidt *et al.*, Appl. Phys. Lett. **97**, 172504 (2010).
[2] S. Schmidt, Diploma Thesis, FSU Jena (2011).
[3] S. Schmidt *et al.*, Phys. Proc. **36**, 82-87 (2012).
[4] S. Döring *et al.*, Physica C **478**, 15-18 (2012).
[5] M. Monecke, Diploma Thesis, FSU Jena (2013).
[6] S. Döring *et al.*, arXiv.org 1309.2331 (2013).

The interaction of intrinsic Josephson junctions with resonant modes of the transmission line

Alexander Grib[1] *and Paul Seidel*

[1]*Physics Department, Kharkiv V. N. Karazin National University, 61022, Kharkiv, Ukraine*

It was experimentally shown that intrinsic Josephson junctions radiate coherently if voltages over junctions equal to values corresponding to geometrical resonances in the system [1]. Self-induced resonant steps appeared in the IV-characteristics of the system, and coherent radiation of junctions was registered just on these steps. Numerical modeling of this effect [2,3] showed that both the appearance of self-induced steps and coherent radiation on them are possible if the system consists of the set of small junctions which radiate inside the system. In the present paper we show that our model explains some features of the experimental results of Ref. 1.

In the 'lumped' representation the transmission line consists of two parallel to each other current lines connected by capacitances *C* which divide the system to *N* equal cells. In each of these connection lines we added to the capacitance also *n* Josephson junctions. We obtained the lumped model of *N* 'small' intrinsic junctions in each of *n* layers of intrinsic junctions inside the transmission line. Parameters of the cell (the resistance *R*, the inductance *L* and the capacitance *C*) depend on the linear dimension of the elementary cell ζ, so the transmission line of *N* cells has the length $N\zeta$. The velocity of the propagation of waves in a transmission line is equal to $c' = c_0 n'^{-1} = \zeta (LC)^{-1/2}$, where c_0 is the velocity of light in vacuum, $n' \approx 4.47$ is the refraction index.

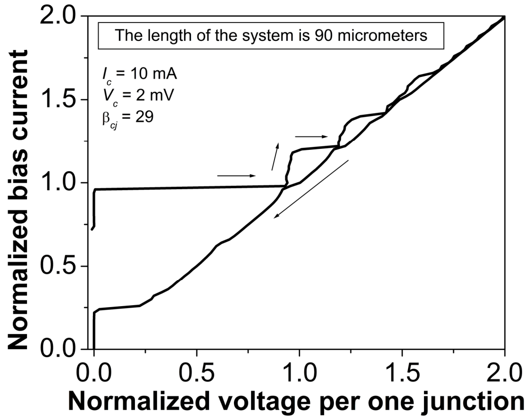

Fig. 1: *The IV-characteristic of the whole system. Bias current is normalized with respect to the averaged critical current 10 mA, voltage over the system is divided on the total amount of junctions and normalized with respect to the averaged critical voltage 2 mV. Arrows show the direction of the change of the critical current.*

To find IV-characteristics of junctions, one must solve dynamic equations for phase differences across junctions together with differential equations for currents in the transmission line [2,3]. To obtain standing waves in the system, one must solve all these equations with boundary conditions which correspond to open ends of the line.

With the use of the described model, we calculated the IV-characteristics of the mesa structure of 90 micrometers length (*N* = 6, $\zeta = 15 \mu m$) and a height of 1 micrometer (665 layers of junctions, the total value of junctions in the system is 4655). Critical currents of junctions I_C were random values which had the Gaussian distribution with the spread 0.4 mA. The IV-characteristic of the system has self-induced steps (Fig. 1).

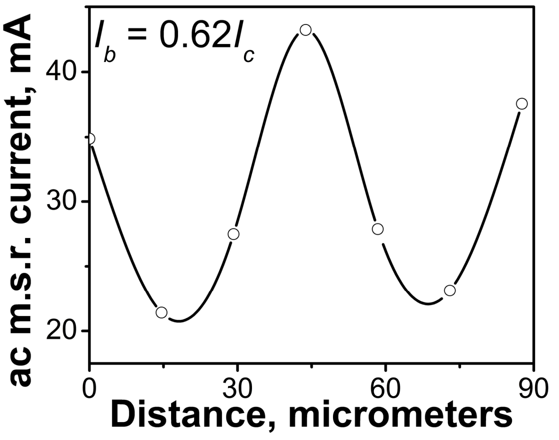

Fig. 2: *The distribution of the mean square root ac current (the standing wave) along the transmission line at* $I_b = 0.62 \cdot I_c$*.*

These steps are formed due to the appearance of a standing wave formed at the resonance in the transmission line. The ac synchronizing current increases in some spatial places of the transmission line at the resonance (see Fig. 2). Junctions radiate intensively in these places, catch their own radiation by means of the feedback circuit (the transmission line) and lock themselves to their own radiation. Therefore, the resonant step is formed in the IV-characteristic. Maxima of emitted power appear at self-induced steps because of the locking effect of the synchronizing ac current. The dependence of the averaged square of the sum of all ac voltages over junctions *S* on the averaged voltage over junctions is shown in Fig. 3. This value is proportional to ac power emitted by the whole system [2]. Maxima of this dependence coincide with the resonant voltages at which self-induced steps in Fig. 1 appear. We calculated the frequency ν_{max1} at which the first maximum of *S* appears (or the interval of frequencies between maxima of *S*) on the reciprocal length of the system (Fig.4). The obtained dependence is close to the dependence which was found in the experiment [1]. Thus, we showed that our model can give the quantitative description of the experiment.

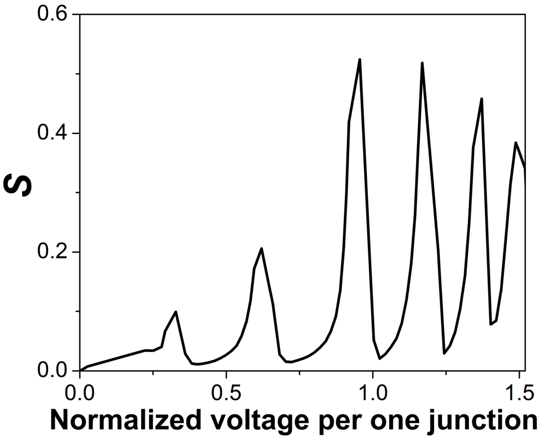

Fig. 3: *The dependence of the averaged square of the sum of all ac voltages over junctions S on the averaged voltage per junction.*

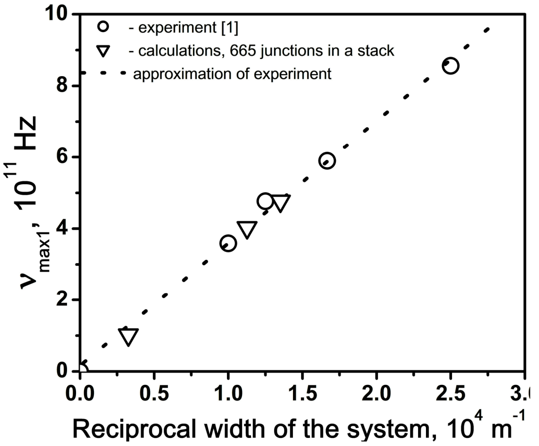

Fig. 4: *Experimental data* [1] *of frequencies at which maxima of coherent radiation was registered (circles) and the calculated dependence of the frequency of the first maximum of S on the reciprocal length of the transmission line: (triangles). Dashed line is the approximation of experimental results.*

References

[1] L. Ozyuzer *et al*., *Science* **318**, 1291 (2007).

[2] A. Grib and P. Seidel, Low Temp. Phys. (Fiz. Nizk. Temp.) **38**, 321-325 (2012).

[3] A. Grib and P. Seidel, 11-th European Conference on Applied Superconductivity (EUCAS 2013), September 15-19, 2013, Genova, Italy, 1P-EL3-06, accepted for J. Phys. Conf. Series (IOP).

Planar hybrid tunnelling, Josephson junctions based on Ba-122 single crystals

*Noor Hasan, David Reifert, Sebastian Döring, Stefan Schmidt, Frank Schmidl, Volker Tympel, Paul Seidel, Thomas Wolf **

** Karlsruhe Institute of Technology, Institute of Solid State Physics, 76021 Karlsruhe, Germany*

In order to understand the nature of the superconductivity in iron pnictides it is necessary to examine their electrical properties and fundamental properties can be derived, such as energy gap and order parameter symmetry. Thus we started to fabricate planar hybrid junctions on Ba-122 ($BaFe_2As_2$) single crystals, since single crystals are superior to thin films in various aspects (e.g. purity, better crystalline structure, easier to dope etc.)

We began with undoped single crystal to prepare the junctions; single crystals of undoped Ba-122 were produced by the Karlsruhe Institute of Technology with a self-flux method. Further details of this technique can be found in [1,2]. They usually have a very rough surface structure which makes it necessary to do a polishing method for these materials, see Fig.1.

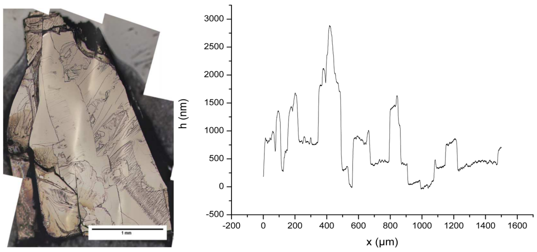

Fig. 1*: On the left side the surface of an unused crystal can be seen. The right diagram shows the surface profile of the crystal. It was measured with a DekTak profilometer [8].*

Therefore we have to solve several issues, especially achieving a high surface quality with an RMS roughness less than 5nm. A high surface quality is necessary since we were planning to realize the junctions via photolithography similar to the processing of the Ba-122 thin films (like in our previous works [3-7]). We were polishing the surface of the single crystal to get an RMS roughness of approx. 2nm or less. Further details of the polishing procedure can be found in [8]. Fig.2 illustrates the RMS surface of single crystal which should be good enough for our junctions. To cover the whole sample a gold layer or Titanium dioxide via layer with a thickness of 10nm as barrier material was sputtered on top. The gold covered iron pnictide base electrode was pattered via argon ion beam etching (IBE) (500eV beam voltage, 0.9 mA cm^{-2} ion beam density) we used before etching for preparation of a photoresist mask that has a thickness 2.5µm.

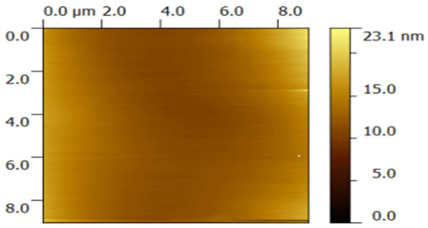

Fig. 2*: Atomic force microscope measurement of a polished surface, RMS=1.96nm.*

By depositing Ti and Au we create pads for the counter electrode which produced in the same time in our Ti and Au system of vacuum chamber, before that we were using a photoresist with a thickness of 1.4 um to create a mask. Fig.3 contains a sample with all process; images were taken by a microscope to get more clarification for surface of single crystal. The counter electrode was produced of a double layer in another lift off process via thermal evaporation of Pb layer which has a thickness of 300 nm and In layer which has a thickness of 50nm. We used an In layer as protecting layer, because Pb oxidizes with atmosphere if it is left for a long time. This is shown in Fig.5 in the last image. Prior to the Ti/Au pads deposition we sputtered SiO_2 (50W rf-power, thickness of 200nm) to insulate the base electrode from counter electrode.

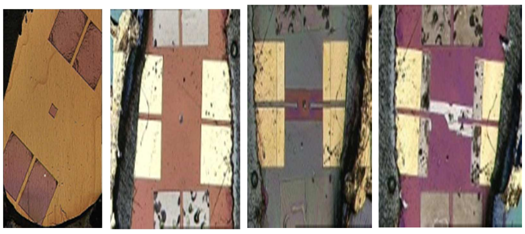

***Fig. 3**: from left to right the first image of single crystal surface and base electrode, the second image with SiO_2 deposition and pads of Ti/Au for counter electrode, third image is mask for Pb counter electrode, and the last one is finished sample*

In Fig.5 illustrates that we also have fabricated a planar junction of lead thin film with a thickness 300 nm as a base electrode evaporated by thermal evaporation system in a vacuum chamber .it is important to know the surface quality of Pb-thin film. Therefore we firstly tested the surface roughness of Pb-thin film; we found that RMS is approx. 0.9 nm, Fig .4. The image was taken by atomic force microscopy (AFM).

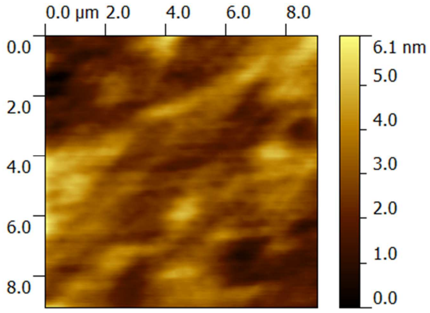

***Fig. 4**: Atomic force microscope measurement of Pb-thin film surface RMS=0.921nm.*

The rest of technique fabrication is the similar on Ba-122 single crystal.

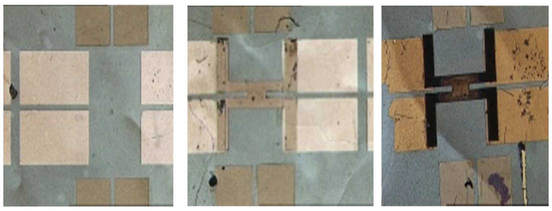

***Fig. 5**: planar junction on Pb thin film as a base electrode, the last image shows the Pb as counter electrode has oxidized when is left for a long time.*

We have fabricated a design of a tunnel structure for single crystals and lead thin film that utilizes our available thin film technologies. The final structure of our junction design that will allow us the determination of T_c and I_c of both base and counter electrode. Therefore we will start with superconductors co-doped Ba-122 single crystals.

Acknowledgements

This work was partially supported by DFG within SPP 1458 under project no.SE 664/15-2 and the EU in the project IRON-SEA, and German Academic Exchange Service DAAD.

References

[1] F. Hardy *et al.*, Phys. Rev. B **81**, 060501 (2010).
[2] F.Hardy *et al.*, Europhys. Lett. **91**, 4400 (2010).
[3] S.Döring *et al.*, physica C Supercond **478**, 15-18 (2012).
[4] S.Schmidt *et al.*, Appl.Phys.Lett.**97**, 172504 (2010).
[5] S.Dring *et al.*, Supercond. Sci.Technol.**25**, 084020 (2011).
[6] S.Döring *et al.*, Phys.Proc.**27**,296-299(2012).
[7] S.Schmidt *et al.*, Phys.Proc.**36**,82-87(2012).
[8] D.Reifert, Master thesis, “Kontaktentwicklung auf Pniktid-Einkristallen” FSU Jena, (2013).

Mechanical loss of thin silicon beams in thermal non-equilibrium

R. Glaser, C. Schwarz, D. Heinert, G. Hofmann, R. Nawrodt

One great goal of modern day physics is the direct detection and measurement of gravitational waves opening a new observation window to the universe. Novel designs for third generation interferometric gravitational wave detectors, like the Einstein Telescope, are using optics at cryogenic temperatures e.g. of 10 K lowering thermal noise in the detection band [1].

In order to achive the desired sensitivity the optical components need to be suspended as pendula and high laser powers (up to the MW range) have to be used. Even in high reflectivity mirrors a small amount of light gets absorbed and thus heats the optical components. This heat needs to be carried away which is done by highly conductive suspension elements made from sapphire, silicon or metals. In order to extract heat through the suspension elements a temperature gradient is needed – otherwise no heat gets removed. This temperature gradient causes a thermal non-equilibrium state in these suspension elements. So far, the mechanical loss of these elements – which is directly linked to the thermal noise by means of the fluctuation dissipation theorem [2] – has just been investigated under thermal equilibrium. In this work the mechanical loss of a thin silicon beam under thermal non-equilibrium is studied.

A thin silicon beam is clamped on both sides with copper clamps, allowing the change the temperature on both ends (see Fig. 1). During cooling, different coefficients of thermal expansion in the sample and the support would result in a variable stress inside the flexure if both ends are fixed to a support. To overcome this issue the lower clamp was not connected to the supporting structure but was suspended by the silicon flexure itself. This allows gravity to establish a constant stress along the fibre which is independent from the measurement temperature. Both clamps are equipped with heaters and temperature sensors.

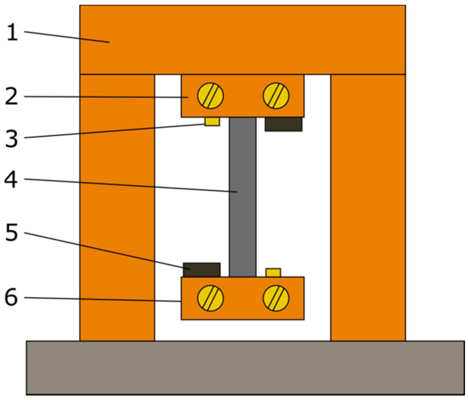

Fig. 1: *Schematic view of the setup used to investigate the mechanical loss under thermal non-equilibrium.1 - support structure, 2 - upper clamp, 3 - upper temperature sensor, 4 - cantilever, 5 - heater, 6 – lower clamp.*

The setup is mounted in a cryostat (temperature range 5 K to 320 K) and the vibration of the flexure is measured by means of a laser vibrometer. The excitation is done by means of an electrostatic driving plate.

Above 50-70 K thermoelastic loss is known to be the dominant loss mechanisms for structures used in this experiment [3]. In the equilibrium case the internal friction caused by thermoelastic damping can be calculated using the equation derived from Zener [4]

$$\Phi_{TED}(\omega) = \frac{YT_0\alpha^2}{\rho C_p}\frac{\omega\tau}{1+(\omega\tau)^2}. \qquad (1)$$

Here Y is the Young's modulus, α is the thermal expansion coefficient of the beam at a temperature T_0. ρ is the mass density and C_p the specific heat capacity. ω is the angular frequency of vibration of the beam and τ is a parameter depending on the dimensions of the beam and can be calculated for a rectangular cross section as follows

$$\tau = \frac{h^2}{\pi^2}\frac{\rho C_p}{\kappa}. \qquad (2)$$

This equation is used for a beam with a thickness of h and a heat conductivity κ.

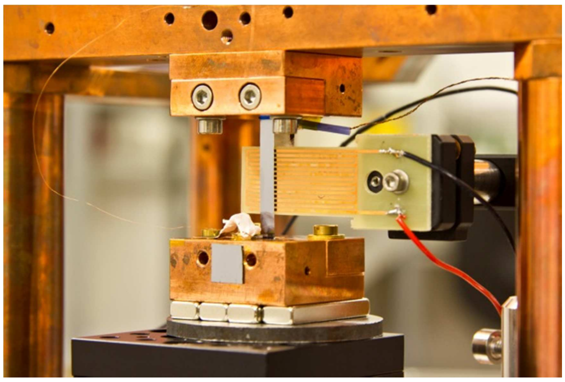

Fig. 2: Photograph of the clamping structure for non-equilibrium loss measurements.

Especially the temperature range around 100 K to 140 K is of importance as the coefficient of thermal expansion of silicon vanishes at 122 K. Due to the vanishing coefficient of thermal expansion the thermoelastic loss shows a local minimum around this temperature. Previously measured cantilevers confirm that in thermal equilibrium the measured values follow nicely the predictions of thermoelastics [3]. In the case of non-equilibrium measurements the mechanical loss follows a trend that can be interpreted as a superposition equilibrium values. As the temperature changes along the flexure due to a thermal gradient the total loss comprises of the sum of losses of inifite small slices along the flexure. Figure 3 shows the measured loss of a dry etched silicon beam with a thickness of 155 µm for an increasing temperature difference. In order to generate a temperature difference ΔT along the cantilever the temperatures of the clamps have been changed in opposite directions while keeping the average temperature constant. It can be seen that the loss increases with an increasing ΔT.

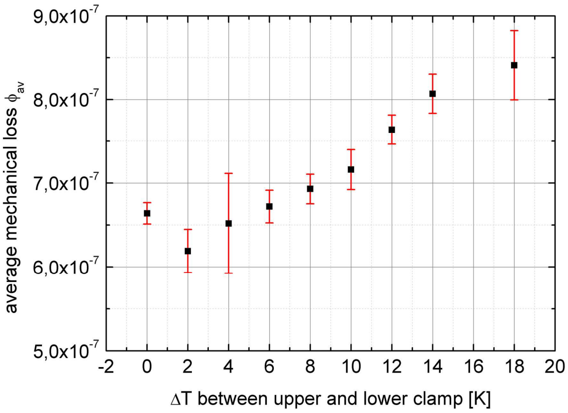

***Fig. 3:** Investigation of the mechanical loss in thermal non-equilibrium. The average temperature was kept constant while the clamp temperatures were changed in opposite directions.*

This first measurement demonstrates the capabilities of the experiment. Further measurements are needed – especially at low temperatures in the range from 10 to 20 K in order to understand if there is any effect on the mechanical loss that arises from the non-equilibrium state or not.

This work was supported by the DFG under contract SFB TR7.

References

[1] S. Hild *et al.*, *Class. Quantum Grav.* **28**, 094013 (2011).

[2] H.B. Callen and T. A. Welton, *Phys. Rev.* **83**, 34-40 (1951).

[3] R. Nawrodt et al., *Class. Quantum Grav.* **30**, 115008 (2013).

[4] C. Zener , *Proc. Phys. Soc. London, 52*, 152-166 (1940).

Mechanical loss of p- and n-type silicon at low temperatures

Gerd Hofmann, Julius Komma, Christian Schwarz, Daniel Heinert, Ronny Nawrodt

Future gravitational wave detectors like the Japanese KAGRA [1] or the European Einstein Telescope [2] will utilise cooling of the test masses to reduce their thermal noise contribution in the detector's signal. Specifically Brownian thermal noise is directly linked to the test mass temperature and its mechanical loss ϕ [3].

Despite of the outstanding performance of fused silica at room temperature it cannot be used at low temperature as thermal noise outreaches due to the high mechanical loss of the material [4]. In contrast crystal materials like sapphire or silicon show a low mechanical loss at low temperatures and thus are on the schedule for future detectors.

Another benefit will be the high thermal conductivity of these materials which helps to reduce thermal lensing from a temperature gradient in the test masses build up by absorbed laser light. Sapphire is an insulator and exhibits moderate absorption in the IR. In contrast the optical absorption in silicon is strongly dependent on free carriers and thus on the doping of the material [5].

The influence of the doping on the mechanical loss is so far unknown and is subject of current investigations. Mechanical loss spectroscopy of Czochralski grown p-type and n-type silicon with different densities of boron and phosphorous is carried out. The samples are excited to resonant vibrations and the free ring down τ of the amplitude at the resonant frequency f is monitored. The mechanical loss is given by $\phi = 1/(\pi f \tau)$. All samples were cylinders of 100 mm diameter and 100 mm height. We used a single loop tungsten wire of 75 µm diameter to suspend the samples inside a specially build cryostat [6]. The vibrational resonances were excited by an electrostatic driving plate near one end of the cylinders. Fig. 1 shows the amplitude along the axis of the cylinder for the eigenmode at 35 kHz. This mode was measured at three silicon samples, two of them doped with 1.5×10^{16}cm^{-3} respectively 2.1×10^{14}cm^{-3} phosphorous (Si:P, n-type) and one by 5×10^{15}cm^{-3} boron (Si:B, p-type).

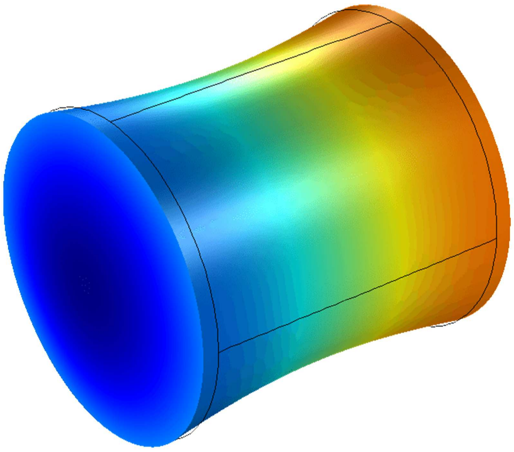

Fig. 1: *Illustration of the deformation along the cylindrical axis of the vibration at 35 kHz of the silicon cylinders under investigation. For comparison the same eigenmodes of the samples were selected for all measurements.*

Our measurements reveal a nearly identical behaviour in terms of mechanical loss from 300 K down to 40 K for all three samples (see fig. 2). Starting at room temperature at a value of $\phi = 7\times10^{-9}$ the loss rises up to 1×10^{-8} at 200 K and then decreases towards 6×10^{-9} at 40 K. For lower temperatures both n-type samples show increasing loss again. In contrast the loss of the p-type sample drops down to a value of 1.6×10^{-9} at 9 K representing the lowest loss for this series of measurements.

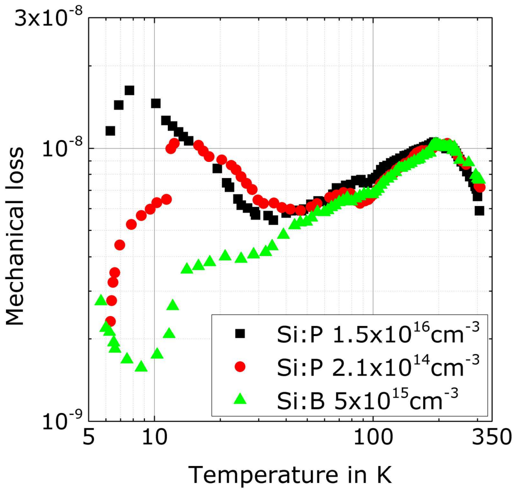

Fig. 2: *Measured mechanical loss of three silicon samples doped with phosphorous (Si:P) and boron (Si:B). While for temperatures down to 40 K no deviation is observable at even lower temperatures the measured data differs obviously.*

A material's total mechanical loss typically is the sum of different mechanisms which contribute together. One intrinsic mechanism is given by the thermo-elastic loss [7]. The mechanical vibration of the solid causes areas to be stretched while others are compressed. This results in a local change of temperature between these areas and subsequently leads to a dissipating flow of heat. A numerical calculation reveals this loss to be more than two orders of magnitude lower than the measured one and thus not to be significant in our case.

Other fundamental mechanisms consider a coupling of acoustic phonons caused by the resonant vibrations with other thermal phonons of the solid's lattice (phonon-phonon) or the free electrons (phonon-electron) [8] in case of a metal or likewise in our case of a semiconductor. The amount of free electrons is strongly affected by doping as well as by temperature. Whereas the amount of free electrons is increased with higher concentrations of phosphorous it is reduced by doping with boron. Our experiment shows higher losses at low temperatures for samples with a high free carrier concentration. Especially at temperatures below 40 K this concentration of free electrons changes strongly likewise the observed mechanical loss begins to differ drastically in this temperature regime. Thus a possible indication of a relation between the mechanical loss and the change in the free electron concentration is given.

Further experiments of an even heavier doped p-type silicon sample (2.3×10^{17}cm^{-3} boron) will be performed to extend our study. Also the electronic conductivity at low temperatures is of interest to check our experiment with the theory of mechanical loss by phonon-electron interaction.

This work was supported by the DFG under the SFB TR7 grant.

References

[1] K. Somiya, *Classical Quantum Gravity* **29**, 124007 (2012).

[2] Einstein gravitational wave Telescope conceptual design study, https://tds.ego-gw.it/ql/?c=7954 (2011).

[3] P. R. Saulson, *Phys.Rev. D.* **42**, 2437-2445 (1990).

[4] C. Schwarz *et al.*, *Proceedings of ICEC 22-ICMC 2008*, 519-524 (2009).

[5] J. Komma *et al.*, *Annual Report 2013 Friedrich-Schiller Universität Jena* (2014).

[6] R. Nawrodt *et al.*, *Cryogenics* **46**, 718-723 (2006).

[7] C. Zener, *Phys. Rev.* **52**, 230-235 (1937).

[8] V. B. Braginsky *et al.*, Systems with Small Dissipation (1985).

Optical absorption of silicon at 1550 nm at cryogenic temperatures

Julius Komma, Gerd Hofmann, Jerome Degaillaix[1], Christian Schwarz, Daniel Heinert and Ronny Nawrodt

[1]Laboratoire des Matériaux Avancés, IN2P3/CNRS, Université de Lyon, 7 Avenue Pierre de Coubertin, Villeurbanne 69100, France

Silicon is a promising material for a large scale cryogenic interferometric gravitational wave detector as shown in the Einstein Telescope (ET) design study [1]. In order to enhance the thermal noise performance future detectors like ET and the Japanese project KAGRA will use cryogenic optics. Due to a low intrinsic mechanical loss crystalline materials are preferred to amorphous materials [2]. KAGRA which is now under construction will be built with sapphire mirrors. However, silicon is available in much larger pieces because of its use in the semiconductor industry and was thus selected as a test mass material for ET.

For the design of the mirror suspensions, which are also responsible for the extraction of heat caused by optical absorption in the mirrors, the knowledge of the optical absorption at low temperatures is needed. The desired wavelength of such a detector is 1550 nm due to its possible low optical absorption in silicon [3].

An optical absorption measurement where the incoming and transmitted laser power is measured does not work for small absorption values. The difference between these two powers is too small to measure with high enough accuracy.

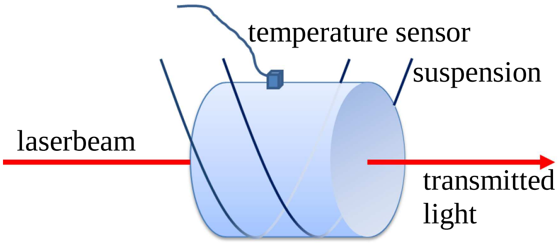

Fig. 1: *Schematic view of the calorimetric absorption measurement. The sample is orientated in the Brewster angle to avoid surface reflections.*

Therefore, we built a calorimetric setup to measure the optical absorption of silicon at cryogenic temperatures. Fig. 1 shows the setup for such a measurement. It is a direct measurement: a temperature sensor attached to the sample measures the heat generated by the optical absorption. The advantage of this type of measurement is that no calibration is needed. The optical absorption α can be calculated with the mass m of the sample and the knowledge of the heat capacity C following:

$$\alpha = \frac{\mathrm{m\,C}}{\mathrm{L\,P\,t\,\Delta T}},$$

L is the length of the sample, P the laser power, t the heating time and ΔT the increase in temperature. The laser source was a 5 W cw fiber laser from NKT Photonics. A mechanical shutter is used to define the illumination time of the sample.

Fig 2 shows acquired temperature data over time for a silicon sample at room temperature. The shown data gives a absorption of 3000 ppm/cm. The group at

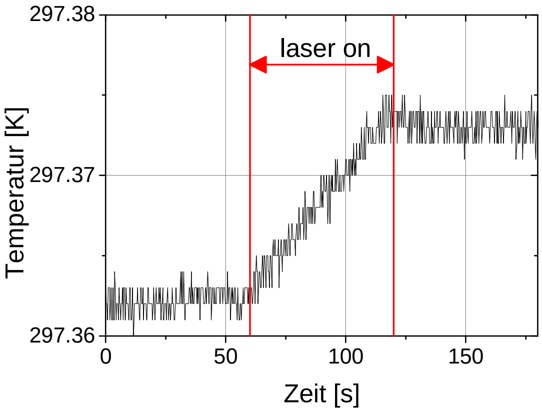

Fig. 2: *Typical heating curve.*

LMA measured 2900 ppm/cm [3] at the same sample with a deflection method.

In order to test the setup we started with samples with doping which causes a much higher absorption than intrinsic material. The dominating process for the optical absorption in the infra-red is suggested to be free carrier (fc) absorption in the conduction band. This process shows a strong dependence on the carrier concentration as shown in the following equation [4]:

$$\alpha_{fc} = \frac{Ne^2}{m^*\varepsilon_0 nc\tau}\frac{1}{\omega^2}$$

N is the number density of carriers, m^* the effective mass, n the refractive index, c the speed of light, τ the scattering time and ω the angular frequency of the incoming light. Results for different doped samples are shown in Fig. 3 where the linear behavior of carrier concentration and optical absorption can be seen.

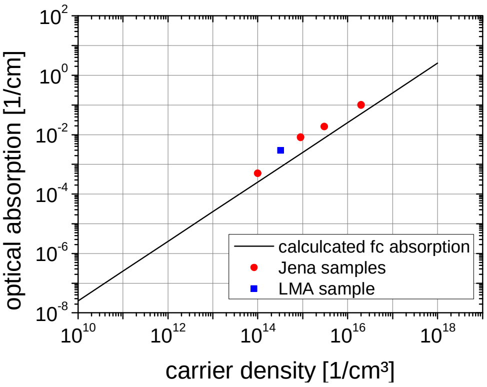

Fig. 3: *Optical absorption as a function of carrier concentration for different silicon samples.*

As the free carrier density is a strongly temperature dependent parameter calorimetric absorption measurements have been performed in an optical bath cryostat in a wide temperature range from 5 K to 300 K. A strong decrease in optical absorption was expected.

At low temperatures the calorimetric measurement benefits from a vanishing heat capacity for lower temperatures. As a consequence, it is possible to measure 20000 times smaller absorption values at 5 K than at 300 K for a given laser power.

Finally first results for a 100 Ωcm sample are shown in Fig. 4. The absorption decreases from 300 K down to 60 K by a factor of 2.3, below that the absorption stays at a constant level. This contradicts with the expectation that the free carrier absorption is strongly reduced at low temperatures. Thus, the generally made assumption that optical absorption decreases at low temperature due to the freeze-out of carriers cannot be underlined experimentally.

The results presented in this article strongly influence the selection of the optimum working temperature of a future GW detector based on silicon.

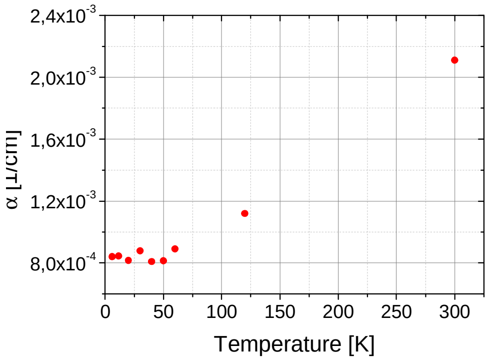

Fig. 4: *Temperature dependent optical absorption of a sample with 100 Ωcm.*

This work was supported by the DFG under contract SFB Transregio 7.

References

[1] https://tds.ego-gw.it/ql/?c=7954

[2] C. Schwarz *et al.*, SSP **184**, 443 (2012)

[3] J. Degallaix *et al.*, Optics Letters **38**, 2047-2049 (2013)

[4] P. Yu and M. Cardona, Fundamentals of Semiconductors, Springer, 4th edition (2010)

Precise measurement of reflectivity in an optical cavity

Felix Küster, Christian Schwarz, Ronny Nawrodt

Optical Resonators are responsible for great improvements in accuracy of measurements. They are used, for example, to stabilize laser frequencies so that they can even provide a more stable frequency than a caesium atom clock [1]. The properties of these cavities are essentially given by the mirrors, their spacing, shape and reflectivity. Hence it is possible to obtain the mirror reflectance out of the light signal transmitted through the cavity with high accuracy. This is very important to calculate dissipations in optical setups and especially crucial in low temperature measurements, e.g. interferometric gravitational wave detectors, where any dissipation leads to additional thermal noise [2].

Once the mirror setup for the resonator is decided, the required shape of the laser beam for resonance inside the cavity is given. In this case a confocal cavity with *d*=50 mm spacing is used, which means that both mirrors' radii of curvature are 50 mm as well. The task is then to match the incoming beam to this given shape as good as possible. To calculate the beam propagation through given optical elements, the Gaussian q-parameter [3] is a helpful tool:

$$\frac{1}{q(z)} = \frac{1}{R(z)} + i\frac{\lambda}{\pi w(z)^2},$$

where z is the propagation direction, $R(z)$ the radius of curvature of the wavefronts, λ the laser wavelength and $w(z)$ the beam radius. Therefore the beam parameter q must be known at least at one point of the optical axis. It can be determined by measuring the beam radius at some locations along the z-axis and then fitting the function $w(z)$ to obtain the waist size w_0 as done in Fig. 1. The formalism of ABCD matrices now allows the prediction of the beam shape along the optical axis after i.e. lenses, so that the exact lens position is calculated to fit the beam into the cavity. This procedure is called mode matching.

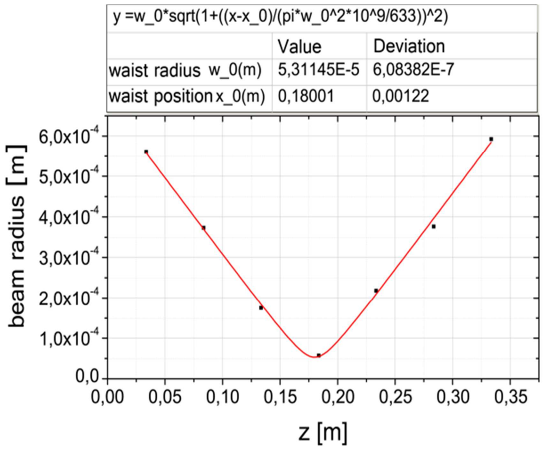

Fig. 1: *To identify the waist of the beam out of exp. data on the radius along the optical axis.*

Resonance is fulfilled once the round trip phase shift of the light inside the cavity equals 2π, in other words the path for one round trip matches an even number times the wavelength. Therefore the resonant frequencies are seperated by a certain distance, namly the free spectral range (FSR), which only depends on the geometry of the used resonator.

In fact, the relation between FSR and FWHM of a resonance peak is directly linked to the reflectivity of both mirrors. It is called the cavity's finesse [3]

$$F = \frac{FSR}{FWHM} = \frac{\pi\sqrt{r_1 r_2}}{1 - r_1 r_2},$$

where r_1 and r_2 are the reflection coefficients of both mirrors.

The used laser is a 1550 nm fibre laser, driven at 5 W output power, which is thermically tunable in wavelength a few pm around the center wavelength. To observe resonance peaks, not the frequency is varied but the spacing between the mirrors. One mirror is continuously slightly shifted back and forth, so that at least two peaks are visible in the transmitted signal. Using a 5 pm shift in wavelength at the laser as a reference, the FSR is determined as shown in Fig. 2.

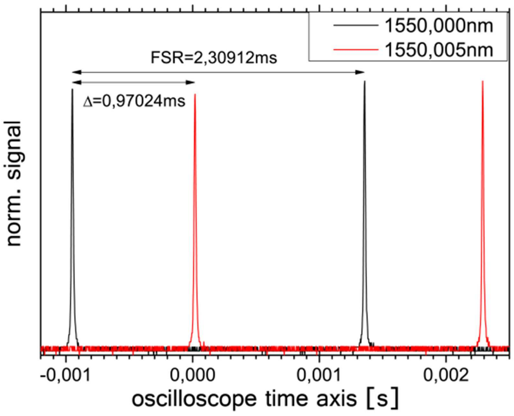

Fig. 2: *The FSR in frequency units is obtained by comparison to a 5 pm shift in wavelength.*

Having this, also the scale from the oscilloscope can easily be transformed into a wavelength or frequency axis and then, by fitting a Lorentzian function onto a resonance peak, the required FWHM is received like in Fig. 3. Rearranging the equation given for the finesse finally leads to the reflectivity.

At first glance, the result doesn't look satisfying. For a tested mirror, in this case a high reflectivity multilayer coating on a fused silica substrate, with this method, 98,38% reflectivity was measured with a relative uncertainty of 0,02%, while the manufacturer ensured a reflectivity of 99,55% for this wavelength. This deviation is basically due to the assumption made in deriving the finesse, namely that all dissipations during one round trip are due to transmission of light through the mirrors. Other losses are not taken into account and therefore lower the result for reflectivity. The big advantage of this method is that almost no statistical random errors occur in the measurement, hence all results just have some offset that can be gained from testing one known reference to calibrate the cavity.

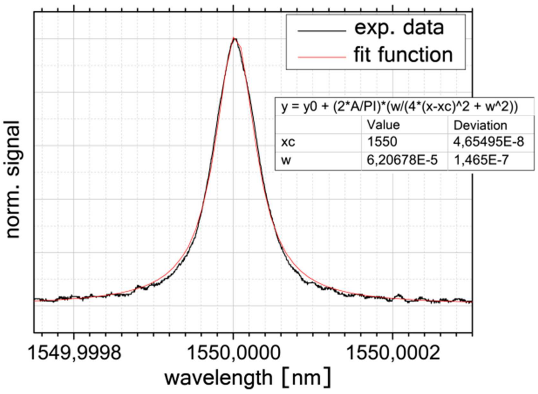

Fig. 3: *A resonance peak described by a Lorentzian function (red).*

Once calibrated, the optical resonator is able to precisely measure reflectivity. In comparison to other methods, it is has a much higher signal-to-noise ratio, so that one could say it is not limited by noise.

References

[1] PTB *http://www.ptb.de/cms/fileadmin/internet/fachabteilungen/abteilung_4/4.2_bild_und_wellenoptik/Optische_Atomuhren.pdf* (2013)

[2] G. Hammond, Insitute for Gravitational Research, University of Glasgow, (2013).

[3] W. Nagourney, *Quantum Electronics for Atomic Physics.* Oxford Graduate Texts, Oxford University Press (2010).

A flexible solid state tunnelling spectroscopy tool set

Volker Tympel, David Reifert

Spectroscopy is an essential method in modern solid state physics. But in our days spectroscopy is not focused on the interaction of photons only. Especially the interaction with electrical charge carriers is important to understand the physics of new materials or electronic devices [1]. Small changes of the electrical resistance or conductivity have to be detected and a lock-in-amplifier is a method to do so.

Grounding in a complex measurement-set is often a difficult task and a source of a drop-in. Therefore, we are using an inductive mixer to couple the DC-component and the AC-lock-in output-signal based on home-made transformer with a VITROVAC 6030 core.

The system is able to detect small 1‰-changes in the resistance using small signals only but it is more powerful than a numerical calculation via the 1st derivative of a measured voltage-current (V-C) curve [Fig. 1] and the resolution can be scaled via the lock-in integration time [Fig. 2].

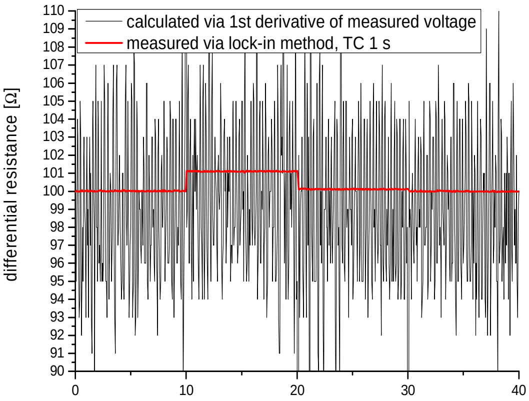

R_{test} = 100 Ω | 101 Ω |100.1 Ω | 100 Ω

Fig. 1: *Resistor test set, R, R+1%, R+1‰.*

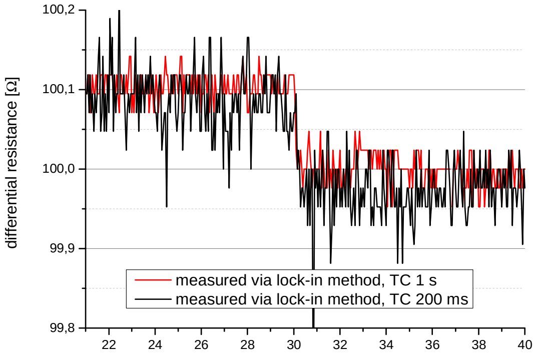

R_{test} = 100.1 Ω | 100 Ω

Fig. 2: *Zoomed resistor test set, R+1‰, R, at different integration Time Constance (TC).*

So the tool set can be used to measure the C-V curve [Fig. 3] and the differential resistivity or conductivity simultaneously with a lower noise level compared to any numerical methods [Fig. 4]. For a larger range of resistivity or conductivity it should be noted that the source resistance R_s of the mixer has to be comparable to maximal sample resistance $R_{x\text{-}max}$.

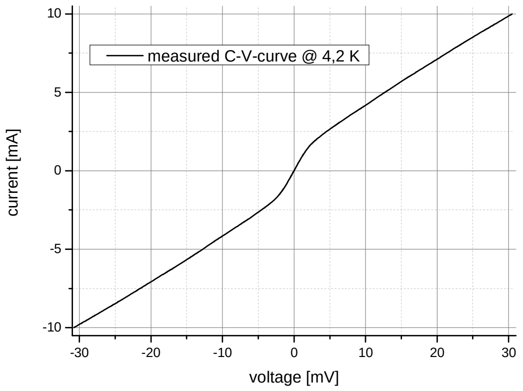

Fig. 3: *C-V curve of a Pb/In – Al/Al-oxide – Co-doped Ba-122 junction.*

The unknown local resistance R_x or conductivity $^1/_{R_x}$ will be obtained from the measured lock-in AC-voltage U_x using the equation: $R_x = \frac{R_S}{\left[\frac{U_{ref}}{Ux}\left(\frac{R_S}{R_{ref}}+1\right)\right]-1}$ with U_{ref} as measured lock-in AC-voltage at a known reference resistance R_{ref}.

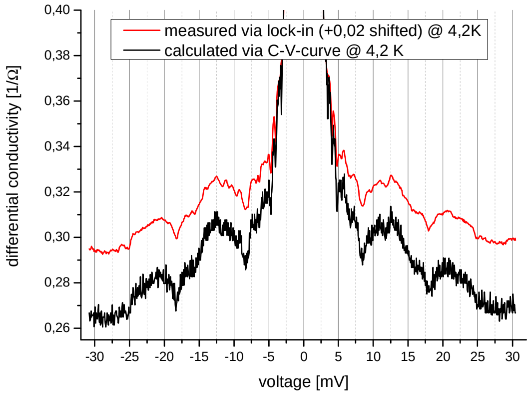

Fig. 4: *Measured and calculated spectra of a Pb/In – Al/Al-oxide – Co-doped Ba-122 junction.*

Also other problematic electrical behaviours can be investigated with the tool set [Fig. 5]. For example, it is possible to find interesting features in noise signals [Fig. 6] – like very small Shapiro-steps behaviour [Fig. 7].

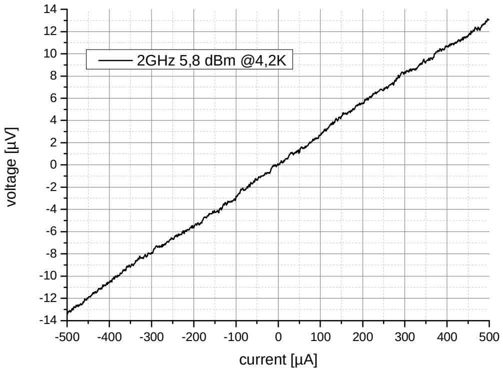

Fig. 5: *The V-C curve of a Pb/In – Co-doped Ba-122 junction with an undefined barrier under microwave radiation and unremarkable behaviour like a mΩ-resistor.*

It could be shown that this spectroscopy tool set is high sensitive and flexible. And it is also easy to switch from the differential resistance *dV/dI* to the second derivation d^2V/dI^2 for inelastic tunnelling and phonon spectroscopy by using the second harmonic mode of lock-in amplifier [2].

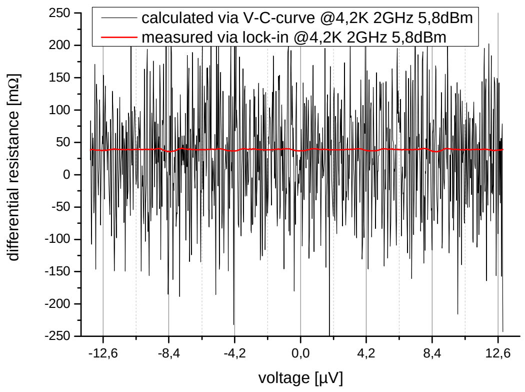

Fig. 6: *The calculated and measured curves of the differential resistance of a Pb/In – Co-doped Ba-122 junction with an undefined barrier under microwave radiation.*

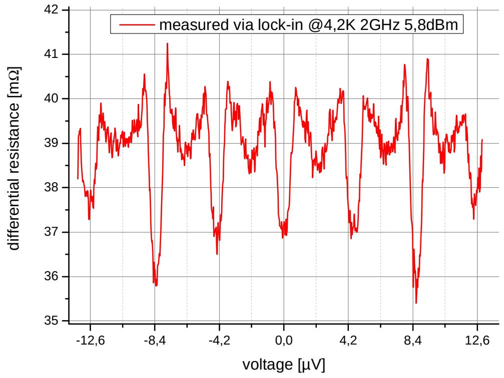

Fig. 7: *The measured and zoomed curves of the differential resistance of a Pb/In – Co-doped Ba-122 junction with an undefined barrier under microwave radiation with clear step behaviour.*

References

[1] E.L. Wolf, Principles of Electron Tunneling Spectroscopy: Second Edition, Oxford Uni. Press, VI-IX (2012).

[2] Model 7260 DSP Lock-in Amplifier Instruction Manual, 5-10 (1998).

Thermoelastic damping of a silicon disc

Daniel Heinert, Geppo Cagnoli[1]*, Alan Cumming*[2]*,*
Massimo Granata[1]*, Iain Martin*[2]*, Ronny Nawrodt*

[1]*Laboratoire des Matériaux Avancés, IN2P3/CNRS, Université de Lyon, France*
[2]*SUPA, School of Physics and Astronomy, University of Glasgow, United Kingdom*

Interferometric gravitational wave detectors are among the most sensitive devices in our time. Detectors of the second generation as aLIGO [1] are under installation at the moment and are expected to allow the detection of relative length changes in the order of 10^{-23}. This performance is likely to result in the first direct detection of gravitational waves.

A crucial point in the design of these detectors is the minimization of different noise sources. Besides seismic noise and optical quantum noise especially thermal noise has to be reduced as it can dominate the most sensitive frequency band of such a detector. In a typical detector the mirrors are realized by a highly reflective layer stack on top of a substrate. Previous papers [2] have identified the Brownian thermal noise of these coating layers as the most important thermal noise process.

Different strategies exist to minimize the Brownian coating noise level. One of them is to decrease the mechanical loss ϕ of the coating material leading to a decrease in noise via the fluctuation-dissipation theorem [3]. Most schemes to measure mechanical loss rely on the use of a base structure elastically supporting the relevant coating layer. The coating loss is then obtained by a comparison of the mechanical loss of the uncoated and the coated sample. In such a scheme additional noise processes will increase the mechanical loss level of the uncoated sample and increase the minimum detectable coating loss.

Thermoelastic (TE) damping represents such an additional loss process. For that reason this report investigates TE damping of a thin silicon disc. Its thickness is assumed as 460 µm and the diameter as 76.2 mm.

Often the solution of a one-dimensional beam by Zener [4] is used to estimate the expected TE loss of a disc. For bending modes of a rectangular beam it reads

$$\phi = \frac{Y\alpha^2 T}{\rho C}\frac{\omega\tau}{1+\omega^2\tau^2},$$

where Y is Young's modulus, α linear thermal expansion, ρ mass density, C specific heat of silicon and T the temperature. Further the frequency dependence is given by the constant τ via

$$\tau = \left(\frac{h}{\pi}\right)^2 \frac{\rho C}{\kappa},$$

where κ represents the thermal conductivity and h the beam height.

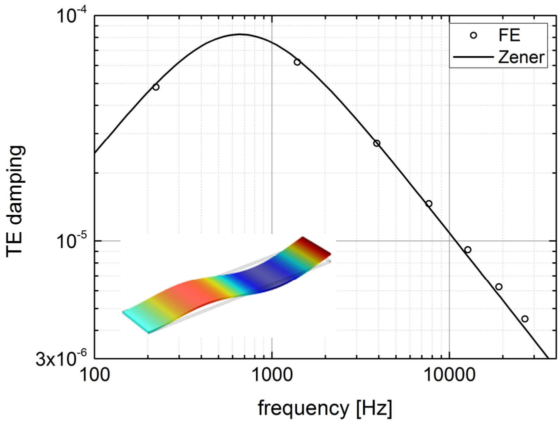

***Fig. 1:** Numerical results for the thermoelastic damping of an isotropic (Y=130 GPa,ν=0) rectangular beam (5 cm×1 cm×460 µm).*

In the following Zener's result is compared to a rigorous numerical calculation for a disc using the finite element (FE) package COMSOL [5]. For a detailed description of this calculation see Ref. [6]. To check our FE code we start with the case of a rectangular beam. The result is given in Fig. 1 showing a nice coincidence between the analytical and the FE results. It guarantees that the mesh density of our model is high enough.

In a second calculation the TE damping of a crystalline silicon disc has been considered taking its anisotropic elastic behavior into account. The results are illustrated in Fig. 2.

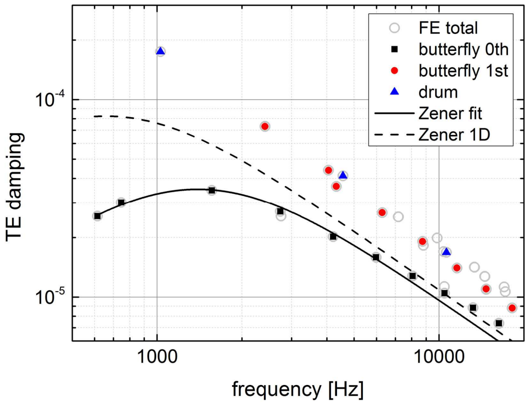

Fig. 2: *Numerical results for the thermoelastic damping of an anisotropic silicon disc The complete set of FE results are indicated by grey dots. The colored symbols refer to different mode shape families.*

The results indicate the emergence of two groups of mode shapes with a different frequency dependence of TE damping. Here the butterfly modes of zeroth radial order form one of these groups and are nicely fitted by the classical Zener solution. Although the Zener equation is helpful to fit the FE results, a strict evaluation of the analytical expression reveals the dashed line in Fig. 2 introducing large deviations especially at low frequencies.

The remaining modes exhibit a higher TE damping and do not show a maximum in the investigated frequency range. At 1 kHz their loss is one order of magnitude larger than that of the first group. The mode shapes belonging to the different symbols are illustrated in Fig. 3.

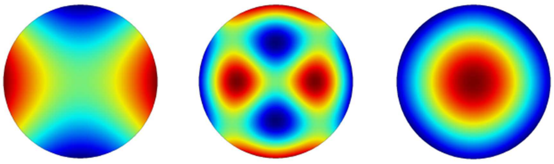

(a) (b) (c)

Fig. 3: *Exemplary mode shapes for a butterfly mode of radial order zero (a) and radial order one (b) as well as a drum mode (c).The color code shows the displacement perpendicular to the circular surfaces. Green regions are at rest while red and blue regions strongly move.*

While the Zener equation correctly describes the TE damping of bending modes in beams we showed that its application to the TE damping of a disc gives wrong results. This finding has to be considered in the choice of suitable modes for coating loss measurements. Especially the butterfly modes of zero radial order are promising candidates in this respect. Further the FE code COMSOL proved as a valuable tool to determine mode frequencies and TE damping for arbitrary geometries.

This work was supported by the DFG under contract SFB Transregio 7.

References

[1] G.M. Harry, Class. Quantum Grav. **27**, 084006 (2010).
[2] R. Nawrodt *et al.*, Gen. Relativ. Gravit. **43**, 593-622 (2011).
[3] H. Callen and T. Welton, Phys. Rev. **83**, 34-40 (1951).
[4] C. Zener, Phys. Rev. **52**, 230-235 (1937).
[5] www.comsol.com
[6] D. Heinert *et al.*, J. Phys.:Conf. Ser. **228**, 012032 (2010).

Influence of different surface machining techniques on the thermal conductivity of sapphire at low temperatures

Christian Schwarz, Bastian Walter, Gerd Hofmann, Daniel Heinert, Julius Komma, Paul Seidel, Ronny Nawrodt

The detection of gravitational waves belongs to the most challenging projects of mankind. In order to increase the detection probability of these detectors it has been successfully shown [1] that the operation at cryogenic temperatures leads to an enhancement of the sensitivity which is currently limited by thermal noise.

So far only the Japanese interferometric detector CLIO has been modified for pioneering low temperatures. All other interferometric gravitational wave detectors run at room temperature. Currently, different detector concepts are under investigation. A crucial part is the lower stage of the suspension system for the optical test masses like mirrors and cavity couplers. This suspension serves two purposes: One is the mechanical decoupling from any seismic disturbances the other is the extraction of heat from the optics to keep them at a fixed temperature preventing any uncontrolled warming. The origin of the heat is thermal radiation from warm parts of the detector and the absorption of laser light, especially if the light transmits through the optic as it is the case for the cavity couplers.

While the seismic decoupling in general works best with thin fibres [2] the suspension design (length and cross section) of a low temperature detector is dominated by the requirements for the heat extraction due to the fact that the heat transfer through the fibre is the only transport mechanism available.

Sapphire as it will be used for the optics of the KAGRA detector also serves as a suspension material showing very high thermal conductivity values below 50 K [3]. To achieve the required values in the order of several thousands of W/(mK) the surface roughness [4], geometric dimensions (length L, cross section A) of the suspension fibres and the purity grade of the material have to be taken into account.

To probe the influence of the surface roughness corresponding to different machining states the thermal conductivity of four different samples was measured. All samples were made from the same crystal and showed the same geometry (100 × 5 × 0.8) mm.

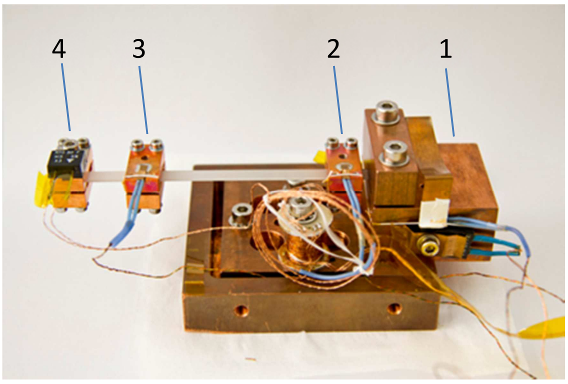

***Fig. 1**: Experimental setup for thermal conductivity measurements on sapphire ribbons. 1 – heat sink, 2 & 3 temperature difference sensors, 4 – heater.*

In order to measure the thermal conductivity κ one end of the ribbon has been attached to a heat sink as shown in fig. 1. Followed by two clamps with silicon diode temperature sensors fixed in a given distance L to each other a heater is clamped on the free end of the ribbon.

After stabilising all clamps to a desired temperature a small amount of heat was applied at the free end of the ribbon with the electric heater. Then the equilibrium temperature difference between the inner two sensors was recorded. After that the heater power has been increased and the new temperature difference ΔT was again recorded. This procedure of heating and waiting for stable temperature distribution has been continued until depending on the heat sink temperature a reasonable maximum of heater power was reached.

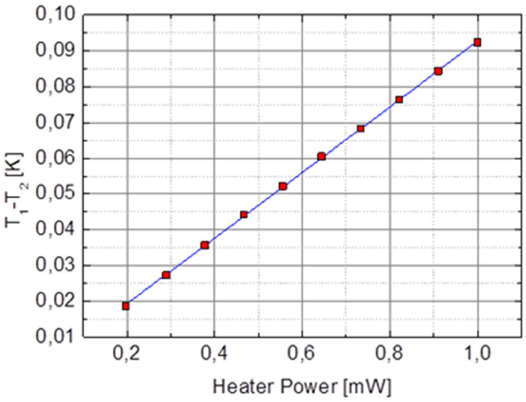

Fig. 2: *Temperature difference ΔT change between two sensors separated by a distance L due to an increase of heater power P.*

By plotting ΔT vs. P one can derive a linear slope as shown in fig. 2 from which the value of κ can be calculated as follows:

$$P = \frac{A}{L}\kappa\Delta T \;\Rightarrow\; \kappa = \frac{P}{\Delta T}\frac{L}{A}.$$

This procedure has been repeated for every data point plotted in fig. 3.

In the investigated samples the thermal conductivity must be limited by the smallest geometrical dimension [5] which explains the gap to the values of a much larger bulk sample. But that doesn’t explain the deviation between the measured curves because all samples had the same geometry. It is obvious that the available surface machining techniques lead to different values of κ obtained at a fixed temperature. Due to the machining dependent introduction of more or less deep cracks near the surface phonon scattering occurs which leads to a general reduction of κ below 50 K and a shift of the maximum (around 30 K to 40 K) to higher temperatures. Fine grinding shows the lowest values while a decreasing roughness from fine diamond grain polished to inspection polished leads to slightly higher values. A significant improvement can be achieved if the geometry of the sample allows the use of a CMP process.

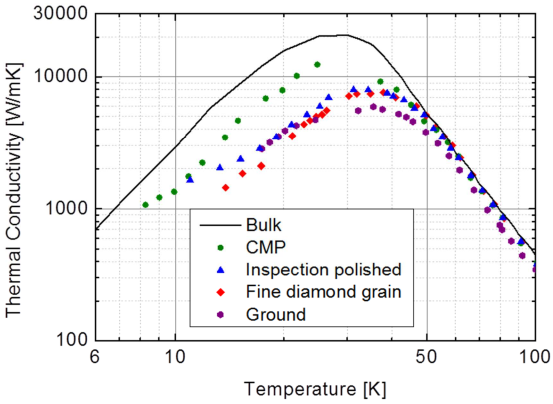

Fig. 3: *Comparison of thermal conductivity values for different samples. The black line represents bulk reference values [6].*

At temperatures above 50 K the difference between all investigated samples and the bulk reference values becomes negligible small.

This work was supported by the DFG under contract SFB Transregio 7 and the EU ELiTES project (IRSES no 295153).

References

[1] S. Miyoki, Class. Quantum Grav. **21**, S1173–S1181 (2004).

[2] A. Cumming, Class. Quantum Grav. **29,** 035003 (18pp) (2012)

[3] R. Berman *et al.*,Proc. R. Soc. Lond. A 19 (1955)

[4] R. O. Pohl, Phys. Rev. Lett. **8** (1962)

[5] P. Carruthers, Rev. Mod. Phys. **33** (1961)

[6] Y. S. Touloukian : Thermophysical Properties of Matter, IFI/Plenum, New York (1970)

Bicrystal grain boundary junctions of P-doped Ba-122

Stefan Schmidt, Takahiko Kawaguchi[1], *Sebastian Döring, Frank Schmidl, Fritz Kurth*[2],
Hiroshi Ikuta[1], *Paul Seidel*

[1] *Nagoya University, Dept. of Crystalline Materials Science, Chikusa-ku, 464-8603 Nagoya*
[2] *IFW Dresden, Institute for Metallic Materials, Helmholtzstraße 20, 01069 Dresden*

Knowledge about the physics of grain boundaries is a key to understand and optimize conducting processes in granular materials, i.e. polycrystalline or textured cables [1]. Detrimental grain boundaries occur naturally and limit the conductance of high-T_C superconductor cables. The critical current density of YBCO decreases quickly at grain boundary angles above 5°. Co-doped Ba-122 as one member of the pnictide superconductor family develops a rather shallow decline with reasonable critical current densities around 10^6 A/cm² up to 15°. First measurements of P-doped Ba-122 compared with Co-doped Ba-122 suggest an equivalently shallow decline with a higher starting value (10^7 A/cm² intragrain j_C) and thus higher j_C values at large grain boundary angles on MgO [2].

P-doped Ba-122 thin films have successfully been deposited via pulsed laser deposition (PLD) and molecular beam epitaxy (MBE). The PLD thin films investigated by Adachi et al. [3] have reasonably high j_C of $3{\cdot}10^6$ A/cm² and T_C (onset 26.5 K) values. Our project partners from Nagoya University prepared P-doped Ba-122 thin films on LSAT ($\theta = 45°$) with an excellent quality by MBE [4] and achieved j_C values of 10^7 A/cm² with a T_C of 31 K (onset). They used the solid sources Ba, Fe, As, GaP in separated Knudsen cells, which allows a fine tuning of the stoichiometry of the Ba-122 and its dopant P. The big difference in vapor pressure of Ga and P is utilized in the GaP source to avoid the highly dangerous P_4.

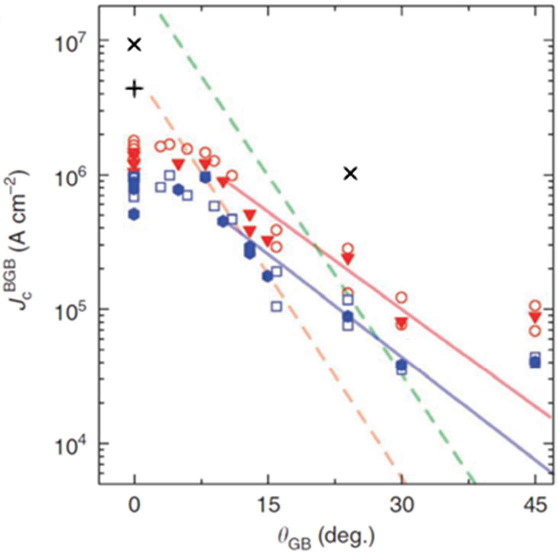

Fig. 1: *Critical current density vs grain boundary angle [5]. The black + and x mark results from P-doped Ba-122 samples on MgO by PLD [3] and MBE [2], respectively.*

The Ba-122 microbridges exhibit symmetric I-V characteristics, which can be fitted by a flux-flow (FF) extension of the resistively shunted junction (RSJ) model as shown by Saitoh et al. [6].

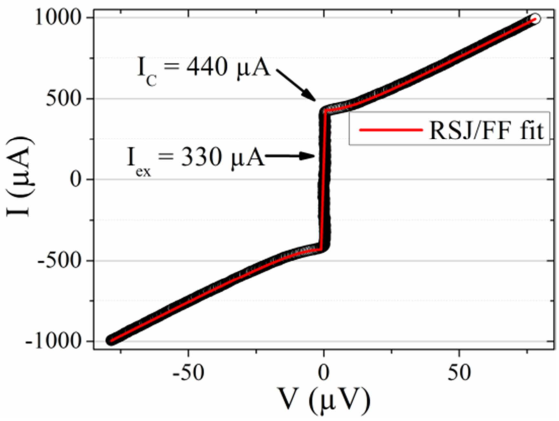

Fig. 2: *Current vs voltage of a GB junction (bridge width 10 µm) with RSJ/FF fit [4].*

A formal I_C of 440 µA as visible in figure 2 leads to a formal I_CR_N product 45 µV which has to be corrected to a value as low as 11 µV when taking I_{ex} into account. The resulting critical current density is $7.2 \cdot 10^4$ A/cm². It will be investigated, how the substrate material, i.e. LSAT and MgO influences this value.

Shapiro steps up to a high order could be observed under microwave irradiation. At a microwave frequency of 8.4 GHz not only full-integer Shapiro steps, but also half-integer ones occur (see Fig. 3) at voltages $f \cdot m \cdot h/2e$, where f is the irradiation frequency, m is a multiple of 1/2 and $h/2e$ ($= 2.07 \cdot 10^{-15}$ Wb) is the magnetic flux quantum.

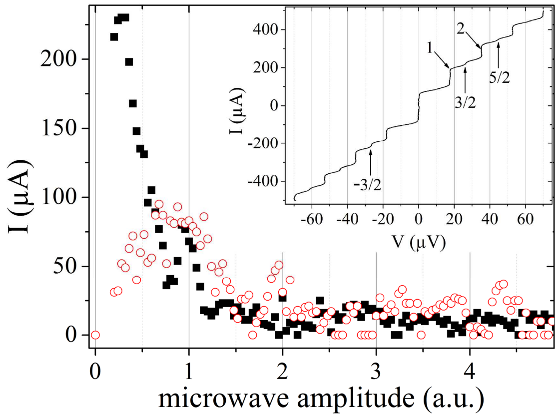

Fig. 3: *Critical current (black squares) and height of the 1st Shapiro step (red circles) of a GB junction (bridge width 7 µm) vs microwave power (f = 8.4 GHz). Inset: Current vs voltage of the same junction at a microwave power of 0.92. The arrows mark (half-) integer Shapiro steps indexed with the corresponding m.*

The magnetic field dependence could not be observed in a standard dewar measurement setup with small Cu coils just next to the sample, because the resulting magnetic field of only a few 100 µT was not sufficient to suppress the critical Josephson current completely. Thus, a large NbTi-Helmholtz coil inside a ^{3}He cryostat was used in order to increase the magnetic field strength up to 2.5 T. The critical Josephson current is suppressed by the external magnetic field and modulates non-periodically, see Fig. 4. This could be caused by a network of Josephson junctions within the microbridge. This kind of network would result in a pattern summarized by several Fraunhofer-like curves, which could lead to enhancement or obliteration of minor maxima.

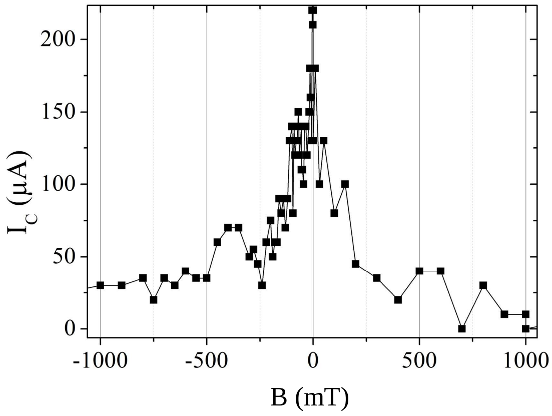

Fig. 4: *Critical current of a GB junction (bridge width 7 µm) vs magnetic field. The line acts just as a guide while ignoring error bars.*

Further experiments will be conducted at different grain boundary angles order to consolidate our knowledge about the transport mechanisms between the grains. Additionally, samples on MgO bicrystal substrates will also be investigated.

References

[1] Y. Ma et al., *Supercond. Sci. Technol.* **25,** 113001 (2012)

[2] A. Sakagami *et al.*, Physica C **494**, 181-184 (2013).

[3] S. Adachi *et al.*, Supercond. Sci. Technol. **25**, 105015 (2012).

[4] S. Schmidt *et al.*, *J. Phys.: Conf. Ser.* (2014), accepted.

[5] T. Katase *et al.*, *Nat. Comm.* **2**, 409 (2011).

[6] K. Saitoh *et al.*, *Jpn. J. Appl. Phys.* **36**, 272-275 (1997).

Particle diagnostics for FAIR: Non-destructive beam current monitoring based on a Cryogenic Current Comparator

René Geithner, Ralf Neubert, Wolfgang Vodel*, Paul Seidel*

**Helmholtz-Institut Jena, Fröbelstieg 3, 07743 Jena, Germany*

Monitoring of ion beam intensities in particle accelerators without affecting the beam guiding elements, interrupting the beam current or influencing its profile is a major challenge in accelerator technology. A solution of this issue is the detection of the magnetic field generated by the moving charged particles. In a joint effort of Institute of Solid State Physics at FSU Jena and Helmholtz-Institute Jena a non-destructive beam monitoring system for particle beams in accelerators based on the Cryogenic Current Comparator (CCC) principle was recently developed [1].

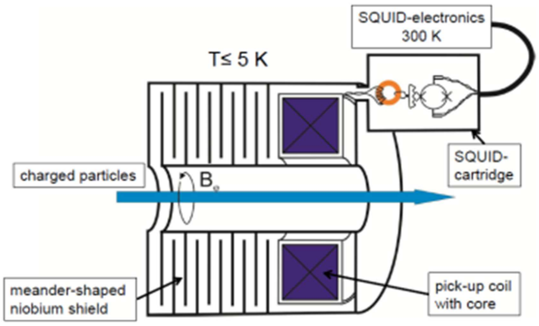

Fig. 1: *Schematic view of the CCC. Only the azimuthal magnetic field of the beam current passes the meander shaped shielding, all other magnetic field components are highly attenuated. The azimuthal magnetic field induces screening currents in the superconducting pick-up coil, which are detected by the SQUID sensor. Because of the superconductivity of all sensing parts, the CCC is able to detect continuous as well as pulsed beam currents.*

The CCC consists of a high-performance low-temperature DC superconducting quantum interference device system, a superconducting toroidal pick-up coil and an extremely effective meander-shaped superconducting niobium shield. This device allows the measurement of continuous as well as pulsed beam currents in the nA-range. The resolution and the frequency response of the detector strongly depend on the toroidal pick-up coil and its embedded ferromagnetic core.

The current spectral density $\langle I^2 \rangle$ of a coil at a temperature T could be calculated with the Fluctuation-Dissipation-Theorem (FDT) and the measured frequency dependent serial inductance L_S (ν) respectively serial resistance R_S (ν) in the equivalent circuit diagram of a real coil, whereas R_S (ν) represents the total losses [2]:

$$\left\langle I^2 \right\rangle = 4k_B T \int \frac{R_S(\upsilon)}{\left(2\pi\upsilon\left(L_{SQUID} + L_S(\upsilon)\right)\right)^2 + \left(R_S(\upsilon)\right)^2} d\upsilon \quad .(1)$$

Investigations of both the temperature and frequency dependence of the relative permeability and the noise contribution of several nanocrystalline ferromagnetic core materials were carried out to optimize the CCC with respect to an improved signal-to-noise ratio and extended transfer bandwidth [3].

The current noise of the CCC could be decreased by a factor of five compared to previous systems [4] (see figure 2). This results from the usage of iron-based nanocrystalline Nanoperm [5] as core material for the pick-up coil. With this optimized CCC, a noise limited current resolution of 1 nA should be achievable in the disturbed environment of an accelerator [3].

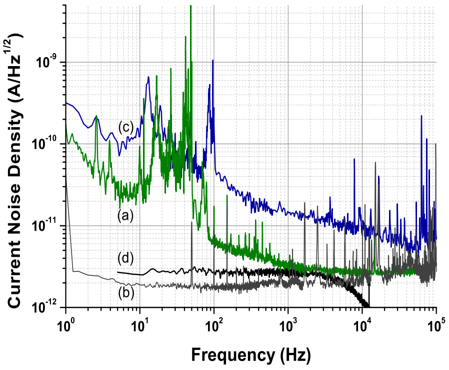

***Fig. 2:** The measured current noise density of the improved FAIR-CCC with Nanoperm M764 core (a) whereas plot (b) represents the intrinsic current noise density of the Supracon SQUID sensor CP2 blue. For comparison the measured current noise density of the DESY-CCC [3] pick-up coil including a Vitrovac 6025F core is shown (c) whereas plot (d) represents the intrinsic current noise density of the SQUID sensor UJ111 from Jena University.*

Figure 3 shows the full-bandwidth response of the FAIR-CCC to a rectangular current signal of 1.438 µA (a), 185 nA (b), and 42.5 nA (c) applied to the additional calibrating loop. There is no low pass filter or time-averaging used. The step function response for lower currents is quite linear as one can see from curves (b) and (c). From this curves it is also visible that there is no drift in the CCC signal during a time span of at least 15 s. At higher currents (curve (a)) an overshooting appears at the rising edge of the signal. The reason for this appearance has to be clarified in subsequent experiments.

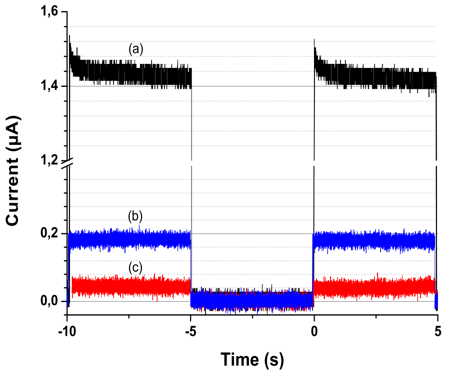

***Fig. 3:** Full-bandwidth response of the FAIR-CCC to a rectangular current signal of 1.438 µA (a), 185 nA (b), and 42.5 nA (c) applied to the additional calibrating loop.*

For the international FAIR project at Darmstadt it is foreseen to install several CCC detectors at the high-energy transport beam lines. Here, beam currents in the range between 10^{-4} and 10^{-2} mA are to be expected.

In addition the installation of a CCC system at CRYRING is planned for highly accurate absolute current measurements at low beam energies and small particle numbers for ions as well as for antiprotons.

References

[1] R. Geithner *et al.*, IEEE Trans. Appl. Supercond . **21**(3), 444-447 (2011).
[2] R. Geithner *et al.*, Cryogenics. **54**, 16-19 (2013).
[3] R. Geithner *et al.*, Proc. IBIC 2013, Oxford UK. TUPF32, 545 (2013).
[4] R. Geithner *et al.*, Rev. Sci. Instrum. ***82***, 013302 (2011).
[5] MAGNETEC GmbH, Industriestrasse 7, D-63505 Langenselbold, Germany.

Realization of arbitrary pinning patterns in $YBa_2Cu_3O_{7-\delta}$ thin films

Christian Katzer, Claudia Stahl[1], Joachim Albrecht[2], P. Seidel and Frank Schmidl

[1]*Max-Planck-Institut für Intelligente Systeme – Heisenbergstraße 3, D-70569 Stuttgart*
[2]*Hochschule Aalen – Beethovenstraße 1, D-73430 Aalen*

A drawback of high-temperature (high-T_c) superconducting $YBa_2Cu_3O_{7-\delta}$ (YBCO) thin films is that magnetic flux penetrates the film in form of flux vortices. Any movement of these flux lines leads to a dissipation of energy, thus decreasing the critical current I_c of the superconductor. Hence, an effective pinning of flux vortices by artificial pinning centers is a pre-requisite for high-current applications of YBCO thin films [1]. On the contrary, for a Josephson junction I_c must not be too high [2]. These border conditions directly demand a technique for a spatially resolved inclusion of pinning centers to locally control the critical current I_c of the film.

We have successfully shown that it is possible to use a dewetting process of thin gold layers for a local inclusion of gold nanoparticles [3]. Single crystal $SrTiO_3$ substrates were coated with a 3 nm gold seed layer and subsequently patterned using photolithography (see fig. 1). The patterned Au layer was overgrown by YBCO using pulsed laser deposition in an oxygen atmosphere [3].

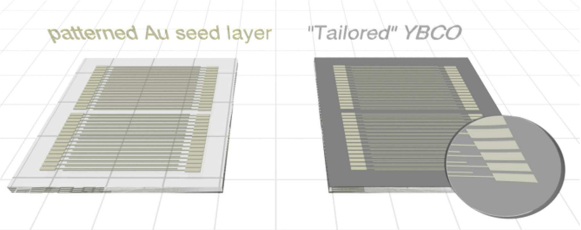

Fig. 1: *Patterning the Au seed layer allows to locally modify the YBCO thin film.*

Due to the high temperatures during the YBCO deposition a self-assembly of crystalline gold nanoparticles can be observed, leading to modified growth conditions of the YBCO film [4]. Interestingly, a sharp borderline between Au modified and non-modified YBCO can be found using scanning electron microscopy (see fig. 2) and the only limitations of the pattern resolution were set by our lithographic process. This indicates that the local modification of YBCO by embedding Au nanoparticles could be possible on even lower length scales. Furthermore, the distribution density of secondary phases - which can be seen as features on the right side of the image and which are observed as a general behavior in YBCO thin films [1] - was found to be drastically reduced in the Au modified areas.

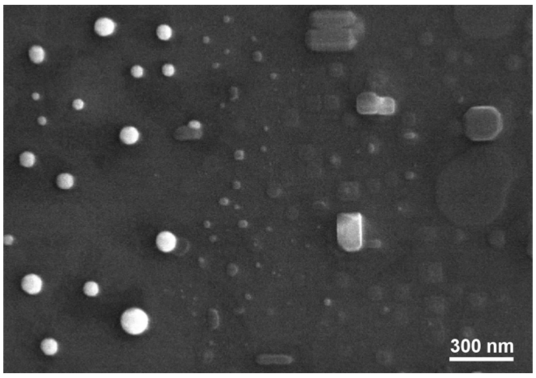

Fig. 2: *Circular, white Au particles can only be found on the left (Au modified) and the border appears to be sub-micrometer sharp.*

To measure the critical current density in our partly Au modified YBCO thin films we employed magneto-optical microscopy. Utilizing the Faraday effect, a locally resolved image of the flux density distribution was obtained which then could be converted into a local and quantitative map of the critical current density j_c using a numerical inversion of the Biot-Savart law [5]. The measurements were performed at a temperature of T = 10 K and the image was obtained in the remnant state after an external magnetic field of 200 mT was applied and subsequently removed.

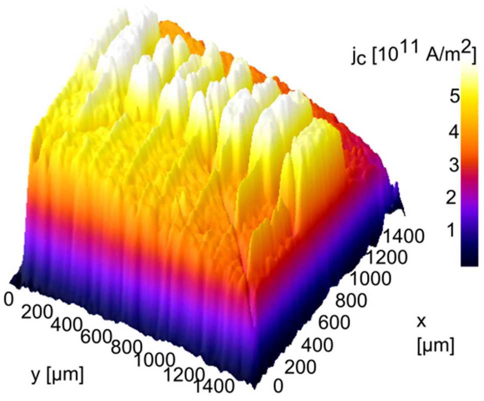

Fig. 3: *3D representation of the local crit. current density in a gold modified YBCO thin film.*

Note, that the critical current density was found to be increased from 4×10^{11} to 6×10^{11} A/m^2 in the Au modified areas. Furthermore, the pattern of increased current density exactly matches the pattern of the initial Au seed layer (compare figs. 1 and 3). Thus, by patterning the Au layer, arbitrary patterns of the critical current in high-T_c thin films can be realized, paving the way for high-quality electronic devices with an improved performance. Until now, no other low-effort method is known for a local tuning of I_c.

Using magneto-optical imaging it is also possible to visualize the hindering of flux penetration [3]. As can be seen in fig. 4 at a field of 16 mT flux already penetrated the non-modified YBCO thin film, whereas the Au modified parts of the film are still flux free. This is a direct evidence for an enhanced pinning which also explains the increased critical current in the Au modified areas.

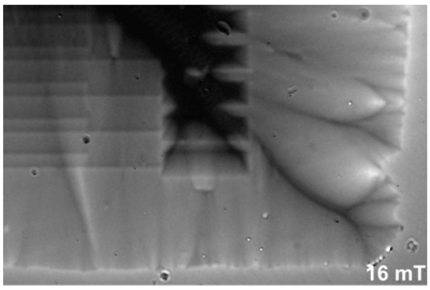

Fig. 4: *Flux density distribution at T = 10 K.*

The fact that the number of precipitates was reduced by embedding Au particles (see fig. 2) indicates that an increased pinning of flux vortices can't be caused by additional outgrowths and defects. Instead, as we could show, there are strong indications that the inclusion of Au nanoparticles even improves the YBCO structure [4]. However, we suggest that a locally strained region of YBCO is created in vicinity of nanoparticles, introducing nanostrain which lately was shown to be causing a significant pinning force [6].

In conclusion, we propose that a modification of the YBCO structure and additional strain at the nanoscale is causing the observed pinning of flux vortices. The arbitrary patterns of pinning structures our method allows to realize may be used for the production of advanced superconducting structures such as magnetic field sensors or electronic devices.

References

[1] S. Foltyn *et al.*, Nature Mater. **6**, 631 (2007).
[2] S. Wunderlich *et al.*, Physica C **340**, 51 (2000).
[3] C. Katzer *et al.*, New J. Phys. **15**, 113029 (2013).
[4] C. Katzer *et al.*, Supercond. Sci. Technol. **26**, 125008 (2013).
[5] C. Joos *et al.*, Rep. Prog. Phys. **65**, 651 (2002).
[6] A. Llordés *et al.*, Nature Mater. **11**, 329 (2012).

Low-temperature charge transport through ultra-thin Si films with dopants: from Coulomb blockade to resonant transmission

Vladimir Shaternik[1]*, Andrej Shapovalov*[1]*, Mikhail Belogolovskii*[2]*, Sebastian Döring,*
Stefan Schmidt, and Paul Seidel

[1] *G.V.Kurdyumov Institute for Metal Physics, 252680 Kyiv, Ukraine*
[2] *Donetsk Institute for Physics and Engineering, 83114, Donetsk, Ukraine*

It is becoming increasingly evident that silicon can be an excellent host material for an entirely new generation of devices partially because dopants in Si represent the ultimate limit of quantum dots. The Coulomb interaction between an electron on a donor and all other electrons in its environment can be parametrized by a single capacitance C. The charging energy $e^2/2C$ leads to the appearance of the Coulomb blockade effect [1]. Since the barrier conductance decreases exponentially with its thickness increased, direct charge tunneling of electrons through a Si layer occurs only in extremely thin films. For thicker films, the transport through dopant states is expected for voltages V exceeding a threshold value related to the charging energy. As a result, the Coulomb gap manifests itself in an increased differential dI/dV-vs-V resistance around $V = 0$.

The first aim of our experiments was to check this effect in trilayered junctions made of MoRe alloy electrodes with a Si interlayer doped by W. Superconducting MoRe films with a thickness of $d \approx 100$ nm were fabricated by magnetron sputtering. The target consisted of a pure Si wafer with a certain number of tungsten wires used to obtain Si barriers doped by W clusters with a tungsten concentration c_W between 0 and 10 at.%. For ultrathin ($d < 10$ nm) pure Si barriers as well as those with a low degree of doping ($c_W < 5$ at.%), I-V characteristics have not exhibited any nonlinearities (curve 1 in Fig. 1). For thicker barriers a strong suppression around $V = 0$ was revealed (curves 2 and 3 in Fig. 1).

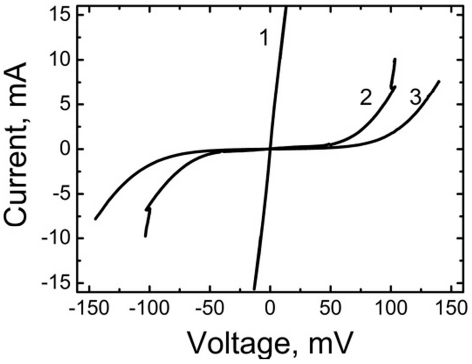

Fig. 1: *I-V* curves of MoRe-Si(4 at.% W)-MoRe junctions with thicknesses of the Si(W) barrier d = 9, 13, and 15 nm (curves 1, 2, and 3, respectively); temperature T = 4.2 K.

Let us estimate the charging energy of a W impurity with a radius $R \sim 1$ nm. Its capacitance $C \approx \varepsilon R$, with $\varepsilon = 12$ for Si, determines the threshold voltage value $\sim e^2/(2\varepsilon R) \approx 60$ meV which agrees well with the measured data (Fig. 1). These considerations are justified when the impurity radius R is very small. If the dopant concentration increases, metal nanoclusters with individual localized energies ε_0 are growing inside the Si layer. In this case, a resonant passage of electrons becomes possible along special resonance-percolation trajectories with periodic arrangement of the nanogranules and almost coinciding localized levels [2]. It is improbable that the optimal trajectory is sinuous, so the problem is close to one-dimensional. Let us consider a simplified case of a single localized state [3] within a semiconducting layer located between two metallic leads near the central point. If so, the probability to transmit the interelectrode gap for an electron with an energy ε can be approximated by the Lorentzian $D(\varepsilon) = [1+(\varepsilon - \varepsilon_0)^2]^{-1}$. Now we assume that the spread of atomic localization energies is very large and they are uniformly ranging from zero to infinity. The related analytical result $\rho(D) = \hbar\bar{G}\left[e^2 D^{3.2}(1-D)^{1/2}\right]^{-1}$ with $\bar{G}$, the disorder-averaged junction conductance, was obtained earlier in [4] for ultrathin disordered interfaces but is valid in our case as well. The main conclusion is that the function ρ(*D*) is bimodal with a large number of strongly reflected “closed” channels and, at the same time, a significant amount of “open” channels with $D \leq 1$.

The second aim of the work was to verify the novel functionalities emerging due to the disorder in doped semiconducting films, namely, existence of the universal transparency distribution function $\rho(D)$ by measuring superconducting gap Δ induced features in *I-V* characteristics of MoRe-Si(W)-MoRe junctions with further increased concentration of W dopants up to 10 at.%. Our goal was to check the analytical form of the bimodal distribution function without any fitting parameters. To realize that, we have analyzed two quantities which can be directly extracted from a current-voltage characteristic of a Josephson SIS junction: the critical supercurrent I_s at $V = 0$ and the excess current I_{exc}, a constant shift of the superconducting *I-V* curve towards that measured in the normal state at *V* exceeding Δ/e [5]. The latter parameter can be found by extrapolation of the resistive part of the *I-V* curve at high voltages back to the axis $V = 0$. The voltage where the extrapolation starts from should not be far from $V = \Delta/e$ since significant nonlinearities in *I-V* characteristics can be caused even at small voltages by hot spots between two conducting banks of the tunnel junction.

In the absence of a barrier the two currents are $I_s = \pi\Delta/(eR_N)$ [6] and $I_{exc} = 8\Delta/(3eR_N)$ [5], hence $I_s/I_{exc} = 1.18$ with R_N, the normal-state resistance. In a realistic situation only a part of the channels is opened and the ratio increases. We have calculated the I_s/I_{exc} ratio averaging general formulas for an arbitrary transmission coefficient *D* [5,6] with the universal distribution function $\rho(D)$, see above. We have obtained that the ratio $I_s/I_{exc} = 1.73$ in this case. In Fig. 2 we show experimental data for a MoRe-Si(7.5 at.% W)-MoRe junction with the barrier thickness $d = 15$ nm. The ratio $I_s/I_{exc} \approx 1.7 - 1.8$ extracted from the measurements is in the excellent agreement with our theoretical simulations.

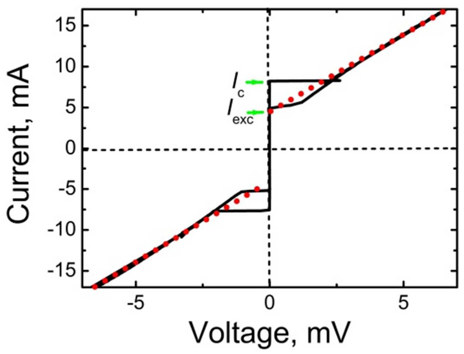

Fig. 2: *Hysteretic I-V curve of a MoRe-Si(c_W = 7.5 at.% W)-MoRe junction with the thickness d = 15 nm; T = 4.2 K. Values of critical I_s and excess I_{exc} currents are shown by arrows.*

References

[1] I. Giaever and H.R. Zeller, Phys. Rev.Lett. **20**, 1504 (1968).

[2] I.M. Lifshitz and V.Ya. Kirpichenkov, Zh. Eksp. Teor. Fiz. **77**, 989 (1979).

[3] H. Knauer, J. Richter, and P. Seidel. phys. stat. sol. (a) **44**, 303 (1977).

[4] K.M. Schep and G.E.W. Bauer, Phys. Rev. B **56**, 15860 (1997).

[5] G.E. Blomder, M. Tinkham, and T.M. Klapwijk, Phys. Rev. B **25**, 4515 (1982).

[6] A.A. Golubov, M.Yu. Kupriyanov, and E. Il’ichev, Rev. Mod. Phys. **76**, 411 (2004).

Shapiro step on the rc-branch of a shunted Josephson junction IV-characteristics

Yu. M. Shukrinov[1,2], *I. R. Rahmonov*[1,3], *K. V. Kulikov*[1,2], *P. Seidel, E. Il'ichev*[4]

[1]*BLTP, Joint Institute for Nuclear Research, Dubna, Moscow Region, 141980, Russia*
[2]*Dep. of Theoretical Physics, International University of Dubna, Dubna, 141980, Russia*
[3]*Umarov Physical Technical Institute, TAS, Dushanbe, 734063 Tajikistan*
[4] *Institute of Photonic Technology, P.O. Box 100239, D-07702 Jena, Germany*

One of the important problems on the way of using the intrinsic Josephson junctions (JJ) in HTSC as terahertz electromagnetic wave sources is the synchronization of all junctions in a stack to increase the power of radiation. Intensive attempts to solve this problem are based on using LC-shunting which leads to such synchronization [1,2,3]. JJ together with the LC elements built an oscillatory circuit. When the Josephson frequency ω_J becomes equal to the natural frequency of the circuit ω_{rc}, oscillations in JJ are tuned to this frequency. This resonance is manifested in the current-voltage characteristic (CVC) in the form of various features such as steps [4,5], humps or dips[6,7], the so-called resonance circuit branch (rc-branch). In particular, the existence of steps in the current-voltage characteristic in various systems of JJ with a resonance circuit was reported in a number of experimental and theoretical works [1,8].

In Ref. [9] the possibility of the appearance of an additional parametric resonance owing to the resonance circuit formed in the system of coupled JJ with LC shunting has been demonstrated. The condition of resonance is $\omega_{rc} = 2\omega_{LPW}$, where ω_{rc} - circuit frequency and ω_{LPW} - longitudinal plasma wave frequency.

In this paper, we study the influence of the external electromagnetic radiation on the phase dynamics in JJ shunted by LC-elements. We simulate the CVC of JJ and present results of detailed investigation of the rc-branch.

Let us consider the system, presented in Fig.1. In normalized units the system of equations, describing this electric scheme taking into account the external electromagnetic radiation, can be written in the form [9]

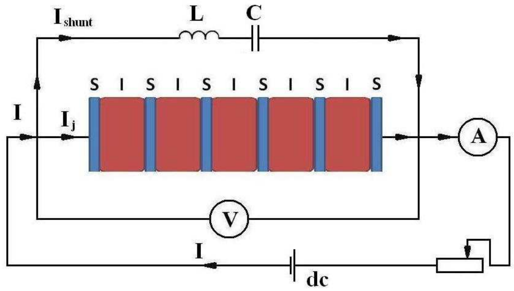

Fig. 1: *Schema of the JJ with LC shunting elements*

$$\begin{cases} \dfrac{\partial \varphi}{\partial t} = V \\ \dfrac{\partial V}{\partial t} = I - \sin\varphi - \beta\dfrac{\partial \varphi}{\partial t} - C\dfrac{\partial u_c}{\partial t} + A\sin\omega t \\ \dfrac{\partial^2 u_c}{\partial t^2} = \dfrac{1}{LC}(V - u_c) \end{cases} \quad (1)$$

Here u_c is the voltage at the capacitance. The bias current I is normalized to the critical current I_c of JJ, time normalized to the inverse plasma frequency $\omega_p = \sqrt{2eI_c/\hbar C}$,voltages V and u_c normalized to $V_0 = \hbar\omega_p/2e$; shunt capacitance C to the capacitance of the JJ

C_j, and shunt inductance L to $\left(C_j\omega_p^2\right)^{-1}$. In the system of equations (1) we introduce a dissipation parameter $\beta = (1/R_j)\sqrt{\hbar/2eI_cC_j} = 1/\sqrt{\beta_c}$ with β_c

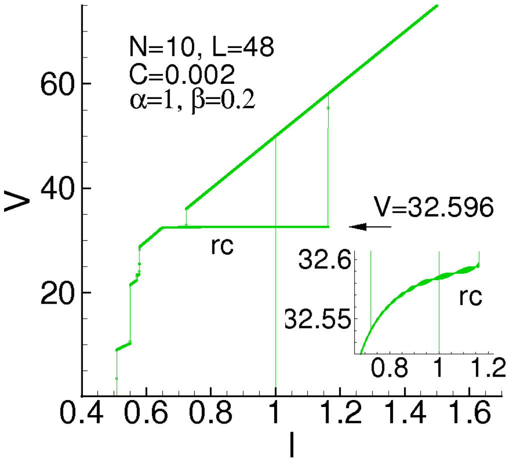

Fig. 2: *CVC of the stack with 10 JJ. Inset enlarges the end part of rc-branch demonstrating its small slope.*

as McCumber parameter. Amplitude A and frequency of external radiation ω normalized respectively to the critical current I_c and plasma frequency ω_p. Fig.2 shows the CVC of the stack with 10 JJ. We see a big rc-branch at V =32.596. Inset enlarges the end part of rc-branch demonstrating a small slope.

Fig.3 shows CVC of the stack with 10 JJ shunted by LC elements and under external radiation with frequency $\omega = 3.2596$ and amplitude A=0.2. Irradiation leads to the appearance of the Shapiro Steps on rc-branch and its subharmonics. Inset enlarges the end part of rc-branch demonstrating this Shapiro step of constant voltage on it. Irradiation of the stack changes Shapiro step behavior in comparison to steps on initial CVC without rc-branch.

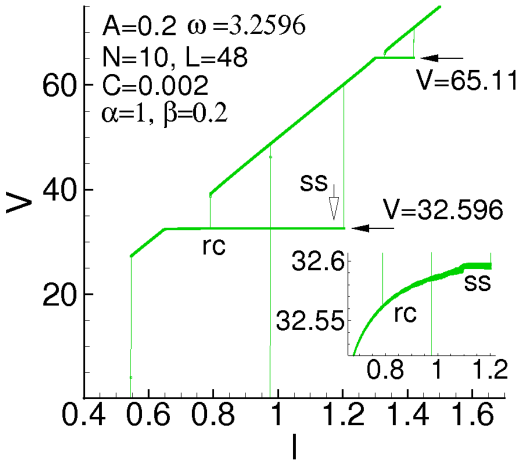

Fig. 3: *CVC of the stack with 10 JJ under external radiation with frequency = 3.2596 and amplitude A = 0.2. Inset enlarges the end part of rc-branch demonstrating Shapiro step on it.*

We studied the resonance features of JJ shunted by LC-elements under electromagnetic irradiation. A strong effect of the external radiation on the CVC is demonstrated. A crucial change in CVC found at the double resonance condition when radiation frequency coincides with Josephson and resonance circuit frequencies.

References

[1] K. K. Likharev, Dynamics of Josephson junctions and Circuits, New York, Gordon and Breach, (1986).

[2] A. N. Grib, P. Seidel, and J. Scherbel, Phys. Rev. B **65**, 094508 (2002).

[3] M. V. Fistul, Phys. Rev. B 75, 014502 (2007).

[4] H. D. Jensen, A. Larsen,J. Mygind, PhysicaB, 165, 1661(1990)

[5] A. Larsen, H. D. Jensen, J. Mygind, Phys. Rev. B **43**, 10179 (1991).

[6] M. Tachiki, K. Ivanovic, K. Kadowaki and T. Koyama, Phys. Rev. B 83, 014508 (2011).

[7] T. Zhou, J. Mao, H. Cui, X. Zhao, L. Fang and S. Yan, Physica C **469**, 785 (2009).

[8] E. Almaas and D. Stroud, Phys. Rev. B **65**, 134502 (2002).

[9] Yu. M. Shukrinov, I. R. Rahmonov, K. Kulikov, JETP Letters, **96**, 657 (2012).

Subgap peculiarities in asymmetric superconducting high-transparency junctions: the case of two-band/two-gap magnesium diboride

Vladimir Tarenkov[1]*, Mikhail Belogolovskii*[1]*, Sebastian Döring,*
Stefan Schmidt, and Paul Seidel

[1] *Donetsk Institute for Physics and Engineering, 83114, Donetsk, Ukraine*

In spite of tremendous progress in our knowledge about Fe-based superconductors, some basic findings still remain unsolved. Similar measurements on other materials, which are better characterized, can be very helpful in the effort to answer the open questions. In particular, it relates the presence of an enormous number of peculiarities in the Andreev-spectroscopy data for superconducting (S) break junctions with a constriction (c) [1,2].

To follow this idea, we have studied charge transport characteristics of ScS junctions based on superconducting MgB_2 with T_c about 39 K whose electronic characteristics in an S-state are well known. In MgB_2, four Fermi surface sheets are grouped into quasi-two-dimensional σ-bands and three-dimensional π-bands and, hence, their properties can be described by an effective two-band model with energy gaps $\Delta_\sigma = 7.1$ meV and $\Delta_\pi = 2.7$ meV [3,4].

In superconducting ScS samples with identical single-gap superconductors a strong subgap current has long being associated with subharmonic gap structure, features in the *I-V* characteristics at voltages $2\Delta/(ne)$, where Δ is the superconducting gap and n is an integer [5]. This effect was explained as a result of multiple Andreev reflections inside the interelectrode spatial gap [5]. In such processes an incoming electron at energy E undergoes at least n-1 Andreev scatterings to finally reach an empty state at energy $E+neV$. The probability of such events transmitting a charge ne from one superconducting bank to another is proportional to D^n. Thus the effect vanishes for tunnel junctions and can be observed only for the transparency $D \leq 1$.

In S_1cS_2 junctions with dissimilar superconductors the situation becomes much more complicated due to the appearance of new possibilities for the subgap current [6]. It is illustrated in Fig. 1 where we compare (a) a well-known single-particle process at $V \geq (\Delta_1 + \Delta_2)/e$ when the applied voltage stimulates a Cooper pair from the superconductor 1 to decay into a single electron in the lowest state of 1 and an electron in the lowest state of 2, and (b) a transmission process at $V \geq (\Delta_2 - \Delta_1)/e$ involving two Cooper pairs from both sides of the junction. Due to the extremely large density of quasiparticle states at the gap edge, the current sets in very steeply at corresponding voltages.

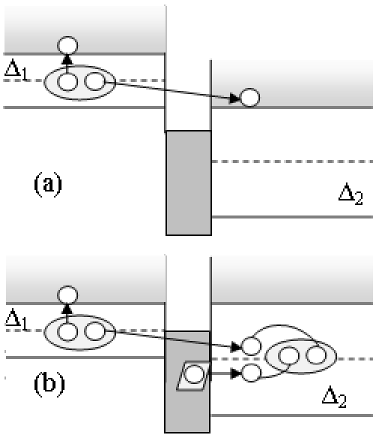

Fig. 1: *Schematic of the charge transferring processes in a ScS junction with threshold biases* $V \geq (\Delta_1 + \Delta_2)/e$ *(a) and* $V \geq (\Delta_2 - \Delta_1)/e$ *(b), the temperature T = 0.*

In our experiments, the Ag tip was indented into polycrystalline MgB_2 samples in order to form junctions between different MgB_2 grains inside the superconducting bulk of the material. Differential conductance dI/dV-versus-V curves were recorded using standard lock-in technique with a small ac modulation of 10 μV superimposed on a slowly varying voltage bias applied to the sample. In some cases the dynamic conductance was determined through numerical differentiation.

Several tens of junctions have been studied at 4.2 K. Most of them demonstrated standard Andreev-reflection spectra with a doubled conductance at $V = 0$ up to $V \approx 2\Delta_\pi / e$. But a small amount of the devices (a few percents) exhibited very reach structure at different voltage biases. A typical example of such dI/dV-vs-V characteristics is shown in Fig. 2.

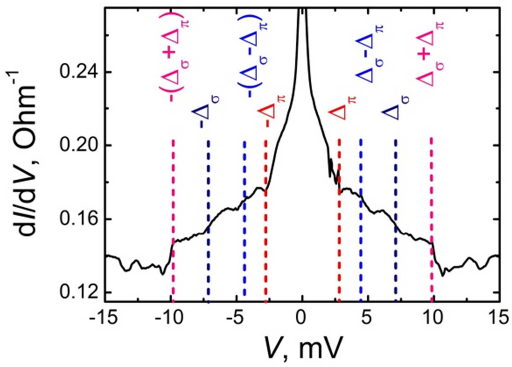

Fig. 2: *The subgap fine structure in the differential conductance spectra of MgB_2 junctions formed by pressing Ag tip into a polycrystalline magnesium diboride bulk; T = 4.2 K. Positions of the main singularities are shown by dashed lines.*

In Fig. 2 we compare the fine structure revealed in the differential conductance spectra with theoretical expectations. First of all, we attract attention to prominent features at $V = \pm(\Delta_\sigma + \Delta_\pi)/e$ which is not expected for a contact of a normal metal and the superconductor. Thus, we can conclude that indeed we are dealing with a $S_\sigma cS_\pi$ heterostructure within the MgB_2 bulk and it is the origin of the sum-of-gaps feature shown schematically in Fig. 1a. Other nonlinearities are not as pronounced since they do not involve two gap-edge singularities but only one of them. In any case, they occur at voltages near those expected for asymmetric superconducting junctions (in particular, it relates the difference-of-gaps feature). It should be emphasized that the gap values shown in Fig. 2 are only averaged ones and the two-band/two-gap approximation ignores significant anisotropy of the superconducting order parameter in MgB_2 [4]. Taking it into account, the agreement between theory and experiment should be regarded as reasonable.

Let us compare our approach with the study of asymmetric Nb-based junctions [6]. The authors attached a Nb microcrystal on the apex of the STM tip and produced asymmetric junctions between Nb single crystal with well characterized parameters and a Nb microcrystal with an initially unknown Δ (but definitely reduced comparing to the Nb bulk). On the contrary, we have interpreted a subgap structure using only well known gap values for MgB_2 [3,4]. In the strongly asymmetric MgB_2 junctions we have revealed numerous number of unexpected features which cannot be seen in conventional symmetric ScS junctions

References

[1] T.E. Shanygina *et al.* J. Phys.: Conf. Ser. **391**, 012138 (2013).

[2] Y.G. Ponomarev *et al.* J. Supercond. Nov. Magn. **26**, 2867 (2013).

[3] A.Y. Liu, I.I. Mazin, and J. Kortus, Phys. Rev. Lett. **87**, 087005 (2001).

[4] H.J. Choi *et al.* Nature **418**, 758 (2002).

[5] T.M. Klapwijk, G.E. Blonder, and M. Tinkham, Physica B+C **109-110**, 1657 (1982).

[6] M. Ternes *et al.* Phys. Rev. B **74**, 132501 (2006).

Optical analysis of thin films coated by CCVD

Ivo Zunke[1], Daniel Lehmann[2], Andreas Heft[1], Bernd Grünler[1], Dietrich RT Zahn[2], Paul Seidel

[1] *Innovent e.V., Prüssingstr. 27B, 07745 Jena*
[2] *TU Chemnitz, Semiconductor Physics, Reichenhainer Straße 70, 09126 Chemnitz*

For surface characterization and assessment particularly optical analytical methods are suited. They work contactless and nondestructive and because of their rapid performance they are also suitable for in-line monitoring of production processes. One powerful optical method represents the spectroscopic ellipsometry. Layer thicknesses, refractive indices and absorption spectra of complex coating systems can simultaneously be detected. However, a particular difficulty depicts the description of surfaces with high roughness.

The evaluation of the measured ellipsometry data requires the generation of a computer model of the examined coating system. The parameters of this model, the optical constants and layer thicknesses, are varied until the model matches the measured data. For the description of surface roughness the effective medium approximation (EMA) with a homogeneous, smooth layer is typically assumed and the optical constants are reduced to 50% of the bulk material (Fig. 1, a). This merely is a very imprecise description when a high surface roughness is present.

The improvement of the roughness model is performed by incorporating the natural growth process into the optical description of the roughness [1]. This results in a mountain-valley character of the real layer instead of a homogeneous roughness layer. Thus nearly 100% of the film (bulk) material is present at the interface roughness-to-bulk. In the other direction only the peaks of the film material (roughness) contribute to the model. According to this a profile of the optical constants results within the roughness layer, which is schematically shown in Fig. 1, b.

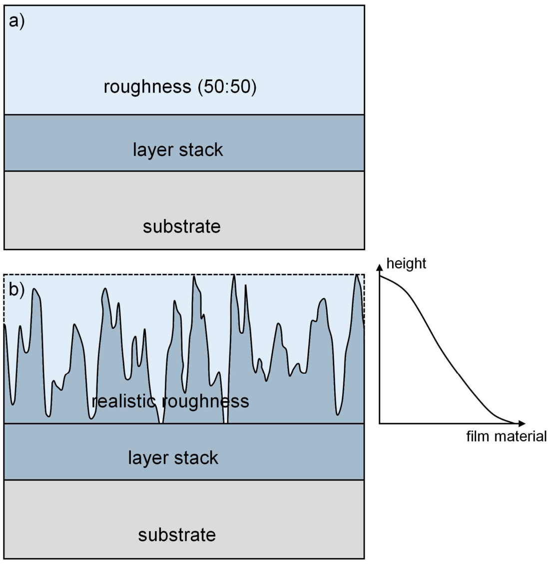

Fig. 1: *Conventional ellipsometry model (a) in comparision with the improved model (b) for characterizing the roughness.*

ZnO thin films were coated by combustion CVD (CCVD) [2] onto silicon substrates. A series of different burner passes was prepared. A correlation between the film thickness and the electrical conductivity should be pointed out [3].

The film thickness was measured by a tactile profilometer and is compared to the ellipsometric calculated thickness using the described model (Fig. 2). The determined layer thicknesses of both techniques (ellipsometry: bulk material + roughness) are in good agreement. This shows the high quality of the ellipsometry model.

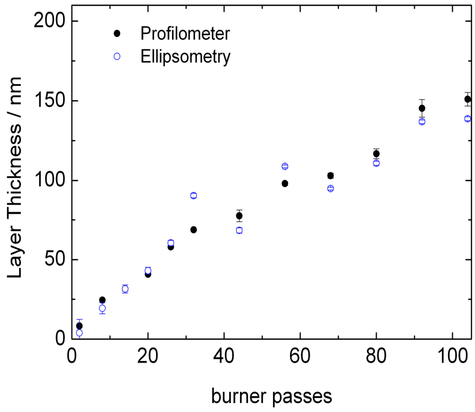

Fig. 2: Calculated layer thicknesses of the different methods: profilometry and ellipsometry.

The big advantage of the chosen model is to distinguish between bulk material and roughness on the basis of the thin film growth. This makes it possible to follow the development of these two components separately (Fig. 3).

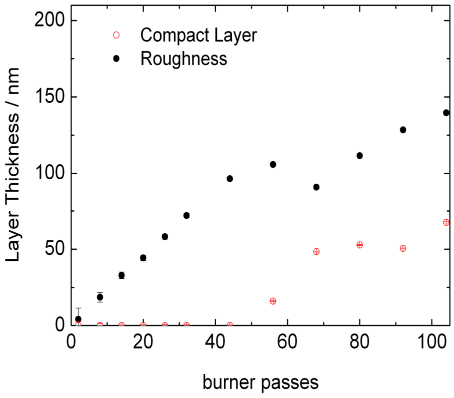

Fig. 3: Concerning the layer thickness, roughness and bulk material can be separated by means of the ellipsometry model.

Following the increasing roughness and starting with the first passes only a statistically adsorption of particles indicates an initial island growth. A continuous layer begins to form at around 50 burner passes. For electrically conductive thin films a contact of the islands, ideally a continuous layer, is essential. So below 50 passes no conductivity should be measured. In fact, using electrical four-point measurements conductivity is demonstrated starting from the 50th burner pass.

Calculating the specific resistivity by using the profilemtric thickness leads to an overestimation due to the fact that the profilometer can not separate roughness and bulk material. So the non contributing fraction 'roughness' has to be removed. Only the result of the ellipsometric study leads to the correct value of the real specific resistivity.

The presented ellipsometry model gives a better description of the roughness of a layer, but also optimizes the overall description of the layer system. The parameters, such as the layer thickness of the underlying roughness, are hidden for the most techniques and can be determined precisely.

Acknowledgement

The main author acknowledges the support of the Federal Ministry of Economics and Energy (BMWi) (VF090055) and highlights the productive cooperation with D.R.T. Zahn and his workgroup at the University of Chemnitz. Special thanks go to D. Lehmann.

References

[1] D. Lehmann *et al.*, 9. ThGOT Tagungsband, 125-128 (2013).
[2] I. Zunke *et al.*, Thin Solid Films **532**, 50-55 (2013).
[3] I. Zunke, Dissertation, FSU Jena, 2014, *submitted*.

The nature of interstellar PAH molecules

Cornelia Jäger, Gaël Rouillé, Friedrich Huisken, and Thomas Henning

Mathias Steglich, University of Basel

Polycyclic aromatic hydrocarbons (PAHs) represent an important group of cosmic-relevant organic molecules. Their existence in several astrophysical environments, ranging from planetary nebulae, reflection nebulae, circumstellar disks, active galactic nuclei, even to the interstellar medium (ISM) has been inferred from the presence of infrared emission bands related to C–H and C–C vibrational modes. It was found that PAH mixtures can contribute to or be entirely responsible for the interstellar ultraviolet bump at 217.5 nm. [1]. Because of their regular structure, PAHs show similar IR emission features. The superimposition of these features results in a collective spectrum that cannot be used to identify individual PAHs. Bands around 3.3 and 3.4 μm were found in IR emission/absorption sources, which are generally attributed to aromatic or aliphatic CH stretching vibrations in in normal or substituted PAHs, respectively.

In a recent study [2], IR absorption spectra of individual PAHs containing methyl, methylene, or diamond-like groups and IR spectra of mixtures of methylated and hydrogenated PAHs prepared by gas-phase condensation were measured at room temperature and at low temperature isolated in Ne matrices. The PAH blends were subjected to an extensive structural analysis of their functional groups by NMR and matrix-assisted laser desorption and ionization mass spectrometry. Supported by calculations at the density functional theory level, the laboratory results were applied to analyze the aliphatic absorption complex of the diffuse ISM at 3.4 μm and to determine the abundances of hydrocarbon functional groups carried by PAHs. By comparing the absorption cross sections we obtained with astronomical observations, we derived the abundance of the three groups ($-CH_3$, $>CH_2$, and $>CH-$). Each has an abundance of 1×10^{-5}–2×10^{-5} compared to that of H atoms. This value is valid for PAHs that are contained in grains. If a large population is in the gas phase, the value is reduced two to four times. Finally, the abundance of the aromatic $=CH-$ groups varies greatly depending on the line-of-sight. They are nearly absent or almost as abundant as either aliphatic group [2].

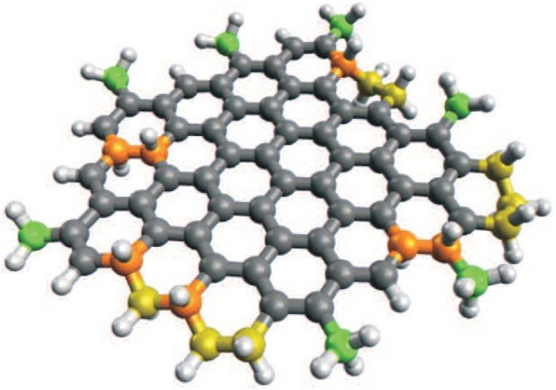

Fig. 1: *Synthetic structure showing the relative interstellar abundances we derived for different functional groups. Carbon atoms colored in green: methyl groups; in yellow: methanediyl groups; in orange: methanetriyl groups.*

In order to account for the whole UV bump strength, $N_C/N_H = (9 \pm 3) \times 10^{-5}$ carbon atoms have to be locked up in interstellar PAHs containing 50–60 C atoms [1]. If we compare this value with the previous estimates, we find that $N_C/N_{CH2+CH3}$=3.3±2.7, which is compatible with a large PAH (about 50–60 aromatic C atoms) with excess hydrogens and methyl groups on its periphery. Figure 1 shows the inferred average molecular structure, which, along with an almost unlimited number of variations, could be present in the diffuse ISM, either as free-flying unit or locked-up and interlinked in larger clusters or grains.

The study of interstellar PAHs is also linked to the question of the nature of the diffuse interstellar bands (DIBs). More than 400 DIBs between 400 and 2000 nm, have been detected so far. Surprisingly, although it is widely thought that the carriers of the DIBs are gas-phase interstellar molecules, not a single of these carriers has been definitely identified. Because PAH molecules can give rise to absorption bands at such wavelengths, especially large ones and cations, they have been proposed as candidates for the carriers of the DIBs.

We have examined the possibility for PAHs to be carriers of DIBs [3,4]. After studying the absorption spectra of several species, and measuring a number of them in the laboratory, we have come to the conclusion that normal PAHs are not carriers of the stronger DIBs. Two arguments stand out: First, the number of possible PAH structures is virtually infinite while that of strong DIBs is a few tens. Second, the spectrum of a PAH is in general dominated by bands in the UV region while DIBs are absent from this wavelength domain. The PAH hypothesis, however, is not to be discarded.

It has to be realized that, in the ISM, PAH molecules participate in various chemical processes. For instance, they can be ionized by the interstellar UV photon flux; they can also react with radicals, such as ethynyl (C_2H), which is one of the most abundant molecules in the ISM. Thus a whole population of the interstellar PAHs would consist of modified species.

Consequently we have proposed that PAHs can be carriers of DIBs provided that they are modified. The modification must: (i) be consistent with interstellar chemistry so that the DIB-carrying PAHs can be produced in the ISM; (ii) result in an enhanced photostability so as to yield large populations that can be detected; and (iii) produce PAH spectra dominated by bands at visible and near IR wavelengths so as to comply with the DIB spectrum.

We have found that these conditions can be linked: Interstellar chemistry can be expected to produce PAHs carrying side groups, which increase the photostability of the molecules by allowing a very fast internal redistribution of the excitation energy. This fast mechanism causes the broadening of the UV bands and the lowering of their peak intensity making them difficult to detect and resulting in a PAH spectrum dominated by bands in the visible domain. Thus PAHs that carry side groups, or substituted PAHs, are better candidates for the DIB carriers than normal PAHs.

References

[1] M. Steglich *et al.Astrophys. J. Lett.* **712,** L16-L20, (2010).

[2] M. Steglich *et al.*, *Astrophys. J. Suppl. Ser.* **208**, 26 (2013).

[3] F. Huisken *et al.*, *Proc. Int. Astron. Union* **9** (S297), in press (2013).

[4] G. Rouillé *et al.*, *Proc. Int. Astron. Union* **9** (S297), in press (2013).

Gas-phase condensation and processing of interstellar dust analogs in the interstellar medium

Tolou Sabri, Cornelia Jäger, Thomas Henning

Lisseth Gavilan, Jean-Louis Lemaire, Gianfranco Vidali
Observatoire de Paris/Universit´e de Cergy-Pontoise

Major amounts of cosmic dust are formed via gas-phase condensation in the winds of asymptotic giant branch (AGB) stars. Eventually, the dust is ejected into the interstellar medium where it will be partly destroyed, recondensed and finally incorporated into interstellar clouds. Silicates are a major component of dust mostly found as amorphous silicates with pyroxene ($M_2Si_2O_6$) or olivine (M_2SiO_4) stoichiometry, where M indicates the metal cation with Mg and Fe being the most abundant. Crystalline silicates in the form of forsterite (Mg_2SiO_4) and enstatite ($MgSiO_3$) have been detected in different astrophysical environments [1].

In a joint research project with the Laboratory Astrochemistry Group at the Observatoire de Paris, realistic silicate dust analogs with defined morphology have been prepared that has finally been used as real surfaces for studying the H_2 molecule formation in the ISM [2,3].

In our laboratory, the condensation of nanometer-sized silicate dust grains has been performed by laser ablation of bulk silicates or mixed metal targets (Mg, Fe, and Si) in He or He/O_2 quenching gas atmosphere, respectively. This method allows us to prepare amorphous silicates of different compositions. A beam of the freshly condensed nanometer-sized particles can be produced via supersonic extraction through a nozzle and a skimmer and finally directed to a substrate for the formation of a particle film. Amorphous Mg_2SiO_4 and Fe_2SiO_4 grains, as well as the corresponding crystalline silicates, forsterite and fayalite, were synthesized. The latter were produced by thermal annealing of the amorphous condensates in controlled atmospheres. The structure and morphology of the produced samples have been characterized and monitored by efficient analytical and imaging techniques. In contrast to former gas-phase condensation studies of silicates [4], the structural and compositional characterization of the condensed grains clearly revealed the formation of amorphous and homogeneously composed, nanometer-sized silicate grains with the typical spectra showing the broad 10 and 20 µm bands of amorphous silicates (see Fig. 1). The spectra of the amorphous samples are in very good agreement to the spectral properties of interstellar silicates [5].

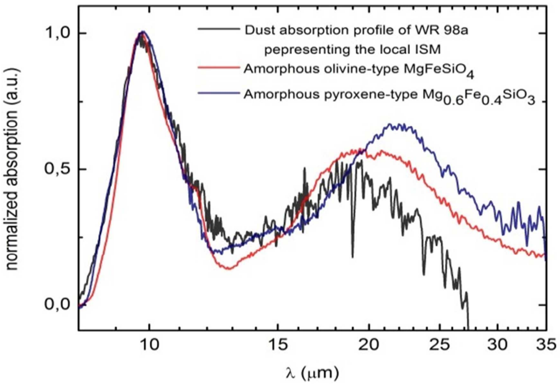

Fig. 1: *IR spectrum of amorphous silicates compared to dust absorption profile of WR98a [5].*

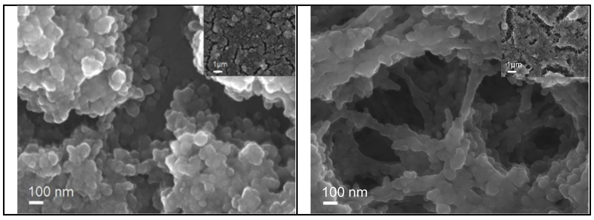

Fig. 2 *FESEM image of the deposited amorphous (left) and crystalline (right)* Mg_2SiO_4 *grains[2,3].*

The formation of molecular hydrogen on different dust surfaces has been studied in an apparatus mainly consisting of a UHV chamber (pressure $<10^{-10}$ mbar). The samples were cooled down to 5 K and irradiated either by a pure molecular hydrogen beam or by an atomic beam with a small, non-dissociated fraction. The setup is well described in [6] Two spectroscopic diagnostics are used, first temperature programmed desorption (TPD) and 2+1 REMPI-TOF (Resonance Enhanced Multi-photon Ionization-Time of Flight). TPD is performed using a QMS.

The data revealed that the amorphous $FeSiO_4$ is a more effective surface for the recombination of D_2 compared to its crystalline counterpart (Fig. 3). In addition, the surface of a grain affects the energy of the newly formed H_2 molecules. Rotational state abundances of the molecules formed and ejected, or just scattered from the different surfaces, were mapped. This showed a rotational cooling of molecules that collided on crystalline dust surfaces. It was interpreted as the blocking of specific rotational degrees of freedom when molecules collide with flatter surfaces.

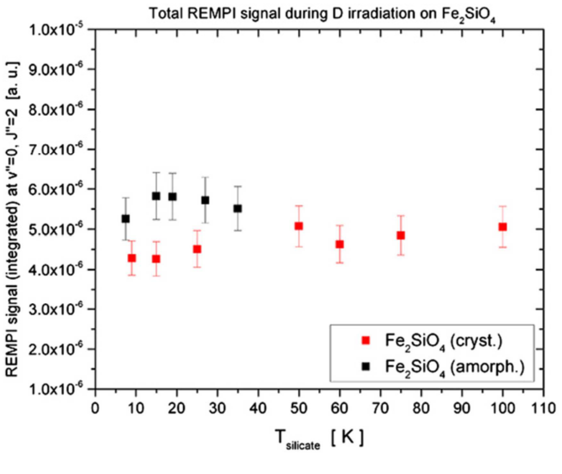

Fig. 3 *Formation efficiency of D_2 after interaction on Fe_2SiO_4 detected by the REMPI from v'' = 0, J'' = 2. [3]*

This characteristic was confirmed by atomic force (AFM) and field-emission scanning electron microscopy (FESEM) analysis of the surfaces. Figures 3 and 4 show 3D images of Mg_2SiO_4, which demonstrate that the shallow valleys transform into valleys with sharper or steeper slopes. Both crystalline silicates produce rotationally cooled molecules, suggesting that rotational cooling may be a kinematic effect most likely produced both by the flatter single grain geometry on these surfaces, and by the presence of bridges between clusters, which effectively affects the translation-rotation coupling of the incoming and/or newly-formed molecules. Effectively, rounder grains will allow the "cartwheel mode to keep rolling" thus leaving the rotational temperature of D_2 scattered on amorphous grains unchanged, while the flatter grain walls will facilitate rotational energy loss.

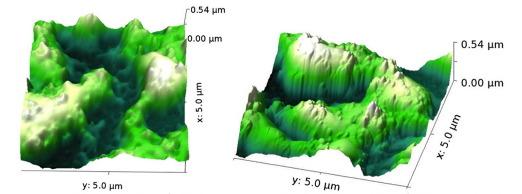

Mg_2SiO_4 am. (5 μm^2, 540 nm deep) Mg_2SiO_4 crystal. (5 μm^2, 540 nm deep)

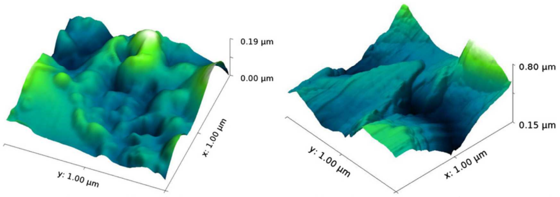

Mg_2SiO_4 am. (1 μm^2, 200 nm deep) Mg_2SiO_4 crystal. (1 μm^2, 650 nm deep)

Fig. 4 *AFM images of Mg_2SiO_4 in 3D showing the amorphous dust grains (left) and crystallized dust grains (right). [2,3]*

Experimental simulation of fundamental gas–grain interactions offers key information on the rotational structure of ejected molecules. Rotationally excited and/or rotationally cool species play a important role in the chemical networks in space.

References

[1] T. Henning, ARA&A, **48**, 21 (2010).
[2] T. Sabri *et al.*, *ApJ*,**780**, 180S (2014).
[3] L. Gavilan *et al.*, *ApJ*, **781**, 79G (2014).
[4] F. Rietmeijer *et al.*, *Chem. Mater.*, **3**, 692R (1999).
[5] J. Chiar *et al. ApJ*, **637**, 774R (2006).
[6] Lemaire *et al. ApJL*, **725**, L156 (2010)

Removal of step-edges in SQUID-based geomagnetic data

Thomas Schönau

M. Schneider, M. Schiffler, M. Schmelz, R. Stolz and H.-G. Meyer
Leibniz-Institute of Photonic Technology, PO Box 100239, D-07702 Jena, Germany

Since Superconducting Quantum Interference Devices (SQUIDs) exhibit a sinusoidal-like output characteristic with a periodicity of one flux quantum Φ_0, they are commonly operated in a special feedback circuit, called flux locked loop (FLL), in order to linearize their output characteristic. In the case of unshielded measurements, magnetic transients can exceed the slew rate of the FLL and force it to change its operating point. Furthermore, some FLL configurations automatically reset the operating point to enhance the dynamic range, resulting in a large amount of step-like shifts of the output voltage as depicted in figure 1a) and 1b). A reliable recognition and removal of step-edges is therefore necessary before SQUID-based data can be interpreted.

A reconstruction based on a simple shift of each interval in figure 1a) to the appropriate level exhibits spikes like in figure 1c) and 1d), which originate in the step response of the A/D converter. Since the shape of the step response depends on the sub-sample time difference between step-edge occurrence and the sampling events, the spikes differ from each other. In order to obtain a smooth reconstruction, we developed software that calculates these shape variations from a sampled step-edge response by appropriate manipulations of phases in Fourier domain. For each step-edge, the step response which fits best is determined by an optimization procedure and subtracted from the data. In figure 1c) and 1d), both reconstruction methods are compared. The better smoothness of the proposed method allows recovering the intrinsic noise spectrum of the measurement, which formerly was disturbed by the remaining spikes.

The implemented step-edge detector is based on the “undecimated wavelet transform” which allows to analyze and to correlate the signal on different timescales. Since a wavelet that has p vanishing moments is orthogonal to any polynomial of degree p-1, the edge detector strongly suppresses the smooth magnetic signal and produces significant outputs only around step-edge locations.

More details concerning the realization of the software and the obtained results can be found in [1].

The author likes to thank his supervisor Prof. Dr. Paul Seidel.

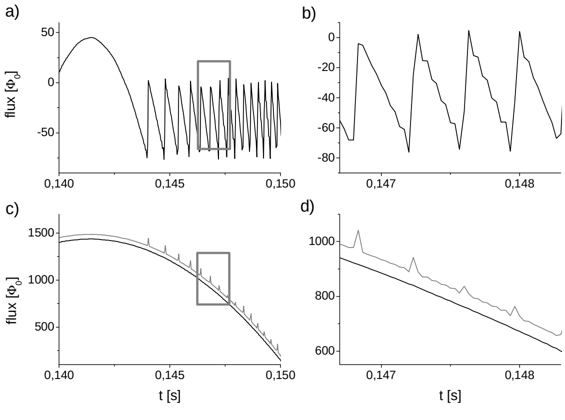

Fig. 1: *Subframes a) and b) show the acquired signal containing step-edges. The simple (grey) and proposed (black) reconstruction methods are depicted in c) and d). The offset between them is introduced for reasons of better illustration.*

References

[1] T. Schönau *et al.*, Meas. Sci. Technol. **24**, 125004 (2013).

3. Technical Reports and Equipment

Operation of the ion-accelerator JULIA and the ion-implanter ROMEO

U. Barth, P. Hoffmann, F. Jehn, C. Ronning

The 3 MV high current tandetron accelerator **JULIA** (***J**ena **U**niversity **L**aboratory for **I**on **A**cceleration*) went in operation end of 1996. Since the beginning of the routine-operation in 1997 it has been used for different types of experiments requiring a broad spectrum of ion-beams. With the exception of helium, where the duoplasmatron ion-source followed by a lithium exchange channel was used, all ions were extracted from a sputter-type ion-source. The beam-on-target-time of 1850 h was about 30% higher than in 2012. The 400 kV ion-accelerator **ROMEO** is in routine operation since 1998, here the beam-on-target-time of 1270 h was in the same order of magnitude as in the preceding years.

Both accelerators can be operated separately or in combination. The ion-beams produced until 2013 are summarized in table 1. The ion-beam currents quoted are typical values of the ion source currents used for the experiments, the maximum currents available are significantly higher for most ions.

Period	Element	Julia	Romeo
1	Hydrogen (H)	1 µA	4 µA
	Helium (He)	0,1 µA	4 µA
2	Lithium (Li)	2 µA	1 µA
	Boron (B)	0,1 µA	5 µA
	Carbon (C)	3 µA	1 µA
	Nitrogen (N)	0,4 µA	4 µA
	Oxygen (O)	2 µA	2 µA
	Flourine (F)	-	2 µA
	Neon (Ne)	-	5 µA
3	Sodium (Na)	-	6 µA
	Magnesium (Mg)	-	5 µA
	Aluminium (Al)	-	4 µA
	Silicon (Si)	16 µA	4 µA
	Phosphorus (P)	1 µA	4 µA
	Sulfur (S)	1 µA	-
	Chlorine (Cl)	-	2 µA
	Argon (Ar)	-	20 µA
4	Potassium (K)	-	3 µA
	Calcium (Ca)	-	5 µA
	Titanium (Ti)	0,7 µA	-
	Vanadium (V)	0,2 µA	1 µA
	Manganese (Mn)	0,02 µA	5 µA
	Chromium (Cr)	0,2 µA	3 µA
	Iron (^{56}Fe)	0,8 µA	2 µA
	Iron (^{57}Fe)		0,015 µA
	Cobalt (Co)	-	3 µA
	Nickel (Ni)	-	6 µA
	Copper (Cu)	0,5 µA	1 µA
	Zinc (Zn)	0,05 µA	6 µA
	Gallium (Ga)	-	3 µA
	Germanium (Ge)	1,6 µA	4 µA
	Arsenic (As)	0,4 µA	1 µA
	Selenium (Se)	0,5 µA	1,5 µA
	Bromine (Br)	10 µA	8 µA
	Krypton (Kr)	-	10 µA
5	Rubidium (Rb)	0,07 µA	1 µA
	Strontium (Sr)	-	3 µA
	Yttrium (Y)	-	4 µA
	Zirconium (Zr)	0,3 µA	1,5 µA
	Rhodium (Rh)	0,2 µA	-
	Palladium (Pd)	0,09 µA	1 µA
	Silver (Ag)	1,6 µA	10 µA
	Cadmium (Cd)	-	0,8 µA
	Indium (In)	0,5 µA	8 µA
	Tin (Sn)	1,0 µA	3 µA
	Antimony (Sb)	0,6 µA	4 µA
	Tellurium (Te)	-	2 µA
	Iodine (I)	3 µA	-
	Xenon (Xe)	-	10 µA
6	Caesium (Cs)	-	4 µA
	Barium (Ba)	-	1 µA
	Praseodymium (Pr)	-	1 µA
	Neodymium (Nd)	-	0,5 µA
	Samarium (Sm)	0,01 µA	1,5 µA
	Europium (Eu)	0,03 µA	2 µA
	Erbium (Er)	0,04 µA	2µA
	Tantalum (Ta)	0,2 µA	2 µA
	Tungsten (W)	0,3 µA	0,01µA
	Osmium (Os)	0,05 µA	-
	Iridium (Ir)	0,3 µA	6 µA
	Platinum (Pt)	0,2 µA	-
	Gold (Au)	2,8 µA	20µA
	Lead (Pb)	0,03 µA	15µA
	Bismuth (Bi)	-	3µA

Table 1: Ion-beams accelerated until 2013. The currents given are measured at the Q-Snout-Faraday-cup after the low-energy mass separator (JULIA) and at the target position (ROMEO), respectively.

As in the preceding years the ion-beam facility was used by external research groups:

3MV-Tandetron „JULIA”

ITN Lissabon, Portugal, Dr. Lorenz
University of Oslo, Norwegen, Dr. Azorov
Uni Oldenburg, A. Neumüller
HZ Berlin für Materialien und Energie, Dr. A. Juma
HZ Berlin für Materialien und Energie, Dr. K. Elmer
Bergakademie Freiberg, S. Rentrop
NamLab gGmbH, Dresden, H. Wylezich
Firma Layertec, Mellingen, H. Heyer
Fachhochschule Jena, Prof. Rüb
IPHT, Jena, Dr. Diegel
University Jena

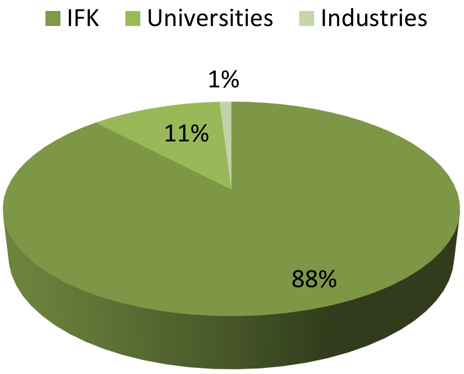

400kV Implanter „ROMEO“

Harvard University, USA, Prof. M. Loncar
University of Conneticut, USA, Prof. Puxian Gao
iThemba Labs, Kapstadt-Südafrika, Prof. K. Bharuth-Ram
University of Pretoria, Südafrika, Prof. Malherbe
University Minsk, Weißrussland, Prof. Kamerow
ITN Lissabon, Portugal, Dr. Lorenz
University of Oslo, Norwegen, Dr. Azorov
IAP, Jena, Dr. F. Schrempel
University Jena

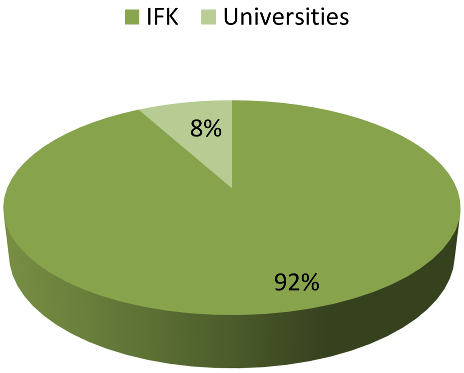

Cryogenic Services (TTS) 2013

All in-house customers of cryogenic liquids, which are all faculties of natural sciences, the university medical division including several hospitals, and other external scientific institutes (e.g. Institute for Photonic Technology Jena, Leibnitz Institute Hans-Knöll Jena) as well as some private customers like the Innovent e.V. Jena and some medical practices, were provided with liquid helium (LHe), with high purity gases (He, N_2), and with liquid nitrogen (LN_2) by the Cryogenic Services. Roughly 117,000 litres of LN_2 were delivered by the cryogenic services in 2013. The total delivery has increased last year due to additional demands of inert gas in the IAAC-institute and the new installed ZAF site.

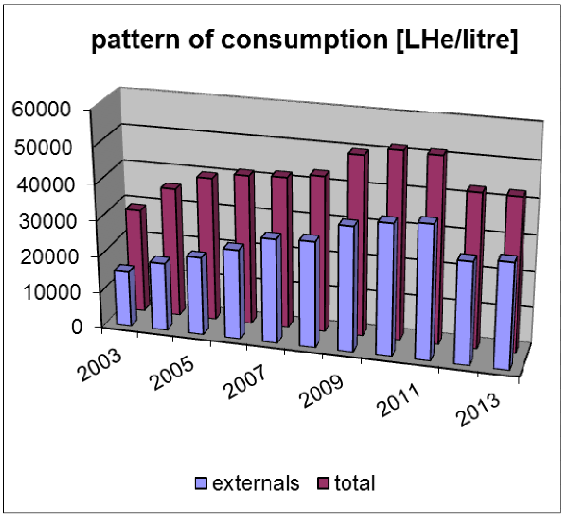

Fig. 1: Liquid helium output

As illustrated in Figure 1, the output of liquid helium (LHe) has levelled off in 2013. Merely 35,000 litres of LHe were delivered which calls for an annual gross refrigeration value of just 42,600 litres.

Last two years we had to face a worldwide shortage in helium supplies which leads generally to increased costs with considerable fluctuations of the fees over the year. On the crest of the wave the costs for short term LHe-orders have increased by a fivefold. In addition the long-term delivery contracts with fixed prices weren't fulfilled by the suppliers relating due to the delivered quantity. Therefore the financial weakness and supply shortfall have caused a strong reduction in LHe-use since 2012. Fortunately the relation between the produced quantity of LHe to the bought quantity was a good deal bigger than the years before 2012. This was possible due to the increased efforts of the LHe-users to decrease He-losses. In spite of the lower production rate the rising market prices increased the gross financial benefits of the internal helium liquefaction for all users noticeably.

The TTS-staff executed design, installation control and commissioning of two new pure argon storage tanks at the Helmholtzweg 4 site and the ZAF-site as well as the new inert gas logistics at the Lessingstraße 5.

The loading of heavy cargo in danger of tipping has been secured considerably by installing a penthouse roof over the open storage-area (Fig. 2).

Fig. 2: Adverse weather cover for the storage area of the He-gas transport units

Equipment

Preparation of Thin Films and Devices

- HV evaporation facilities for thermal and electron beam evaporation
- UHV evaporation facilities, including electron gun and in situ RHEED system
- Equipment for laser deposition of thin crystalline films and material systems, especially high temperature superconductors (KrF excimer laser, $\lambda = 248$ nm)
- Molecular Beam Epitaxy (MBE) facilities: MBE for silicon carbide (RIBER EVA 32 R&D)
- Organic Molecular Beam Epitaxy (OMBE) facilities including surface analysis techniques (MCP-LEED, UHV STM/AFM, RHEED) and *in situ* optical spectroscopy (PL and DRS)
- dc and rf sputtering systems for metallic (Au, Ti) and oxidic (SiO_2, Ta_2O_5) thin films and multilayers
- Ion beam etching with Ar ions at sample temperatures down to 80 K in vacuum
- Chamber for ion- and reactive etching up to 4” wafer
- Reactive ion beam etching with sample diameters up to 6 cm
- Ultrasonic wire bonder
- Equipment for photolithographic patterning
- MBE system NEBULA for $Cu(In,Ga)S_2$ layers on 4’’ substrates including RHEED setup
- Two HV systems for closed-space sublimation (CSS) for deposition of CdTe layers
- RF reactive sputtering system for transparent conducting oxides (TCO’s) and molybdenum
- DC sputtering system for copper and indium
- UHV system ULS400 for $Cu(In,Ga)(Se,S)_2$ on (100x100) mm^2 substrates
- Wet chemical processing and chemical bath deposition of photoactive layers

Surface Analysis Systems

- LT-STM/AFM (1 K) with QMS (1000 amu), MCP-LEED, DRS
- AUGER electron spectrometer
- Surface analysis systems SPECS and UNISPEC with XPS, UPS, AES, LEED, STM
- Atomic force microscopes (AFM and Microstructure Measuring Device VERITEKT 3 with needle sensor)
- Surface profilometer DEKTAK 100
- Scanning electron microscopes
- Several UHV-scanning probe devices (STM, AFM)

Electrical Measurement Techniques

- Electrical transport measurements (resistance, critical current density, point contact and tunneling spectroscopy)
- Hall-effect and Four-point probe equipment
- Current-voltage characteristics ($2 \text{ K} < T < 300 \text{ K}$, $B \leq 5$ T)
- Current-voltage characteristics by microwave irradiation ($2 \text{ GHz} < f < 300 \text{ GHz}$)
- Noise measurements (frequency range 60 µHz - 100 kHz) at low temperatures
- LTS-SQUID characterization at 4.2 K (current-voltage, flux-voltage, noise, screening properties)
- HTS-SQUID characterization up to 100 K (current-voltage, flux-voltage, noise)

- 2 Deep level transient fourier spectrometers (temperature range 80 K - 690 K, 30 K - 330 K)
- 3 Admittance spectrometers (frequency range 40 Hz - 100 kHz, 20 Hz - 2 MHz and 75 kHz - 30 MHz, temperature range 30 K - 690 K)
- Microwave signal generator (frequency range 1 - 20 GHz, resolution: 1 kHz)
- Electrical and optical characterization of high power diode laser arrays

Equipment for Optical Characterization

- UV-VIS spectrometer
- FTIR spectrometer
- Cathodoluminescence at SEM, equipped for IR - UV
- Micro-Photoluminescence, IR-UV, time-resolution ~ 1ns
- Photoluminescnce excitation (PLE)
- Optical cryostats (2…300 K) for optical absorption, photoluminescence and Raman spectroscopy
- Excitation lasers in a wide range from 405-1550 nm (fiber, gas, solid state and diode lasers)
- Optical microscopes
- Magnetrelaxation of ferrofluids (MORFF) for characterization of magnetic nanoparticles

Equipment for Electro-Optical (Solar) Characterization

- Solar simulator (AM 1.5) with Current-Voltage measurement
- Illumiated Current-Voltage measurements for 10 K to RT
- Quantum efficiency (EQE) measurements of solar cells

Equipment for Thermal Treatment

- Furnace for conventional thermal treatment in inert gas atmosphere or vacuum (temperatures up to 2050 K)
- RTA apparatus (double graphite strip heater) for short time annealing (annealing time in the order of seconds, temperature range 1000 K to 1950 K, temperature rise rate 100 K s^{-1})

Electron Microscopy

- Scanning electron microscope JEOL JSM-6490 with LaB_6-cathode
- FEI field-emission electron microscope connected with FIB system

Ion Beam Techniques

3 MV Tandetron accelerator "JULIA", equipped with

- Sputter ion source and Duoplasmatron source
- Universal beam line for ion implantation and ion beam analysis
- Second beam line for ion beam analysis, combined with implantation chamber of 400 kV implanter
- Irradiation chamber with cooled and heated sample holder and four axis goniometer

Application:

- Ion implantation: energy range 500 keV - 12 MeV, temperature range 15 K - 1500 K
- Ion beam analysis: RBS and PIXE in combination with channeling, ERDA, NRA

400 kV implanter “ROMEO”, equipped with

- Hot filament, hollow cathode ion source
- Irradiation chamber with cooled and heated sample holder and four axis goniometer, combined with beam line of 3 MV Tandetron accelerator

Application:

- Ion implantation: energy range 20 keV - 400 keV, temperature range 15 K - 1500 K
- Ion implantation at low temperatures and subsequent RBS analysis using H- or He-ions from 3 MV Tandetron accelerator

Low Energy implanter “LEILA”, equipped with

- Colutron Ion source 100-Q
- Colutron Ion Gun System G-2-D
- Irradiation chamber with heated sample holder

Application:

- Irradiation of surfaces: energy range sub-keV, temperature range 300 K - 750 K

Low Energy implanter “Mr. JIM Stringer”, equipped with

- Hot filament, hollow cathode ion source
- Irradiation and deposition chamber

Application:

- Deposition of diamond-like thin films: energy range 100eV – 30 keV, RT

Focused Ion Beam system FEI NanoLab Helios 600i

- Liquid ion source, E = 500 eV – 30 keV
- Electron microscope, E = 350 eV – 30 keV

Application:

- TEM-lamella preparaqtion, etc.

Low Temperature Measuring Equipment

- LT STM/AFM down to 1 K
- He-4 cryostats for temperatures down to 4.2 K
- He-4 refrigerator for the temperature range 1.3 K - 4.2 K
- Helium 3 refrigerator for temperatures range 4,2K - 300 mK with superconducting magnet to 2 T
- He-3/He-4 dilution refrigerator for temperatures range 4,2 K - 6 mK with superconducting magnet to 10 T
- He-3/He-4 dilution refrigerator with a base temperature of 35 mK
- Electronic equipment for characterization of cryoelectronic devices
- SQUID sensor systems for magnetic measurements under unshielded conditions
- SQUID sensor system for spatially resolved magnetorelaxometry
- Cryostats (2 K < T < 300 K; optical window; magnetic field)
- Cryocoolers (Gifford-McMahon and Stirling)
- Pulse tube refrigerators (for sensor cooling)

SQUID Application Laboratories

- Measurement system for non-destructive evaluation in unshielded environment based on high-T_C-SQUID gradiometers
- Magnet-Relaxation-Measuring System in unshielded environment for MRX and TMRX based on low-T_C SQUID gradiometers

Clean Room (Number of Particles/cu/t < 100)

- Photolithography
- Wet chemical etching
- dry chemical etching (Plasma etching machine “pico”, Diener Plasma)
- minimum lateral resolution: few micrometers

Shielded Rooms

- Faraday room
- Magnetic shielded room

Laboratory for Cryogenic Measurement of Mechanical Quality Factors of Gravitational Wave Detector Components

- room temperature stability of ± 0.2 K at best
- vibration isolation (decoupled foundation)
- acoustic isolation
- remote controlled operation of the measurement equipment
- separated room for disturbing machines (e.g. pumps)
- full supply of technical media to perform cryogenic measurements
- polishing tools for bulk samples

Laboratory for Astrophysics and Cluster Physics

- Supersonic jet apparatus for gas-phase spectroscopy of large molecules for gas-phase spectroscopy under astrophysical conditions covering the spectral range from UV to the NIR and LIF setup
- Matrix isolation UV/vis spectroscopy setup with closed-cycle cryostat
- Helium droplet apparatus for spectroscopy and reaction studies at ultra-low temperature
- Flow reactors for the production of silicon-, carbon-, and iron-based nanoparticles
- Cluster beam apparatus with laser pyrolysis source and size selection facility
- Time-of-flight mass spectrometer (TOF-MS)
- Quadrupole mass spectrometer
- Photoluminescence spectrometer for UV/vis and near IR emission wavelengths
- Atomic force microscope (AFM)
- High-pressure liquid chromatograph (HPLC) combined with DDA UV detector and fraction controller for analysis and preparative separation of pyrolysis condensates
- Pulsed and cw CO_2 lasers
- Single-mode Nd:YAG lasers with tunable dye lasers and frequency doubling facilities
- ArF excimer laser
- laser ablation setup for gas-phase condensation of nanoparticles combined with a particle beam extraction system and a closed-cycle cryostat for ice deposition and low-temperature applications
- FTIR spectrometer (Bruker)

4. Current Research Projects

(A) Supported by the Bundesministerium für Bildung, Wissenschaft, Forschung und Technologie (BMBF), Bundesministerium für Wirtschaft und Arbeit (BMWi), and Bundesministerium für Umwelt, Naturschutz und Reaktorsicherheit (BMU)

CdTe-CdS-Solarzellen hoher Effizienz für eine verbesserte Modul-Produktionstechnologie

Prof. Dr. W.Wesch	0329881A	09/08 – 06/13

Spitzenforschung und Innovation in den Neuen Ländern – PhoNa: Photonische Nanomaterialien

Prof. Dr. C. Ronning	PhoNa	12/09 – 11/14

Ioneninduzierte Strukturumbildungsprozesse in amorphen Halbleitern
Teilprojekt 4 im Verbundprojekt „Ioneninduzierte Strukturumbildung“
Verbund Forschung mit Sonden und Ionenstrahlen im Gesamtverbund Erforschung der kondensierten Materie mit Großgeräten

Prof. Dr. W. Wesch	05K10SJ1	07/10 – 08/13

Grenzflächen und Defekte – Rechnerunterstützte Optimierung des Wirkungsgrades von CIGS Dünnschichtsolarzellen in der industriellen Umsetzung
Teilvorhaben: Ermittlung von Struktur-Eigenschaftsbeziehungen und ihre Beeinflussung durch Variation der Prozessparamenter

Prof. Dr. C. Ronning	0325448E	08/12 – 07/15

Toxikologische Charakterisierung von Nanomaterialien für die diagnostische Bildgebung in der Medizin – NanoMed

Prof. Dr. P. Seidel	BMBF (Ausschreibung NanoCare)	09/10 – 08/13

Josephsonkontakte mit variablem Durchlassvermögen

Prof. Dr. P. Seidel	BMBF (WTZ UKR 10/034)	06/11 – 05/13

Resonance Features of Coupled Josephson Junctions with LCR-shunting under Radiation

Prof. Dr. P. Seidel, Dr. Yu. M. Shukrinov	BMBF(Heisenberg-Landau Prog.)	01/13 – 12/13

ET-R&D – Networking and R&D for the Einstein Telescope

Dr. R. Nawrodt	BMBF (05A13SJ1)	03/13 – 02/16

(B) Supported by the Deutsche Forschungsgemeinschaft (DFG)

Rastertunnelspektroskopie an einzelnen Molekülen in epitaktischen Nanoschichten

Prof. Dr. T. Fritz	FR 875/11-1	10/09 – 12/13

Optische Spektroskopie an ultradünnen Molekülschichten

Prof. Dr. T. Fritz	FR 875/9-3	02/12 – 02/15

Großgeräteantrag UHV-Analysesystem für XPS/UPS/AES

Prof. Dr. T. Fritz	INST 275/267-1	06/12 – 05/14

Formation and Shaping of Magnetic Nano-clusters in Ion Implanted Oxides

Prof. Dr. C. Ronning	Ro1198/13-1	03/11 – 02/15

Wiring quantum dots – phase separation inducing new functionlity (D-A-CH)

Prof. Dr. C. Ronning	Ro1198/14-1	08/11 – 07/14

Strukturierungsverfahren für mikro- und nanooptische Elemente in Lithiumniobat
Dr. E.-B. Kley, Prof. Dr. W. Wesch KL1199/2-2 05/10 – 12/13

Dynamics and Interactions of Semiconductor Nanowires for Optoelectronics (Coordination project)
Prof. Dr. Carsten Ronning RO1198/16-1 03/12 – 06/15

Light-matter interaction in optically doped nanowire LEDs and nano lasers (Teilprojekt P4)
Prof. Dr. Carsten Ronning RO1198/17-1 03/12 – 11/15

Gütemessungen bei kryogenen Temperaturen
(Teilprojekt C4 im SFB/TR 7 „Gravitationswellenastronomie“)
Prof. Dr. P. Seidel, Dr. R. Nawrodt DFG–SFB/TR7 01/03 – 12/14

Optische Eigenschaften siliziumbasierter Testmassen
(Teilprojekt C9 im SFB/TR 7 „Gravitationswellenastronomie“)
Dr. R. Nawrodt DFG–SFB/TR7 01/11 – 12/14

Josephson effects at iron pnictides
Prof. Dr. P. Seidel DFG (SPP 1458, SE 664/15-1) 05/10 – 09/13

Josephson effects at iron pnicides - phase-sensivitve experiments
Prof. Dr. P. Seidel DFG (SE 664/15-2) 10/13 – 09/16

Experimental and theoretical studies of charge transport in heterostructures based on two-band superconductros and/or ferromagnetic metals
Prof. Dr. P. Seidel DFG (SE 664/18-1) 11/13 – 10/14

Synthesis, processing, and spectroscopic characterization of PAHs with astrophysical impact
Prof. Dr. Fr. Huisken HU 474/21-2 07/10 – 06/13

Experimental studies of the low-temperature condensation of cosmic dust in the interstellar medium
Prof. Dr. Th. Henning HE 1935/26-1 02/12 – 01/15

Kohlenwasserstoff-Chemie bei ultratiefen Temperaturen in flüssigen Helium-Tröpfchen,
Prof. Dr. Fr. Huisken HU 474/22-3 05/12 – 05/15

(C) Support by the EU

Marie-Curie ITN network “Nanowiring”
Prof. Dr. C. Ronning 265073 11/10 – 10/14

IRON-SEA - Establishing the basic science and technology for Iron-based superconducting electronics applications
Prof. Dr. P. Seidel 283141 10/11 – 09/14

FP7-PEOPLE-IRSES Austauschprogramm für Wissenschaftler „ELiTES“
Dr. R. Nawrodt GA295153 03/12 – 02/16

ET R&D – Networking and R&D for the Einstein Telescope (3rd common ASPERA call)
Dr. R. Nawrodt ELiTES 03/13 – 02/16

Marie Curie ITN network “LASSIE- Laboratory Astrophysics Surface Science in Europe’’
Dr. C. Jäger 238258 02/10 – 01/14

Marie Curie Intra-European Fellowship "PAHCNP- Spectroscopy of cosmic dust analogs: study of the interaction with polycyclic aromatic hydrocarbons"
Dr. Abel Brieva, C. Jäger 274794 10/11– 09/13

(D) Supported by the Thüringer Ministerium für Bildung, Wissenschaft und Kultur (TKBWK)

Verbessertes Jacketingverfahren zur Glasfaserherstellung
Prof. E. Wendler Thüringer Aufbaubank 12/12 – 11/14

(E) Supported by other institutions

Virtuelles Institut "MEMRIOX" Memory Effects in Resistive Ion-beam Modified Oxides
Prof. Dr. Carsten Ronning HZDR 10/11 – 09/16

GaN Nanokristalle dotiert mit seltenen Erden
Prof. E. Wendler DAAD/PPP Griechenland 01/13 – 12/14

Structure and stoichiometry of individual Cobald and Europium doped ZnO nanowires
Prof. C. Ronning ESRF Grenoble 04/13 – 09/13

Schwingungsdynamik in komplexen Verbindungshalbleitern
Dr. C.S. Schnohr ProChance, FSU Jena 03/13 – 02/15

Experimente zur Laborastrophysik
Dr. C. Jäger MPI Heidelberg 01/02 – 05/22

5. Publications, Invited Talks, and Conference Contributions

5.1 Publications in Scientific Journals

To tilt or not to tilt: Correction of the distortion caused by inclined sample surfaces in low-energy electron diffraction,
F. Sojka, M. Meissner, C. Zwick, R. Forker, M. Vyshnepolsky, C. Klein, M. Horn-von Hoegen, and T. Fritz,
Ultramicroscopy **133**, 35-40 (2013).

Determination and correction of distortions and systematic errors in low-energy electron diffraction,
F. Sojka, M. Meissner, C. Zwick, R. Forker, and T. Fritz,
Rev. Sci. Instrum. **84**, 015111 (2013).

Optical constants of a- and β-zinc(II)-phthalocyanine films,
M. Kozlik, S. Paulke, M. Gruenewald, R. Forker, and T. Fritz,
Dataset Papers in Physics, 926470 (2013).

A General Approach toward Shape-Controlled Synthesis of Silicon Nanowires
W. Molnar, A. Lugstein, P. Pongratz, M. Seyring, M. Rettenmayr, C. Borschel, C. Ronning, N. Auner, C. Bauch and E. Bertagnolli
Nano Letters **13**, 21 (2013)

DNA hybridization assay at individual, biofunctionalized zinc oxide nanowires
C. Leiterer, B. Seise, I. Slowik, G. Brönstrup, R. Niepelt, K. Weber, C. Ronning, S. Christiansen and W. Fritzsche
Journal of Biophotonics **6**, 143 (2013)

Luminescence and energy transfer processes in ensembles and single Mn or Tb doped ZnS nanowires
U. Kaiser, S. Gies, S. Geburt, F. Riedel, C. Ronning, and W. Heimbrodt
Journal of Applied Physics **113**, 073506 (2013)

Luminescent Ordered Arrays of Nanoporous Silicon Nanopillars and Silicon Nanopillars with Nanoporous Shells
D. Wang, S. Schönherr, S. Du, C. Ronning, and P. Schaaf
Materials Letters **98**, 186 (2013)

The Physics of Copper Oxide (Cu_2O)
B.K. Meyer, A. Polity, D. Reppin, M. Becker, P. Hering, B. Kramm, P.J. Klar, T. Sander, C. Reindl, C. Heiliger, M. Heinemann, C. Müller and C. Ronning
Semiconductors and Semimetals **88**, 201 (2013)

Intense intra-3d-luminescence and waveguiding properties of Co-doped ZnO nanowires
S. Geburt, R. Röder, U. Kaiser, L. Chen, M.H. Chu, J. Segura-Ruiz, G. Martínez-Criado, W. Heimbrodt and C. Ronning
physica status solidi RRL **7**, 886 (2013)

Ordered arrays of patterned nanoporous silicon
D. Wang, S. Schönherr, R. Ji, A. Herz, C. Ronning and P. Schaaf
J. Micromech. Microeng. **23**, 074004 (2013)

Controlled synthesis of ultrathin ZnO nanowires using micellar gold nanoparticles as catalyst templates
H. Yin, Q. Wang, S. Geburt, S. Milz, B. Ruttens, G. Degutis, J. D'Haen, L. Shan, S. Punniyakoti, M. D'Olieslaeger, P. Wagner, C. Ronning and H.-G. Boyen
Nanoscale **5**, 7046 (2013)

Continuous wave nanowire lasing
R. Röder, M. Wille, S. Geburt, J. Rensberg, M. Zhang, J.G. Lu, F. Capasso, R. Buschlinger, U. Peschel and C. Ronning
Nano Letters **13**, 3602 (2013)

Local lattice distortions in single Co-implanted ZnO nanowires
M.H. Chu, G. Martínez-Criado, J. Segura-Ruiz, S. Geburt and C. Ronning
Applied Physics Letters **103**, 141911 (2013)

Magnetic polarons and large negative magnetoresistance in GaAs nanowires implanted with Mn ions
S. Kumar, W. Paschoal Jr., A. Johannes, D. Jacobsson, C. Borschel, A. Pertsova, W.H. Wang, M.K. Wu, C. Canali, C. Ronning, L. Samuelson and H. Pettersson
Nano Letters **13**, 5079 (2013)

Spatially-resolved measurements of charge carrier lifetimes in CdTe solar cells
C. Kraft, H. Hempel, V. Buschmann, T. Siebert, C. Heisler, W. Wesch and C. Ronning
Journal of Applied Physics **113**, 124510 (2013)

Buffer-free Cu(In,Ga)Se_2-solar cells by near-surface ion implantation
J. Haarstrich, M. Teichmann, H. Metzner, M. Gnauck, C. Ronning, W. Wesch, T. Rissom, C.A. Kaufmann, H.W. Schock, V. Scheumann and W. Mannstadt
Solar Energy Materials & Solar Cells **116**, 43 (2013)

Characterization of semiconductor devices and wafer materials via sub-nanosecond time-correlated single-photon counting
V. Buschmann, H. Hempel, A. Knigge, C. Kraft, M. Roczen, M. Weyers, T. Siebert and F. Koberling
Journal of Applied Spectroscopy **80**, 449 (2013)

Atomic-scale structure, cation distribution, and bandgap bowing in Cu(In,Ga)S_2 and Cu(In,Ga)Se_2
S. Eckner, H. Kammer, T. Steinbach, M. Gnauck, A. Johannes, C. Stephan, S. Schorr and C. S. Schnohr
Applied Physics Letters **103**, 081905 (2013)

CdTe grown under Cd/Te excess at very low temperatures for solar cells
C. Heisler, M. Brückner, F. Lind, C. Kraft, U. Reislöhner, C. Ronning, and W. Wesch
Journal of Applied Physics **113**, 224504 (2013)

Transparent CdTe solar cells with a ZnO:Al back contact
C. Heisler, C. S. Schnohr, M. Hädrich, M. Oertel, C. Kraft, U. Reislöhner, H. Metzner and W. Wesch
Thin Solid Films **548**, 627 (2013)

Lift-off protocols for thin films for use in EXAFS experiments
S. Decoster, C. J. Glover, B. Johannessen, R. Giulian, D. J. Sprouster, P. Kluth, L. L. Araujo, Z. S. Hussain, C. Schnohr, H. Salama, F. Kremer, K. Temst, A. Vantomme and M. C. Ridgway
Journal of Synchrotron Radiation **20**, 426 (2013)

Selective ion-induced intermixing and damage in low-dimensional GaN/AlN quantum structures
A. Redondo-Cubero, K. Lorenz, E. Wendler, D. Carvalho, T. Ben, F. M. Morales, R. García,
V. Fellmann and B. Daudin
Nanotechnology **24**, 505717 (2013)

SEM analysis of ion implanted SiC
Johan B. Malherbe, N.G. van der Berg, A.J. Botha, E. Friedland, T.T. Hlatshwayo,
R.J. Kuhudzai, E. Wendler, W. Wesch, P. Chakraborty and E.F. da Silveira
Nuclear Instruments and Methods in Physics Research Section B-Beam Interactions with Materials and Atoms **315**, 136 (2013)

Ion-beam synthesis and characterization of narrow-gap A3B5 nanocrystals in Si: Effect of implantation and annealing regimes
F. Komarov, L. Vlasukova, O. Milchanin, W. Wesch, E. Wendler, J. Zuk and I. Parkhomenko
Materials Science and Engineering: B **178**, 1169 (2013)

Structural and optical properties of silicon layers with InSb and InAs nanocrystals formed by ion-beam synthesis
F. Komarov, L. Vlasukova, M. Greben, O. Milchanin, J. Zuk, W. Wesch, E. Wendler
and A. Togambaeva
Nuclear Instruments and Methods in Physics Research Section B-Beam Interactions with Materials and Atoms **307**, 102 (2013)

Low-temperature damage formation in ion implanted InP
E. Wendler, A. Stonert, A. Turos, and W. Wesch
Nuclear Instruments and Methods in Physics Research Section B-Beam Interactions with Materials and Atoms **307**, 377 (2013)

Comparison of low- and room-temperature damage formation in Ar ion implanted GaN and ZnO
E. Wendler, W. Wesch, A.Yu. Azarov, N. Catarino, A. Redondo-Cubero, E. Alves and K. Lorenz
Nuclear Instruments and Methods in Physics Research Section B-Beam Interactions with Materials and Atoms **307**, 394 (2013)

Ion Beam Synthesis of InAs Nano crystals in Si: Influence of Thin Surface Oxide Layers
F. Komarov, L. Vlasukova, O. Milchanin, M. Greben, A. Komarov, A. Mudryi, W. Wesch,
E. Wendler, J. Zuk, M. Kulik and G. Ismailova
Acta Physica Polonica A **123**, 809 (2013)

Effect of In implantation and annealing on the lattice disorder and nano-mechanical properties of GaN
K. Filintoglou, P. Kavouras, M. Katsikini, J. Arvanitidis, D. Christofilos, S. Ves, E. Wendler and
W. Wesch
Thin Solid Films **531**, 152 (2013)

Ion beam induced stress formation and relaxation in germanium
T. Steinbach, A. Reupert, E. Schmidt and W. Wesch
Nuclear Instruments and Methods in Physics Research Section B-Beam Interactions with Materials and Atoms **307**, 194 (2013)

Simulation of energy barrier distribution using real particle parameters and comparison with experimental obtained results
M. Büttner, M. Schiffler, P. Weber, P. Seidel
Journal of Magnetism and Magnetic Materials **345**, 230–235 (2013).

Tunneling characteristics of superconducting junctions with inhomogeneous tunnel barriers
V. Shaternik, A. Shapovalov, M. Belogolovskii, S. Döring, S. Schmidt, P. Seidel
Mat.-wiss. u. Werkstofftech. **44**, 205–209 (2013).

Low temperature permeability and current noise of ferromagnetic pickup coils
R. Geithner , D. Heinert, R. Neubert, W. Vodel , P. Seidel
Cryogenics **54**, 16–19 (2013).

Dependence of cryogenic strength of hydroxide catalysis bonded silicon on type of surface oxide
N. L. Beveridge, A. A. van Veggel, L. Cunningham, J. Hough, I. W. Martin, R. Nawrodt, S. Reid, S. Rowan
Class. Quantum Grav. **30**, 025003 (2013).

Magnetic properties of multicore magnetite nanoparticles prepared by glass crystallization
C. Worsch, M. Büttner, P. Schaaf , R. Harizanova, C. Rüssel, F. Schmidl, and P. Seidel
J. Mater. Sci. **48**, 2299–2307 (2013).

Bicrystalline Grain Boundary and Hybrid SNS Junctions Based on Ba-122 Thin Films
St. Schmidt, S. Döring, F. Schmidl, V. Tympel, S. Haindl, K. Iida, F. Kurth, B. Holzapfel, P. Seidel
IEEE Trans. Appl. Supercond. **23**, 7300104 (2013).

CW-diode laser crystallization of sputtered amorphous silicon on glass, SiN_X, and SiO_2 intermediate layers
G. Schmidl, G. Andrä, J. Bergmann, A. Gawlik, I. Höger, S. Anders, F. Schmidl, V. Tympel, F. Falk
J. Mater. Sci. **48**, 4177–4182 (2013).

Tunneling into multiband superconductors: The case of magnesium diboride and iron-based superconductors
M. Belogolovskii, P. Seidel
Physics and Engineering of Microwaves, Millimeter and Submillimeter Waves (MSMW), 2013 International Kharkov Symposium on MSMW, IEEE, 157–159 (2013).

Charge transport under microwave irradiation in Josephson heterostructures superconductor - doped semiconductor – superconductor
V. Shaternik, A. Shapovalov, A. Suvorov, S. Döring, S. Schmidt, P. Seidel
Physics and Engineering of Microwaves, Millimeter and Submillimeter Waves (MSMW), 2013 International Kharkov Symposium on MSMW, IEEE, 655–657 (2013).

Matrix induced in-situ growth of crystalline Au nanoparticles for photonic applications
C. Katzer, M. Westerhausen, P. Naujok, H. Bernhardt, G. Schmidl, W. Fritsche, A. Undisz, M. Drüe, M. Rettenmayr, F. Schmidl
Nanophotonic Materials X, edited by St. Cabrini, G. Lerondel, A.M.Schartzberg, T. Mokari, Proc. of SPIE Vol. 8807 88070K (2013).

Structural properties of gold modified $YBa_2Cu_3O_{7-\delta}$ thin films
C. Katzer, M. Westerhausen, I. Uschmann, F. Schmidl, U. Hübner, P. Seidel
Supercond. Sci. Technol. **26**, 125008 (2013).

Gold nanocrystals in high-temperature superconducting films: creation of pinning patterns of choice
C. Katzer, C. Stahl, P. Michalowski, S. Treiber, F. Schmidl, P. Seidel, J. Albrecht, G. Schütz
New Journal of Physics **15**, 113029 (2013).

A Cryogenic Current Comparator for FAIR with Improved Resolution
R. Geithner, W. Vodel, R. Neubert, P. Seidel, F. Kurian, H. Reeg, M. Schwickert
Proceedings of International Beam Instrumentation Conference 2013, Oxford, UK, TUPF32 590 (2013).

Measurements with the upgraded cryogenic current comparator
F. Kurian, M. Schwickert, H. Reeg, P. Kowina, P. Huelsmann, R. Neubert, W. Vodel, R. Geithner
Proceedings of International Beam Instrumentation Conference 2013, Oxford, UK, TUPF30 583 (2013).

20 Years of Development of SQUID-based Cryogenic Current Comparator for Beam Diagnostics
W. Vodel , R. Geithner, R. Neubert, P. Seidel, , H. Reeg, M. Schwickert, K. Knaack, K. Wittenburg, A. Peters
Proceedings of IPAC2013, Shanghai, China, MOPME013 497 (2013).

Investigation of mechanical losses of thin silicon flexures at low temperatures
R. Nawrodt, C. Schwarz, S. Kroker, I. W. Martin, R. Bassiri, F. Brückner, L. Cunningham, G. D. Hammond, D. Heinert, J. Hough, T. Käsebier, E.-B. Kley, R. Neubert, S. Reid, S. Rowan, P. Seidel, A. Tünnermann
Class. Quantum Grav. **30**, 115008 (2013).

Coherent radiation in serial arrays of Josephson junctions
A. Grib, M. Mans, M. Büenfeld, J. Scherbel, F. Schmidl, P. Seidel, H. Schneidewind
IEEE 14th International Superconductive Electronics Conference (ISEC) (2013).

Calculation of thermal noise in grating reflectors
D. Heinert, S. Kroker, D. Friedrich, S. Hild, E.-B. Kley, S. Leavey, I. W. Martin, R. Nawrodt, A. Tünnermann, S. P. Vyatchanin, K. Yamamoto
Phys. Rev. D **88**, 042001 (2013).

The abundances of hydrocarbon functional groups in the interstellar medium inferred from laboratory spectra of hydrogenated and methylated polycyclic aromatic hydrocarbons
M. Steglich, C. Jäger, F. Huisken, M. Friedrich, W. Plass, H.-J. Räder, K. Müllen, and Th. Henning
Astrophys. J. Suppl. Ser. **208**, 26/1 – 26/22 (2013).

Analogs of solid nanoparticles as precursors of aromatic hydrocarbons
K. A. K. Gadallah, H. Mutschke, and C. Jäger
Astron. Astrophys. **554**, A12/1 – A12/9 (2013).

5.2 Invited Talks at Conferences and Colloquia

T. Fritz:

Epitaxial Organic Thin Films of Large Aromatic Hydrocarbons - Structure and Physical Properties
AMAZING Workshop, Da Nang (Vietnam), 16.-24.03.2013

Optical in situ Differential Reflectance Spectroscopy on Epitaxially Grown Molecular Films
10th International Conference on Optics of Surfaces and Interfaces (OSI 10)
Chemnitz, 8.-13.09.2013

Optical in situ Differential Reflectance Spectroscopy (DRS): A Powerful Tool to Investigate Ultrathin Molecular Films"

International Workshop on Surface Sensitive Optical Spectroscopy, Tianjin University, Tianjin (China), 3.-5.11.2013

C. Ronning:

Ion beam doping of semiconductor nanowires
Physikalisches Kolloquium, Universität Leipzig, 17.12.2013

Semiconductor nanowire photonics
Materials Research Society (MRS) fall meeting, session SS, Boston, 2.12.2013

Semiconductor nanowires for photonic applications
Seminar at Graduate School MAterials science IN mainZ, U Mainz, 30.10.2013

Lasing in Semiconductor nanowire
Focus workshop on Nanowires for Optoelectronics, TU Munich, 28.10.2013

Semiconductor nanowire photonics
Department of Physics and Astronomy, University of Southern California, 9.9.2013

Ion beam doping of semiconductor nanowires
Los Alamos National Laboratory, 5.9.2013

Lasing in ZnO and CdS nanowires & optical doping of ZnO nanowires
Seminar at SEAS, Harvard University, 31.7.2013

CIGS and CdTe thin film photovoltaics
Seminar at Institute of Materials Science, University of Connecticut, 30.7.2013

Semiconductor nanowires: synthesis, doping and photonic applications
Seminar of the Department of Physics, Imperial College, London, 26.6.2013

Ion beam synthesis and ion irradiation of cubic boron nitride
1st Midsummer workshop on boron nitride based materials, Uppsala, Schweden, 19.6.2013

Semiconductor nanowires for optoelectronics
Workshop der school for contacts in nanosytems, Niedersächsische Technische Hochschule, Goslar, 15.6.2013

Sequentielle Synthese, Ionenstrahldotierung und elektrische Charakterisierung von CIGS Solarzellen
Seminar am ISE Fraunhofer Institut, Freiburg, 31.5.2013

Ion beam doping of semiconductor nanowires
Spring meeting of the E-MRS, Session P, Strasbourg, France, 29.5.2013

CIGS and CdTe thin film photovoltaics
Colloquium of the Physics Department, University of Pretoria, Südafrika, 28.3.2013

Semiconductor nanowires: growth, doping and photonic applications
Colloquium of the Physics Department, University of Witwatersrand, Johannesburg, Südafrika, 27.3.2013

P. Seidel:

Tunneling into multiband superconductors: the case of magnesium diboride and iron-based superconductors
8th Internat. Symposium on Physics and Engineering of Microwaves, Kharkov, Ukraine, 26.06.2013

Josephson effects in iron-based superconductors
Trilateral Workshop on Hot Topics in HTSC: Fe-based Superconductors, Zvenigorod, Russia, 02.10.2013

Josephson effects in iron-based superconductors
Chalmers University of Technology, Göteborg, Sweden, 29.08.2013

Superconducting electronics: basics
EUCAS Summer School "New Trends with Superconductivity Quantum Detectors, Genova, Italy, 10.09.2013

E. Wendler:

Damage formation in ion implanted semiconductors at 15 K and its correlation with primary energy deposition and general material properties
21th International Conference on Ion Surface Interactions, Yaroslavl, Russia, 22. – 26. August 2013

F. Huisken:

Laboratory studies on the role of PAHs as DIB carriers
The Diffuse Interstellar Bands, International Astronomical Union (IAU) Symposium 297, Haarlem, The Netherlands, May 20 – 24, 2013

Reactions of metal atoms and clusters with oxygen and hydrocarbons in helium droplets
International Conference on Quantum Fluid Clusters QFC2013, Thon-Dittmer-Palais, Regensburg, Germany, June 16 – 19, 2013

Laboratory experiments for the interpretation of astrophysical phenomena
Workshop Laboratory Astrophysics 2013, Schlosshotel Bad Wilhelmshöhe, Kassel, Germany, September 30 – October 2, 2013

C. Jäger:

Condensation and Processing of Dust in Astrophysical Environments
Workshop on "Dust Growth in Star- and Planet-Forming Environments ", Heidelberg, 22-25 Juli 2013

I.Laboratory experiments on cosmic dust condensation, &
II. Laboratory experiments on cosmic dust processing
LASSIE 2013 Summer School "State-of-the-art Astrochemistry", Observatory of Paris, France, 4.-6. September 2013

Condensation and Processing of Dust in Astrophysical Environments
Conference on "Physical Processes in the ISM ", MPE Garching, 21.-25. Oktober 2013

R. Forker:

Differential Reflectance Spectroscopy (DRS) and Classification of Epitaxy
Osaka University, Bereichsseminar (Prof. Dr. Munakata), Osaka, Japan, 26.06.2013

Nanoscale Interfaces for Organic Electronics
Kyoto University, Bereichsseminar (Prof. Dr. Matsumoto), Kyoto, Japan, 04.07.2013

Nanoscale Interfaces for Organic Electronics
Chiba University, Bereichsseminar (Prof. Dr. Ueno), Chiba, Japan, 05.09.2013

C.S. Schnohr:

Atomic-scale structure and cation distribution in $Cu(In,Ga)Se_2$ *and* $Cu(In,Ga)S_2$
Euromat 2013 - European Congress and Exhibition on Advanced Materials and Processes, Sevilla, Spanien, 9.-13. September 2013

Atomic-scale structure, cation distribution and band gap bowing in Cu(In,Ga)Se2
25th Nordic Semiconductor Meeting, Espoo, Finnland, 9.-12. Juni 2013

R. Nawrodt:

Optics for Future Detectors
GWADW 2013, LaBiolola/Elba, Italy, 20.05.2013

Material issues for future gravitational wave detectors
Gravitational Exchange Meeting, Tokyo Tech., Japan, 06.12.2013

F. Sojka:

Compensating geometric distortions in LEED images for enhanced quantitative analysis
SPA-LEED-Workshop Universität Bonn, 26./27.09.2013

R. Röder:

Semiconductor Nanowire Photonics
International Max Planck Research School “Physics of Light”, Erlangen, 25. Juli 2013

A. Johannes:

Wiring Quantum Dots
Seminar at iThemba Labs, Kapstadt, Südafrika, 19. Juni 2013

5.3 Conference Contributions

Frühjahrstagung DPG Regensburg, March 1–15, 2013

M. Grünewald, K. Wachter, R. Forker, and T. Fritz
Organic heteroepitaxy of PTCDA and SnPc on single crystalline metals

M. Meißner, F. Sojka, M. Grosch, T. Dienel, T. Fritz
On the similarity of multiple scattering and the Moiré Effect in reciprocal space and how to make use of it in LEED

M. Kozlik, S. Paulke, M. Gruenewald, R. Forker, and T. Fritz
Optoelectronic Properties Of Zinc(II)-Phthalocyanine

H. Holland-Moritz, C. Borschel, S. Scheeler, C. Pacholski and C. Ronning
Sputtering effects on ion irradiated Au nanoparticles

R. Röder, S. Geburt, R. Buschlinger, U. Peschel and C. Ronning
Polarization dependent CdS nanowire lasing

J. Rensberg, B. Roessler, C. Katzer, F. Schmidl and C. Ronning
Resistive switching properties in ion beam modified $SrTiO_3$

R. Pickenhain, F. Schmidt, S. Geburt, C. Ronning, H. von Wenckstern and
M. Grundmann
Iron-induced gap states in ZnO thin films

S. Vatterodt, J. Rensberg, D. Buerger, H. Schmidt and C. Ronning
Electrical and optical properties of tungsten doped VO_2 *thin films*

F. Felgenträger, J. Rensberg, S. Milz, C. Ronning and W. Wesch
Ion beam enhanced etching of LiNbO3 containing silver nano clusters for plasmonic waveguide applications

M. Wille, S. Geburt, R. Röder, M. Zhang, J. Grace Lu and C. Ronning
Optical properties of Sn-doped CdS nanowires

R. Röder, S. Geburt, A. Johannes, M. Glaser, A. Lugstein and C. Ronning
Tailoring CdS nanowire lasing resonators

M. Ogrisek, A. Johannes und C. Ronning
Einfluss der Prozessparameter auf das Wachstum von ZnO-Nanodrähten

B. Roessler, J. Rensberg, F. Schmidl and C. Ronning
Structural and resistive switching properties of $SrTiO_3$ *deposited by RF sputtering*

S. Gemming, D. Blaschke, K. Potzger, P. Zahn, A. Bogusz, H. Schmidt, T. Mikolajick,
S. Slesazeck, H. Wylezich, B. Abendroth, D. C. Meyer, S. Rentrop, R. Dittmann,
K. Skaja, R. Waser, J. Rensberg, C. Ronning, N. A. Spaldin and D. Basov
Memory Effects in Resistive Ion-beam Modified Oxides

A. Kusch, M. Oertel, D. Stoll, U. Reislöhner and C, Ronning
Electro-optical charaterization of CIGS solar cells with varied absorber compositions

M. Krauße, C. Kraft, H. Hempel, V. Buschmann, T. Siebert, C. Heisler, W. Wesch
and C. Ronning
Spatially-resolved measurements of charge carrier lifetimes in CdTe solar cells

S. Gies, U. Kaiser, W. Heimbrodt, S. Geburt and C. Ronning
Analysis of the energy transfer process in ZnS:Mn and ZnS:Tb by a modified Förster model

E. Wendler, W. Wesch, A. Yu. Azarov, N. Catarino, A. Redondo-Cubero, E. Alves and K. Lorenz
Comparison of low- and room-temperature damage formation in Ar ion implanted GaN and ZnO

E. Schmidt, T. Steinbach and W. Wesch
The role of defect-types in ion beam induced stress in $LiNbO_3$

M. Schmidt, J. Rensberg, F. Schrempel and W. Wesch
Temperature- and orientation-dependent damage-formation due to electronic energy deposition in $LiNbO_3$

M. Salge, C. Schnitter, C. Heisler, C. Kraft and W. Wesch
Plasma induced nitrogen incorporation in CdTe-layers for solar cell applications

F. Lind, J. Krammer, C. Heisler, C. Kraft, C.-H. Fischer and W. Wesch
Electrical and structural characterization of CdTe thin film solar cells with In2S3 buffer layer

S. Eckner, H. Kämmer, T. Steinbach, M. Gnauck, A. Johannes, C. Stephan, S. Schorr and C. S. Schnohr
Composition-dependent atomic-scale structure of Cu(In,Ga)S2

B. Roessler, J. Rensberg, F. Schmidl, C. Ronning
Structural and resistive switching properties of $SrTiO_3$ *deposited by RF sputtering*

J. Rensberg, B. Roessler, Ch. Katzer, F. Schmidl, C. Ronning
Resistive switching properties in ion beam modified $SrTiO_3$

H. Bernhardt, Ch. Katzer, S. Christke, F. Schmidl, G. Schmidl, W. Fritzsche, J. Petschulat, Th. Pertsch, M. Rettenmayr
Optical resonances of self-organized monocrystalline Au nanoparticles embedded in a $SrTiO_3$ *matrix*

P. Naujok, Ch. Katzer, P. Michalowski, F. Schmidl, M. Westerhausen, G. Schmidl, R. Mueller, J. Dellith, Ch. Schmidt, J. Jatschka, W. Fritzsche
Matrix-induced in situ growth of plasmonic Au nanoparticles for biological sensor devices

St. Schmidt, S. Döring, M. Feltz, N. Ali Hasan, S. Gottwals, F. Schmidl, S. Haindl, K. Iida, F. Kurth, B. Holzapfel, P. Seidel
Investigations of pnictide superconductors - three Josephson junction aproaches

Ch. Katzer, C. Stahl, P. Michalowski, S. Treiber, G. Christiani, F. Schmidl, P. Seidel, G. Schütz, J. Albrecht
Gold nanocrystals in high-temperature superconducting films: Creation of pinning patterns of choice

M. Monecke, St. Schmidt, S. Döring, M. Feltz, N. Ali Hasan, D. Reifert, F. Schmidl, P. Seidel
Processing of insulation barriers for the development of tunneling junctions based on pnictide superconductors

M. Feltz, St. Schmidt, S. Döring, D. Reifert, S. Gottwals, N. Ali Hasan, M. Monecke, F.Schmidl, K. Iida, F. Kurth, B. Holzapfel, P. Seidel
Josephson junctions based on pnictide superconductors

D. Reifert, St. Schmidt, S. Döring, M. Feltz, S. Gottwals, N. Ali Hasan, M. Monecke, Th. Wolf, F. Schmidl, P. Seidel
Studies on the processing of Ba-122 single crystals for the development of tunnel junctions

S. Gottwals, S. Döring, St. Schmidt, N. Ali Hasan, F. Schmidl, F. Kurth, K. Iida, B. Holzapfel, I. Mönch, P. Seidel
Conductance spectra investigations of ironarsenide superconductor in planar junctions

Hybrid Photovoltaics, Berlin, May 15-17, 2013

M. Kozlik, M. Gruenewald, S. Paulke, R. Forker, C. Ronning, T. Fritz
Hybrid Solar Cells made of Phthalocyanines and Zinc Oxide Nanowires

SPA-LEED-Workshop, Bonn, Sept. 26-27, 2013

M. Meissner, A. Winkelmann, L. Matthes, F. Sojka, and Torsten Fritz

IVC 19/ICN+T, Paris, Sept. 9-13, 2013

M. Kozlik, S. Paulke, M. Gruenewald, R. Forker, and T. Fritz
Optoelectronic Properties Of Zinc(II)-Phthalocyanine

OSI 10, Chemnitz, Sept. 8-13, 2013

M. Gruenewald, K. Wachter, M. Meissner, M. Kozlik, F. Sojka, R. Forker, and T. Fritz
Organic Heteroepitaxy of PTCDA and SnPc on Single Crystalline Metals

CLEO Europe, München, May 12 – 16, 2013

T. Sidiropoulos, S. Geburt, R. Röder, M. Ogrisek, S.A. Maier, C. Ronning, R. F. Oulton
Room temperature plasmonic nanowire laser near the surface plasmon frequency

Spring meeting of the E-MRS, Strassbourg, France, May 26 – 31, 2013

M. H. Chu, G. Martinez-Criado, J. Segura-Ruiz, S. Geburt, C. Ronning, E. Secco and N. Garro
Local structural comparison of as-implanted and thermal-annealed Co doped ZnO nanowires

S. Gemming, D. Blaschke, K. Potzger, P. Zahn, A. Bogusz, H. Schmidt, T. Mikolajick, S. Slesazeck, H. Wylezich, B. Abendroth, D.C. Meyer, S. Rentrop, R. Dittmann, V. Rana, K. Skaja, R. Waser, J. Rensberg, C. Ronning, N. Spaldin and D. Basov
Memory effects in resistiveion-beam modified oxides

7th Interantional Conference on Materials for Advanced Technologies (ICMAT), Singapore, June 30 – July 5, 2013

A. Lugstein, W. Molnar, P. Pongartz, M. Seyring, M. Rettenmayr, C. Borschel, C. Ronning, N. Auner, C. Bauch, E. Bertagnolli

Shape Control Method for Prismatic Si-NWs by Subeutectic VLS Growth using Cubic α–NiSi2 as Catalyst

International Conference on One-dimensional Nanomaterials (ICON), Annecy, France, September 22 – 26, 2013

A. Johannes , S. Noack , H. Holland-Moritz, C. Borschel, S. Kumar, W. Paschoal, C. M. Canali, L. Samuelson, H. Pettersson, C. Ronning
Ion beam tailoring of nanowire diameters

A. Pescaglini, E. Secco, D. Cammi, C. Ronning, N. Garro, and D. Iacopino
Tunable Raman Scattering in Au Nanorods Decorated ZnO Nanowires Hybrid Structures

D. Cammi, C. Bückmann, C. Ronning
Surface Modification of ZnO Nanowires with Plasma and Annealing Treatments for Hydrogen Sensing

Workshop on ion beams, Leipzig, June 12 – 14, 2013

H. Holland-Moritz, C. Borschel, S. Scheeler, C. Pacholski and C. Ronning
Sputtering effects on ion irradiated Au nanoparticles

Mikrosystemtechnik-Kongress des VDE, Aachen, October 14 – 16, 2013

F. Krippendorf, C. Csato, T. Bischof, S. Gupta, W. Han, M. Nobst, C. Ronning, R. Rupp, M. Rüb, A. Schewior, W. Wesch
Energiefilter für Ionenimplantation

Fall meeting of the Material Research Society (MRS), Boston, USA, December 1 – 6, 2013

R. Röder, M. Wille, S. Geburt, J. Rensberg, M. Zhang, J. G. Lu, R. Buschlinger, U. Peschel, F. Capasso, C. Ronning
Continuous wave green nanowire laser

F. Schmidt, S. Müller, R. Pickenhain, H. von Wenckstern, S. Geburt, C. Ronning, M. Grundmann
Defect studies on Ar-implanted ZnO thin films

R. Oulton, T. Sidiropoulos, O. Hess, S. Maier, S. Geburt, R. Röder, C. Ronning
Ultrafast ZnO Nanowire Lasers near the Surface Plasmon Polariton Frequency

7th Nanowire workshop, Lausanne, June 9 – 11, 2013

M. H. Chu, G. Martinez-Criado, J. Segura-Ruiz, S. Geburt and C. Ronning
Exploring atomic lattice distortions generated in single Co implanted ZnO nanowires

18th International Conference on Surface Modification of Materials by Ion Beams (SMMIB), Kusadasi, Turkey, September 15-20, 2013

H. Holland-Moritz, C. Borschel, S. Scheeler, C. Pacholski, C. Ronning
Sputtering effects on ion irradiated Au nanoparticles

17th International Conference Radiation Effects in Insulators, June 30 – Jul< 5 2013, Helsinki, Finnland

E. Wendler, K. Lorenz
RBS channelling studies of Ar ion implanted GaN

E. Wendler, M. Schilling
Low-temperature damage formation in ion implanted SiC

J. Rensberg, T. Bierschenk, M.C. Ridgeway, B. Afra, M.D. Rodriguez, P .Kluth, J. Sommerfeld, S. Milz, W. Wesch
Track morphology and amorphization kinetics induced by 185 MeV Au-ion irradiation in LiNbO3

E. Schmidt, T. Steinbach, W. Wesch
Ion-beam induced stress-evolution in Lithium Niobate

SPP-Workshop "Hochtemperatursupraleitung in Eisenpniktiden", Bad Honnef, January 23-25, 2013

P. Seidel, S. Döring, S. Schmidt, F. Schmidl, V. Tympel
Josephson effects in iron pnictides: Phase-sensitive experiments

DPG-Tagung Jena, February 25 – March 01, 2013

J. Komma, G. Hofmann, Ch. Schwarz, D.Heinert, J. Steinlechner, R. Schnabel, P. Seidel, R. Nawrodt
Optical properties of silicon

G. Hofmann, J. Komma, Ch. Schwarz, D. Heinert, P. Seidel, A. Tünnermann, R. Nawrodt
Mechanical loss of sapphire at low temperatures

Ch. Schwarz, J. Komma, G. Hofmann, D. Heinert, St. Kroker, A. Tünnermann, P. Seidel, R. Nawrodt
Silicon surfaces and its impact on gravitational wave detectors

D. Heinert, St. Kroker, D. Friedrich, St. Hild, I. Martin, R. Nawrodt, P. Seidel, A. Tünnermann, S. Vyatchanin, K. Yamamoto
Thermal noise in grating reflectors

G. Hofmann, Ch. Schwarz, J. Komma, D. Heinert, P. Seidel, A. Tünnermann, R. Nawrodt
New materials for low noise measurements

B. Walter, J. Komma, G. Hofmann, Ch. Schwarz, D. Heinert, P. Seidel, C. Schnohr, R. Nawrodt
Mechanical loss of ion-implanted tantala layers

P. Pastrik, J. Komma, G. Hofmann, Ch. Schwarz, D. Heinert, P. Seidel, R. Nawrodt
Optical absorption of silicon around the fundamental band gap at low temperatures

J. Komma, G. Hofmann, Ch. Schwarz, D. Heinert, J. Steinlechner, R. Schnabel, P. Seidel, R. Nawrodt
Optical absorption measurements of silicon at 1550 nm

3rd IRON-SEA Meeting, Osaka, Japan, March 5-6, 2013

P.Seidel
Progress in realization of thin film Josephson junctions with iron-based superconductors using different geometries

S. Döring
Progress in thin film junctions with different geometries

S. Schmidt
Bicrystalline grain boundary junctions based on Ba-122 thin films and advances in Ba-122 single crystal preparation

P. Seidel, S. Döring, S. Schmidt, F. Schmidl, V. Tympel
Josephson effects in iron pnictides: Phase-sensitive experiments

IPAC13, 4th International Particle Accelerator Conference, Shanghai, China, May 12-17, 2013

W. Vodel , R. Geithner, R. Neubert, P. Seidel, , H. Reeg, M. Schwickert, K. Knaack, K. Wittenburg, A. Peters
20 Years of Development of SQUID-based Cryogenic Current Comparator for Beam Diagnostics

QM13 – 4th Internat. Conference on Quantum Metrology Poznan, Poland, May 15 -17, 2013

P. Seidel
Opto-mechanical materials for low noise operation at cryogenic temperatures

Y. Shukrinov, P. Seidel, W. Nawrocki
The perspective of intrinsic Josephson junctions for quantum metrology

GWADW 2013 – Gravitational Wave Advanced Detector Workshop, LaBiodola/Elba, Italy, May 19 – 25, 2013

R. Nawrodt
Optics for Future Detectors

G. Hofmann, J. Komma, C. Schwarz, D. Heinert, K. Haughian, G. D. Hammond, P. Murray, K. Craig, P. Seidel, J. Hough, S. Rowan, R. Nawrodt
Bulk silicon mechnical loss for estimates of thermal noise

J. Komma, G. Hofmann, C. Schwarz, P. Pastrik, D. Heinert, R. Nawrodt
Optical measurements at cryogenic temperatures

Internat. Symposium Molecular Plasmonics 2013, Jena, May 23-25, 2013

C. Katzer, F. Schmidl, P. Michalowski, P. Naujok, R. Diener, G. Schmidl, J. Dellith, J. Jatschka, R. Mueller, W. Fritzsche
Matrix induced in-situ growth of crystalline gold nanoparticles

EDA workshop Superconducting front-end microwave electronics, Brussels, Belgium, May 30, 2013

C. Katzer, F. Schmidl, M. Westerhausen, R. Diener, P. Michalowski, P. Seidel
Tuning YBCO thin films, Joesphson junctions and dc-SQUID gradiometers by embedding Au nanocrystals

8th Internat. Symposium on Physics and Engineering of Microwaves, Millimeter and Submillimeter Waves (MSMW'13), Kharkov, Ukraine, June 23-28, 2013

M. Belogolovskii, P. Seidel
Tunneling into multiband superconductors: the case of magnesium diboride and iron-based superconductors

V. Shaternik, A. Shapovalov, A. Suvorov, S. Döring, S. Schmidt, P. Seidel
Charge transport under microwave irradiation in Josephson heterostructures superconductor-doped semiconductor-superconductor

14th Superconductive Electronics Conference ISEC 2013, Cambridge, MA, July 7-11, 2013

A. Grib, M. Mans, M. Büenfeld, J. Scherbel, F. Schmidl, P. Seidel, H. Schneidewind
Coherent radiation in serial arrays of Josephson junctions

Y. Shukrinov, Ilhom Rahmonov, K. Kulikov, P. Seidel, E. Il'ichev
Effect of Radiation and Resonances in Coupled Linear Josephson Junctions Arrays with an LC-Shunt

SPIE Optics + Photonics, San Diego, California United States, August 25-29, 2013

C. Katzer, M. Westerhausen, P. Naujok, H. Bernhardt, G. Schmidl, W. Fritzsche, A. Undisz, M. Drüe, M. Rettenmayr, F. Schmidl
Matrix induced in-situ growth of crystalline Au nanoparticles for plasmonic applications

4th IRON-SEA Meeting, Torino, Italy, September 13 – 14, 2013

P. Seidel
Progress in Josephson junctions with iron-based superconductors

S. Döring
Progress in planar thin film Josephson junctions

S. Schmidt
Bikristalline grainboundary junctions base on Co-doped and P-doped Ba-122 thin films

P. Seidel, S. Döring, F. Schmidl, V. Tympel
Josephson effects in iron pnictides: Phase-sensitive experiments

11th European Conference on Applied Superconductivity (EUCAS), Genova, Italy, September 15-19, 2013

S. Döring, S. Schmidt, S. Gottwals, F. Schmidl, V. Tympel, I. Mönch, F. Kurth, K. Iida, B. Holzapfel, P. Seidel
Influence of the spreading resistance on the conductance spectrum of planar hybrid thin film SNS' junctions based on iron pnictides

S. Schmidt, S. Döring, F. Schmidl, F. Kurth, K. Iida, B. Holzapfel, P. Seidel
Bicrystalline grain boundary Josephson junctions of Co-doped Ba-122 thin films

A. Grib, P. Seidel
Coherent emission of intrinsic Josephson junctions

V. Shaternik, A. Shapovalov, A. Suvorov, P. Seidel, S. Schmidt
Planar Josephson MoRe-doped Si-MoRe junctions: evidence for a resonant tunneling mechanism

C. Katzer, C. Stahl, P. Michalowski, S. Treiber, M. Westerhausen, R. Diener, F. Schmidl, P. Seidel, G. Schütz, J. Albrecht
Realization of arbitrary patterns in high temperature superconducting YBa2Cu3O7-X thin films

F. Schmidl, C. Katzer, P. Michalowski, S. Koch, V. Tympel
Grain boundary engineering with gold nanoparticles

International Beam Instrumentation Conference 2013 (IBIC), Oxford, UK, September 16-19, 2013

R. Geithner, W. Vodel, R. Neubert, P. Seidel, F. Kurian, H. Reeg, M. Schwickert
A Cryogenic Current Comparator for FAIR with Improved Resolution

F. Kurian, M. Schwickert, H. Reeg, P. Kowina, P. Huelsmann, R. Neubert, W. Vodel, R. Geithner
Measurements with the upgraded cryogenic current comparator

8th FLUXONICS RSFQ Design Workshop 2013, University of Technology, Ilmenau, September 23-25, 2013

C. Katzer
Tuned YBCO thin films and devices by embedding Au nanocrystals

Trilateral Workshop on Hot Topics in HTSC: Fe-based Superconductors, Zvenigorod, Russia, September 29 – October 2, 2013

P. Seidel, S. Döring, F. Schmidl, S. Schmidt, V. Tympel
Josephson effects in iron-based superconductors

S. Döring
Thin film Josephsons junctions fort he characterization of ion-based superconductors

Tagung Kryoelektronische Bauelemente KRYO 2013, Bad Herrenalb, October 06-08, 2013

F. Schmidl, C. Katzer, P. Michalowski, S. Koch, E. Treiber, V. Tympel
Grain boundary Josephson junctions with Au nanocrystals

F. Schmidl, C. Katzer, P. Michalowski, S. Koch, E. Treiber, V. Tympel
YBCO grain boundary Josephson junctions with gold nanoparticles

D. Reifert, M. Monecke, S. Schmidt, S. Döring, V. Tympel, F. Schmidl, T. Wolf, F. Kurth, K. Iida, B. Holzapfel, P. Seidel
Processing of Josephson junctions on iron based superconductors

V. Tympel, M. Feltz, St. Schmidt, S. Döring, D. Reifert, S. Gottwals, N. Ali Hasan, M. Monecke, F. Schmidl, K. Iida, F. Kurth, B. Holzapfel, P. Seidel
Josephson junctions based on pnictide superconductors

5th Einstein Telescope Symposium, Hannover, October 22 – 23, 2013

R. Nawrodt
Investigations of mechanical, optical and thermal properties of materials for future GW detectors

D. Heinert
The effect of anisotropy onto Brownian noise in Sapphire and Silicon test masses

B. Walter, J. Komma, G. Hofmann, C. Schwarz, D. Heinert, P. Seidel, C. Schnohr, R. Nawrodt
Mechanical Loss if Ion-Implanted Dielectric Films

J. Komma, G. Hofmann, C. Schwarz, D. Heinert, J. Degallaix, D. Forest, G. Cagnoli, J. Steinlechner, A. Khalaidovski, R. Schnabel, P. Seidel, R. Nawrodt
Optical absorption measurements on silicon at 1550 nm

The Diffuse Interstellar Bands, International Astronomical Union (IAU) Symposium 297, Haarlem, The Netherlands, May 20 – 24, 2013

G. Rouillé, C. Jäger, F. Huisken, and Th. Henning
Polyynyl-substituted PAH molecules and DIB carriers

C. Jäger
Hydrogenated Amorphous Carbon and Kerogene – Carriers of the DIBs

International Conference on Quantum Fluid Clusters QFC2013, Thon-Dittmer-Palais, Regensburg, Germany, June 16 – 19,2013

S. Krasnokutski, G. Rouillé, C. Jäger, F. Huisken, K. Potrick, and Th. Henning
Formation of interstellar silica dust analogs inside helium nanodroplets

The 6th meeting on Cosmic Dust, Center for Planetary Science, Kobe, Japan, August 5 – 9, 2013

G. Rouillé, S. A. Krasnokutski, K. Potrick, C. Jäger, F. Huisken, and Th. Henning
Condensation of silicon monoxide at cryogenic temperatures

The Life Cycle of Dust in the Universe: Observations, Theory, and Laboratory Experiments, Academia Sinica, Taipei, Taiwan, November 18 – 22, 2013

G. Rouillé, S. A. Krasnokutski, C. Jäger, F. Huisken, and Th. Henning
Cosmic dust formation at cryogenic temperatures

C. Jäger, T. Sabri, Th. Henning, and E. Wendler
Laboratory studies on dust processing in astrophysical environments

Workshop Laboratory Astrophysics 2013, Schlosshotel Bad Wilhelmshöhe, Kassel, Germany, September 30 – October 2, 2013

G. Rouillé
Condensation of silicates in the interstellar medium

D. Fulvio
(Poster) Chemistry induced by photons and ions in ice-coated carbons

5.4 Theses

(A) PhD Theses

Sebastian Geburt	*Lasing and ion beam doping of semiconductor nanowires*
Stephan Pohlner	*Impact of indium sulphide based buffer layers on the electrical properties of CIGSSe thin film solar cells*
René Geithner	*Optimierung eines kryogenen Stromkomperators für den Einsatz als Strahlmonitor*

(B) Diploma and Master Theses, Staatsexamensarbeit

Marcel Grosch	*Epitaktisches Wachstum von Oxidschichten auf Ni_3Al-Einkristallen*
Christian Udhardt	*Molecules on Surfaces - Investigations of Rubrene Thin Films on Graphite and Highly Ordered Pyrolytic Graphite*
Tino Kästner	*Dotierung molekularer Schichten*
Matthias Ring	*Kontaktierung und Untersuchung des Kontaktwiderstandes von Indiumsuld-Dünnschichten*
Stefanie Eckner	*Untersuchung der atomaren Struktur von Cu(In,Ga)S2 mittels Röntgenabsorptionsspektroskopie*
David Stoll	*Herstellung von Cu(In,Ga)Se2-Solarzellen in einem sequentiellen Prozess*

Hannes Hempel	*Spektroskopische und elektrische Untersuchungen an Phosphor-dotiertem CdTe*
Felix Felgenträger	*Nanostrukturierung von ionenimplantiertem Lithiumniobat*
Matthias Ogrisek	*Kontrolliertes Wachstum von Zinkoxid und Vanadium(IV)-oxid Nanodrähten*
Marcel Wille	*Optische und elektrische Eigenschaften von Zinn-dotierten CdS Nanodrähten*
Stefanie Koch	*Untersuchungen zu LC-Resonanzen von HTSL DC-SQUIDs*
Markus Westerhausen	*Strukturelle Untersuchungen an epitaktischen Schichten mit Gold-Nanopartikeln*
Sandra Gottwals	*Untersuchungen an Fe-basierten Supraleitern*
Philipp Naujok	*Herstellung und Charakterisierung von YBCO-Matrix-modifizierten Gold Nanopartikeln*
Manuel Monecke	*Herstellung und Charakterisierung von Dünnschichtbarrieren für supraleitende Bauelemente*
Hendrik Bernhardt	*Au-Nanopartikel in dünnen SrTiO3-Schichten*
Markus Weidner	*Auswirkungen von MeV Bestrahlung auf Clusterbildung in epitaktischen Schichten*
Arnulf Thieme	*Sputtern von STO – Schichten*
Albrecht Töpfer	*Absorption elektromagnetischer Strahlung in Halbleitern*
Martin Engler	*Die „Physica pauperum“ und die „Glasphysik“ nach Hermann Schaeffer*

(C) Bachelor Theses and Studienarbeiten

Konrad Ritter	*Optische Frequenzverdopplung an dünnen Siliziumstrukturen*
Martin Gebhardt	*Dotierung von Zinkphthalocyanin zur Anwendung in Solarzellen*
Paul Louis Gerlach	*Quantitative Charakterisierung eines MCP-LEED Gerätes*
Arthur Jungkind	*Ionenstrahlanalyse von Cäsium-dotiertem Strontiumtitanat*
Helge Neumann	*Proteinadsorption auf diamantähnlichen Kohlenstoffschichten - Optimierung des Analyseverfahrens*
Sven Bauer	*Strukturelle Analyse von ZnO/Cu-Nanostrukturen*
Felix Otto	*Optimierung der Cadmiumsulfid-Pufferschicht für Substrate mit und ohne intrinsischer Schicht in Cadmiumtellurid-Solarzellen*
Alexander Tille	*Energiedispersive Röntgenspektroskopie und Kathodolumineszenz Messungen an CISe- / CIGSe Lamellen*

Robert Cordts	*Numerische Berechnung der Dekanalisierungsfunktion und Auswertung der RBS/C-Spektren von* $LiNbO_3$
Ellen Butz	*Herstellung und Charakterisierung von Si-Cantilevern*
Rene Glaser	*Untersuchung des mechanischen Verlusts im thermischen Nichtgleichgewicht*
Felix Küster	*Präzisionsmessungen an Laborspiegeln hoher Reflektivität*
Alexandra Scholz	*Clusterexperimente an dünnen Goldschichten*
Enrico Treiber	*Temperaturabhängige Messungen von Korngrenzenkontakten*
Lukas Trefflich	*Plasmachemisches Ätzen von Fotolacken*
Jonas Gronemann	*Herstellung von Hochtemperatursupraleiterschichten bei variierten Herstellungsparametern*

6. Cooperations, Guests and Colloquia at the IFK

The Institute of Solid State Physics collaborates with a large number of Institutes and Universities in Germany and around the world and has also close connections with several companies. In the framework of these wide spread contacts in 2013 a number of scientists from various countries visited our Institute to perform experiments, discuss scientific results obtained within joint projects and to give talks in the colloquium of the Institute of Solid State Physics.

6.1 Visiting Scientists

Prof. Dr. T. Munakata	Osaka University
Prof. Dr. T. Yamada	Osaka University
MSc T. Ueba	Osaka University
Prof. F. Capasso	Harvard U, USA – **Carl-Zeiss Professur**
Prof. K. Baruth-Ram	iThemba Labs, Cape Town, Südafrika
Prof. J. G. Lu	University of Southern California, USA
Markus Glaser	TU Wien, Österreich
Prof. A. Lugstein	TU Wien, Österreich
Themis Sidiropoulos	Imperial College London, UK
Prof. Anna Foncuberta	EPF Lausanne, Schweiz
Dr. Stefan Janz	ISE Freiburg
Dr. Barbara Abendroth	TU Freiberg
Solveig Rentrop	TU Freiberg
Prof. Jan Meijer	U Leipzig
Prof. Maria Katsikini	U Thessaloniki
Prof. Sotirios Ves	U Thessaloniki
Kyriokos Filintoglou	U Thessaloniki
Dr. Liudmilla Vlasukova	BGU Minsk
Prof. Dr. K. Somiya	Tokyo Institute of Technology
Prof. Dr. Y. Shikano	National Institute of Natural Sciences, Institute for Molecular Science, Okazaki
Prof. Dr. K. Kuroda	The University of Tokyo
Prof. Dr. N. Kimura	KEK, High Energy Accelerator Research Organization, Tsukuba
Dr. A.Grib	Kharkov National University
Dr. M. van Veggel	University of Glasgow
Dr. K. Haughian	University of Glasgow
Dr. G. Hammond	University of Glasgow
Dr. S. Reid	University of the West of Scotland
Dr. J. Degallaix	Laboratoire des Matériaux Avancés - CNRS
Dr. M. Belogolovskii	University Rostov
Dr. V. Shaternik	Inst. Metal Phys. Kiev
Dr. A. Shapovalov	Inst. Metal Phys. Kiev
Dr. Y. Shukrinov	Joint Institute for Nuclear Research, Dubna, Russia
R. Douglas	University of Glasgow
S. Caffrey	University of the West of Scotland
A. Kumeta	Tokyo Institute of Technology
K. Ono	The University of Tokyo
S. Konisho	The University of Tokyo
A. Watanabe	Tokyo Institute of Technology
J. Kato	Tokyo Institute of Technology
M. Nakano	The University of Tokyo
I. Rahmonov	Joint Institute for Nuclear Research, Dubna, Russia

Dr. A. Gucsik	Tohoku University, Sendai Japan
Prof. Dr. A. Andersen	Dark Cosmology Center, Copenhagen, Denmark
Melinda Krebsz	Konkoly Thege Miklos Astronomical Institute, Astrophysical and Geochemical Laboratory, Budapest, Hungary
Steven Cuylle	Raymond and Beverly Sackler Laboratory for Astrophysics, Leiden

6.2 Colloquia at the Institute of Solid State Physics

PD Dr. C. Kumpf (FZ Jülich), Jan. 11, 2013
Interaction at metal - organic and heterorganic contacts: Adsorption of organic molecules on noble metal surfaces

Prof. Dr. Gianaurelio Cuniberti (TU Dresden), Jan. 25, 2013
Charge migration and heat phenomena in biomolecular systems: two sides of the same medal?

Dr. Regina Dittmann (FZ Jülich), Febr. 1, 2013
Oxide based RRAM: How defects can be useful for memory applications

Dr. Barbara Abendroth (TU Freiberg), Apr. 19, 2013
Structurual response of SrTiO3 on electroforming: the interplay of point defects and electric fields

Prof. Dieter Kölle (Uni Tübingen), May 3, 2013
Kolloquium zur Ernennung von Dr. F. Schmidl zum apl.-Prof."Empfindliche nanoSQUIDs für die Untersuchungen an kleinen Spinsystemen"

Prof. Dr. Jan Meijer (U Leipzig), May 17, 2013
Einzelionenimplantation als Schlüsselexperiment für Quantencomputer

Ao.Univ.-Prof. Dr. Egbert Zojer (TU Graz), May 31, 2013
Understanding the Peculiarities of the Electronic Structure of Metal - Organic Interfaces through Quantum - Mechanical Modeling

Dr. Thorsten Wagner (Johannes Kepler Universität Linz), June 28, 2013
Untersuchung des Wachstums von 6T auf Silberoberflächen mit PEEM, STM und LEED: Einfluss von Stufen auf die Epitaxie

Evelyn Stilp (Paul Scherrer Institut, Schweiz), July 5, 2013
Direct investigation of the Meissner screening profile in high Tc's by low - energy muon - spin rotation

Prof. Dr. Anna Fontcuberta i Morral (EPF Lausanne, Schwei), Oct. 18, 2013
Semiconductor nanowires: single photon emission and next generation photovoltaics

Justin Schneiderman (Chalmers University Göteborg, Schweden), Oct. 25, 2013
High-Tc SQUID-based MEGMRI: Combining next-generation structural and functional brain imaging techniques

Dr. Stefan Janz (ISE Freiburg), Nov. 8, 2013
Silicon Nanocrystals produced by Solid Phase Crystallisation for Photovoltaic Applications

Dr. Takashi Yamada (Osaka University, Japan), Nov. 22, 2013
Spectroscopic Investigation of Unoccupied Molecular States at the Nano- and Macroscopic Scale

Prof. Dr. Stefan Lochbrunner (Universität Rostock), Dec. 6, 2013
Mobile Electronic Excitations in Organic Materials and Supramolecular Structures

7. Teaching Activities

7.1 Lectures

Struktur der Materie II	Prof. Dr. T. Fritz Prof. Dr. C. Ronning
Festkörperphysik (Physik-Master)	Prof. Dr. T. Fritz
Nukleare Festkörperphysik	Prof. Dr. C. Ronning
Nanomaterials and Nanotechnology	Prof. Dr. C. Ronning
Physik für Nebenfach-Studenten (Biologie, Ernährungswissenschaften, Pharmazie, Biogeowissenschaften, Chemie, Biochemie)	Prof. Dr. E. Wendler
Kerne und Teilchen	Dr. C.S. Schnohr Prof. Dr. E. Wendler
Physik der Materie I	Prof. Dr. C. Ronning
Festkörpermodifikationen mit Ionenstrahlen	Prof. Dr. E. Wendler
Nukleare Festkörperphysik	Prof. Dr. C. Ronning
Vakuum-und Dünnschichtphysik	Prof. Dr. P. Seidel
Supraleitende Materialien	Prof. Dr. P. Seidel
Physik für Human- und Zahnmedizinstudenten	Prof. Dr. F. Schmidl
Festkörperphysik (Materialwiss. Master)	Prof. Dr. P. Seidel
Elektronik	Dr. R. Nawrodt Prof. Dr. F. Schmidl (verantwortl.)
Optoelectronics (Master of Photonics 3. Semester)	PD Dr. F. Schmidl
Laborastrophysik	Dr. C. Jäger Dr. H. Mutschke

7.2 Seminars

Proseminar zum Fortgeschrittenenpraktikum	Dr. B. Schröter
Physik der Materie II	Dr. R. Forker
Festkörperphysik (Physik-Master)	Dr. R. Forker
Nukleare Festkörperphysik	Dipl.-Phys. J. Rensberg
Physik der Materie I	Dr. M. Oertel Dipl.-Phys. A. Johannes, St.-Ex. H. Holland-Moritz

Physik für Biogeowissenschaftler	MSc. P. Schöppe
Kerne und Elementarteilchen	Dr. C.S. Schnohr
Physik für Chemiker	Dr. C.S. Schnohr Dipl.-Phys. M. Schmidt
Nanomaterialien und Nanotechnologie	Dipl.-Phys. J. Rensberg
Festkörperphysik (Materialwiss. Master)	Dr. V. Tympel
Optoelectronics (Master of Photonics 3. Semester)	Prof. Dr. F. Schmidl
Elektronik	Dipl.-Phys. J. Komma Dr. R. Nawrodt
Tieftemperaturphysik und Supraleitung	Prof. Dr. P. Seidel
Supraleitende Materialien	Prof. Dr. P. Seidel
Vorbereitungsmodul Staatsexamensprüfung Exphysik	Prof. Dr. P. Seidel, Prof. Dr. Spielmann
Tutorial Messtechnik	Dr. R. Nawrodt
Oberseminar (Festkörperphysik/Materialwissenschaften)	Prof. Dr. T. Fritz Prof. Dr. P. Seidel
Tutorial für Mediziner	Prof. Dr. F. Schmidl Dipl.-Phys. C. Katzer Dipl.-Phys. P. Michalowski
Laborastrophysik	Dr. H. Mutschke Dr. C. Jäger

7.3 Practica

Fortgeschrittenen-Praktikum	Prof. Dr. T. Fritz (verantwortl. HSL) Dr. B. Schröter (Leitung) Dipl-Ing. M. Thürk Dipl.-Phys. M. Kozlik Dipl.-Phys. F. Sojka Dipl.-Phys. M. Grünewald Dipl.-Phys. Jana Sommerfeld Dipl.-Phys. Martin Gnauck
Praktikum für Biochemiker	Prof. Dr. E. Wendler (Leitung)
Praktikum für Biologen	Prof. Dr. E. Wendler (Leitung)
Praktikum für Nebenfächler	Prof. Dr. E. Wendler (Leitung) Dr. C.S. Schnohr
Kernphysikalisches Praktikum	Dr. U. Reislöhner (Leitung) Dipl.-Phys. Sebastian Geburt Dipl.-Phys. Steffen Wolf MSc. Emanuel Schmidt

Physikalisches Grundpraktikum für Mediziner	Prof. Dr. F. Schmidl (Leitung)
	Dipl.-Phys. C. Katzer
	Dipl.-Phys. S. Schmidt
	MSc. Robert Röder
Physikalisches Praktikum für Zahnmediziner	Prof. Dr. F. Schmidl (Leitung)
Messtechnik	Dr. R. Nawrodt (Leitung)
	Dr. C. Schwarz
	Dipl.-Phys. J. Komma
	Dipl.-Phys. C. Heisler
	Dipl.-Ing. H. Mühlig
	Dipl.-Phys. Sven Schönherr
	Dipl.-Phys. Christoph Heisler
Elektronikpraktikum	Dr. R. Nawrodt (Leitung)
Lehramtskandidaten 5. Sem. Physik-Bachelor, Nebenfächler	Prof. Dr. F. Schmidl
	Dipl.-Ing. H. Mühlig
	Dipl.-Ing. R. Neubert
	Dipl.-Phys. S. Schönherr
Grundpraktikum	Dr. R. Nawrodt
3.Semester Bachelor Physik	Dr. C. Schwarz
	Dr. D. Heinert
	Dipl.-Phys. S. Schönherr
	Dipl.-Phys. C. Heisler
	Dipl.-Phys. G. Hofmann
	Dipl.-Ing. H. Mühlig
	Dipl.-Ing. R. Neubert
Lab course Master of Photonics	MSc. Davide Cammi
	MSc. Yaser Haj-Hmeidi

8. Personnel

Professors

Prof. Dr. habil. Torsten Fritz (director)
Prof. Dr. habil. Carsten Ronning
Prof. Dr. habil. Paul Seidel
apl. Prof. Dr. habil. Elke Wendler
apl. Prof. Dr. habil. Frank Schmidl
Prof. Dr. Puxian Gao (Humboldt-Fellow, since 09/2013)

Scientific Staff

Dr. R. Forker
Dr. Bernd Schröter
Dr. Claudia Schnohr
Dr. Udo Reislöhner
Dr. Ernst Glaser
Dr. Tobias Steinbach (till 08/2013)
Dr. Cornelia Jäger
Dr. Gael Rouillé
Dr.-Ing. V. Tympel
Dr. R. Nawrodt
Dr. D. Heinert
Dr.-Ing. C. Schwarz
Dr. Michael Oertel
Dr. Christian Kraft (till 05/2013)
Dr. Sergiy Krasnokutski
Dr. Abel Brieva
Dr. Sebastian Geburt (till 04/2013)

PhD Students

Michael Kozlik
Marco Grünewald
Christian Udhardt (since 10/2013)
Steffen Wolf
Andreas Johannes
Philipp Schöppe
Martin Gnauck
Henry Holland-Moritz
Sven Schönherr
Jura Rensberg
Gerd Hofmann
Julius Komma
Sebastian Döring
Tolou Sabri
Karsten Potrick
Matthias Meissner
Falko Sojka
Christoph Heisler
Jana Sommerfeld
Yaser Haj-Hmeidi
Davide Cammi
Robert Röder
Matthias Schmidt
Stefanie Eckner
Stefan Schmidt
Christian Katzer
Peter Michalowski
Ali Hasan Noor
Rene Geithner
Hagen Walter

Extern PhD Students

Michael Blech	CiS Erfurt
Matthias Rost	Bosch Solar Energy, Arnstadt
Charlotte Weiss	Frauenhofer ISE, Freiberg
Stephan Pohlner	AVANCIS GmbH (till 11/2013)
Florian Krippendorf	FH Jena
Constantin Csato	FH Jena
Gregor Oelsner	IPHT Jena

Thomas Schönau	IPHT Jena
Uwe Schinkel	IPHT Jena
Ivo Zunke	Innovent

Diploma and Master Students

Christian Udhardt
Marcel Grosch
Tino Kästner
Benjamin Rößler
Martin Krause
Felix Felgenträger
Marcel Wille
Tim Barth
Stefan Noack
Max Riediger
Bastian Walter
Stefanie Koch
Sandra Gottwals
Markus Westerhausen
Markus Weidner
Romina Diener
Felix Lind
Martin Salge
Sebastian Vatterodt
Matthias Ogrisek
Hannes Hempel
Marcel Hopfe
Alexander Kusch
Markus Schwiderke
Alexander von Müller
Matthias Ring
Martin Feltz
David Reifert
Manuel Monecke
Hendrik Bernhardt
Philipp Naujok

Extern Diploma and Master Students

-/-

Technical Staff

Ulrich Barth
Marie Boxhammer
Uwe Eberhardt
Tobias Eißmann
Lutz Föllmer
Silke Frunzke
Kristina Garlipp
Frank Jehn
Patrick Hoffmann
Holger Mühlig
Anja Mittelstädt
Ralf Neubert
Stefan Prass
Helga Rudolph
Sylvia Stender
Matthias Thürk
Carmen Voigt